REPORT DOCUMENTATION PAGE

Form Approved OMB NO. 0704-0188

1. REPORT DATE (DD-MM-YYYY)	2. REPORT TYPE	3. DATES COVERED (From - To)
25-10-2018	Final Report	26-Sep-2016 - 29-Sep-2018

4. TITLE AND SUBTITLE

Final Report: Parallel Two-Electron Reduced Density Matrix Based Electronic Structure Software for Highly Correlated Molecules and Materials

5a. CONTRACT NUMBER

5b. GRANT NUMBER
W911NF-16-C-0124

5c. PROGRAM ELEMENT NUMBER
665502

6. AUTHORS

5d. PROJECT NUMBER

5e. TASK NUMBER

5f. WORK UNIT NUMBER

7. PERFORMING ORGANIZATION NAMES AND ADDRESSES

Q-Chem, Inc.
6601 Owens Drive
Suite 105
Pleasanton, CA 94588 -0000

8. PERFORMING ORGANIZATION REPORT NUMBER

9. SPONSORING/MONITORING AGENCY NAME(S) AND ADDRESS (ES)

U.S. Army Research Office
P.O. Box 12211
Research Triangle Park, NC 27709-2211

10. SPONSOR/MONITOR'S ACRONYM(S)
ARO

11. SPONSOR/MONITOR'S REPORT NUMBER(S)
69478-CH-ST2.3

12. DISTRIBUTION AVAILIBILITY STATEMENT

Approved for public release; distribution is unlimited.

13. SUPPLEMENTARY NOTES

The views, opinions and/or findings contained in this report are those of the author(s) and should not contrued as an official Department of the Army position, policy or decision, unless so designated by other documentation.

14. ABSTRACT

15. SUBJECT TERMS

16. SECURITY CLASSIFICATION OF:			17. LIMITATION OF ABSTRACT	15. NUMBER OF PAGES	19a. NAME OF RESPONSIBLE PERSON
a. REPORT	b. ABSTRACT	c. THIS PAGE			Albert DePrince
UU	UU	UU	UU		19b. TELEPHONE NUMBER: 850-645-1291

RPPR Final Report
as of 26-Oct-2018

Agency Code:

Proposal Number: 69478CHST2 **Agreement Number: W911NF-16-C-0124**
INVESTIGATOR(S):

Name: Albert Eugene DePrince
Email: deprince@chem.fsu.edu
Phone Number: 8506451291
Principal: Y

Organization: **Q-Chem, Inc.**
Address: 6601 Owens Drive, Pleasanton, CA 945880000
Country: USA

DUNS Number: 837635556 EIN:
Report Date: 25-Oct-2018 Date Received: 25-Oct-2018
Final Report for Period Beginning 26-Sep-2016 and Ending 29-Sep-2018
Title: Parallel Two-Electron Reduced Density Matrix Based Electronic Structure Software for Highly Correlated Molecules and Materials
Begin Performance Period: 26-Sep-2016 **End Performance Period:** 29-Sep-2018
Report Term: 0-Other

Submitted By: Albert DePrince Email: deprince@chem.fsu.edu
Phone: (850) 645-1291

Distribution Statement: 1-Approved for public release; distribution is unlimited.

STEM Degrees: 2 **STEM Participants:** 3

Major Goals: The accurate and balanced description of ground and electronically excited states is of central importance in elucidating the optical, catalytic, and energetic properties of molecules and materials. For small molecules whose electronic wave functions can be qualitatively described by a single-reference configuration, this problem is largely solved; the coupled-cluster (CC) and equation-of-motion CC hierarchies are powerful methods for obtaining ground- and excited-state wave functions, energies, and properties. However, when considering more complex molecules, transition states, or molecular configurations far from equilibrium, static or nondynamical correlation effects may become important, and standard single-reference approaches can no longer guarantee a reliable description of the electronic structure.

The standard approach for capturing nondynamical correlation effects is the complete active space self-consistent field (CASSCF) method. However, because the size of the underlying configuration interaction (CI) expansion of the wave function grows exponentially with the size of the active space, the application of CI-based CASSCF to large actives spaces is nontrivial. The treatment of large active spaces requires one to either (i) abandon CI in favor of some other wave function expansion that scales polynomially with system size or (ii) abandon the wave function altogether. We adopt the latter strategy, as methods that employ the two-electron reduced-density matrix (2-RDM) as the central variable (instead of the wave function) have the potential to overcome the scaling problems that plague CI.

The primary goal of the STTR was to develop an efficient 2-RDM-based library for large-scale CASSCF computations within the Q-Chem electronic structure package. The library would have access to all of the useful features developed within Q-Chem prior to this STTR, including effective core potentials and methods for incorporating solvent effects. Specific efforts toward this goal included:

1. Enhancing computational efficiency of v2RDM-CASSCF through new algorithms that exploit either (i) the advanced tensor library, libtensor,3 (ii) parallel eigensolvers such as ScaLAPACK or Elemental, or (iii) graphical processing units (GPUs).

2. Improving convergence in the boundary-point semidefinite solver for the v2RDM problem.

3. Fully integrating the library with Q-Chem so as to have access to its rich set of existing features. The library should also be compatible with the IQmol molecular visualizer.

4. Enhancing the capabilities of the software, including analytic energy gradient evaluation for v2RDM-CASSCF, methods to model excited states, and models for dynamical correlation effects not captured by v2RDM-CASSCF.

Accomplishments: See document uploaded at the end of this report.

Training Opportunities: Undergraduate Student Training:

This STTR supported summer research opportunities for undergraduate student Lauren Koulias. Lauren worked closely with PI Eugene DePrince and postdoctoral researcher Wayne Mullinax to develop an implementation of the v2RDM method that exploited graphical processing units (GPUs). This research opportunity exposed Lauren to important concepts relevant to large-scale collaborative software development and GPU-based programming, improving her proficiency as a developer. Lauren defended an Honors Thesis related to this STTR and is currently a graduate student in Chemistry at the University of Washington

Graduate Student Training:

This STTR has supported Mohammad (Sina) Mostafanejad as a graduate research assistant. Sina worked closely with PI Eugene DePrince and postdoctoral researcher Wayne Mullinax to develop an implementation of the multiconfigurational pair density functional theory (MCPDFT) to model dynamical correlation not captured by v2RDM-CASSCF. Sina has had the opportunity to present his research in a talk at the National ACS Meeting in Boston in August 2018, and he will present a poster at the National ACS Meeting in Orlando in the spring. Sina has also used his experience to develop a proposal for a graduate research fellowship through the Molecular Sciences Software Institute.

Postdoctoral Training:

The STTR has supported Wayne Mullinax as a postdoctoral researcher. Wayne has gained valuable software development experience as the primary developer of the v2RDM-CASSCF library within Q-Chem. He has also gained valuable mentorship experience while working with undergraduate student Lauren Koulias and graduate student Sina Mostafanejad. The STTR has also given him the opportunity to travel to collaborate in person with co-PI Evgeny Epifanovsky at Q-Chem and to attend an NVIDIA Technical Summit in spring 2018.

Results Dissemination: We have submitted two manuscripts to the Journal of Chemical Theory and Computation. The first manuscript details our implementation of analytic energy gradients for the v2RDM-CASSCF method in Q-Chem. This implementation improves makes use of the density fitting approximation to the two-electron repulsion integrals, which facilitates geometry optimizations and harmonic frequency analysis (using finite differences of analytic energy gradients) on large molecules. A preprint of this manuscript can be found on the arXiv (https://arxiv.org/abs/1809.09058); this preprint is also included in the supplementary document uploaded with this report. The second manuscript describes our pilot implementation of the multi configurational pair density functional theory (MCPDFT) approach, which serves as a computationally efficient way of incorporating dynamical correlation effects on top of v2RDM-CASSCF computations. A preprint of this manuscript can be found on the arXiv (https://arxiv.org/abs/1810.00753); this preprint is also included in the supplementary document uploaded with this report. We are preparing a third manuscript detailing our implementation of the v2RDM-CASSCF method that makes use of graphical processing units (GPUs). The GPU-driven implementation (using an NVIDIA Quadro GP100 GPU) is as much as 3.8 times more efficient than the CPU-driven implementation (using 6 cores of an Intel core i7-6830k processor). We have also presented our work at national chemistry conferences; for example, PI Eugene DePrince and graduate student Mohammad Mostafanejad each gave talks on research supported by this STTR at the 256th national ACS meeting in Boston in August 2018.

Honors and Awards: DePrince: Openeye Outstanding Junior Faculty Award, COMP Division of the American Chemical Society, 2017

DePrince: Emerging Young Investigator, Florida Local Section of the ACS, 2017

Protocol Activity Status:

Technology Transfer: Nothing to Report

RPPR Final Report
as of 26-Oct-2018

PARTICIPANTS:

Participant Type: Postdoctoral (scholar, fellow or other postdoctoral position)
Participant: Jimmy Wayne Mullinax
Person Months Worked: 15.00 **Funding Support:**
Project Contribution:
International Collaboration:
International Travel:
National Academy Member: N
Other Collaborators:

Participant Type: PD/PI
Participant: Albert Eugene DePrince III
Person Months Worked: 2.00 **Funding Support:**
Project Contribution:
International Collaboration:
International Travel:
National Academy Member: N
Other Collaborators:

Participant Type: Graduate Student (research assistant)
Participant: Mohammad Mostafanejad
Person Months Worked: 15.00 **Funding Support:**
Project Contribution:
International Collaboration:
International Travel:
National Academy Member: N
Other Collaborators:

Participant Type: Co PD/PI
Participant: Evgeny Epifanovsky
Person Months Worked: 15.00 **Funding Support:**
Project Contribution:
International Collaboration:
International Travel:
National Academy Member: N
Other Collaborators:

Participant Type: Undergraduate Student
Participant: Lauren Koulias
Person Months Worked: 3.00 **Funding Support:**
Project Contribution:
International Collaboration:
International Travel:
National Academy Member: N
Other Collaborators:

Participant Type: Staff Scientist (doctoral level)
Participant: Zhengting Gan
Person Months Worked: 2.00 **Funding Support:**
Project Contribution:
International Collaboration:
International Travel:
National Academy Member: N

Other Collaborators:

Participant Type: Staff Scientist (doctoral level)
Participant: Fazle Rob
Person Months Worked: 4.00 **Funding Support:**
Project Contribution:
International Collaboration:
International Travel:
National Academy Member: N
Other Collaborators:

Participant Type: Staff Scientist (doctoral level)
Participant: Xintian Feng
Person Months Worked: 2.00 **Funding Support:**
Project Contribution:
International Collaboration:
International Travel:
National Academy Member: N
Other Collaborators:

Participant Type: Staff Scientist (doctoral level)
Participant: Adrian Morrison
Person Months Worked: 1.00 **Funding Support:**
Project Contribution:
International Collaboration:
International Travel:
National Academy Member: N
Other Collaborators:

Participant Type: Staff Scientist (doctoral level)
Participant: Ilya Kaliman
Person Months Worked: 1.00 **Funding Support:**
Project Contribution:
International Collaboration:
International Travel:
National Academy Member: N
Other Collaborators:

ARTICLES:

RPPR Final Report
as of 26-Oct-2018

Publication Type: Journal Article Peer Reviewed: Y **Publication Status:** 4-Under Review
Journal: Journal of Chemical Theory and Computation
Publication Identifier Type: Other Publication Identifier:
Volume: Issue: First Page #:
Date Submitted: 10/24/18 12:00AM Date Published:
Publication Location:
Article Title: Combining pair-density functional theory and variational two-electron reduced-density matrix methods
Authors: Mohammad Mostafanejad
Keywords: v2RDM, CASSCF, MCPDFT
Abstract: CASSCF computations can be realized at polynomial cost via the variational optimization of the active-space two-electron reduced-density matrix (2-RDM). Like conventional approaches to CASSCF, variational 2-RDM (v2RDM)-driven CASSCF captures nondynamical electron correlation in the active space, but it lacks a description of the remaining dynamical correlation effects. Such effects can be modeled through a combination of v2RDM-CASSCF and on-top pair-density functional theory (PDFT). The resulting approach provides an inexpensive framework for describing both static and dynamical correlation effects in strongly correlated systems. On-top pair-density functionals can be derived from familiar exchange-correlation (XC) functionals through the translation of the v2RDM-CASSCF densities. On-top PDFT versions of several common XC functionals are applied to the potential energy curves of N2, H2O, and CN-, as well as to the singlet/triplet energy splittings in the linear polyacene series.
Distribution Statement: 1-Approved for public release; distribution is unlimited.
Acknowledged Federal Support: **Y**

Publication Type: Journal Article Peer Reviewed: Y **Publication Status:** 4-Under Review
Journal: Journal of Chemical Theory and Computation
Publication Identifier Type: Publication Identifier:
Volume: Issue: First Page #:
Date Submitted: 10/24/18 12:00AM Date Published:
Publication Location:
Article Title: Analytic energy gradients for variational two-electron reduced-density matrix methods within the density-fitting approximation
Authors: Wayne Mullinax, Evgeny Epifanovsky, Gergely Gidofalvi, Eugene DePrince
Keywords: v2RDM, CASSCF, analytic energy gradient
Abstract: Analytic energy gradients are presented for a variational two-electron reduced-density-matrix (v2RDM) driven CASSCF procedure that employs the density-fitting (DF) approximation to the two-electron repulsion integrals. The DF approximation significantly reduces the computational cost of v2RDM-CASSCF gradient evaluation, enabling geometry optimizations on much larger chemical systems than could previously be considered at the this level of theory. The efficacy of v2RDM-CASSCF for computing equilibrium geometries and harmonic vibrational frequencies is assessed using a set of 25 small molecules. Optimized geometries are obtained for the lowest-energy singlet and triplet states of the linear polyacene series up to dodecacene (C50H28), in which case the active space is comprised of 50 electrons in 50 orbitals. The v2RDM-CASSCF singlet-triplet energy gap extrapolated to an infinitely-longlinear acene molecule is found to be 7.8 kcal/mol.
Distribution Statement: 1-Approved for public release; distribution is unlimited.
Acknowledged Federal Support: **Y**

RPPR Final Report
as of 26-Oct-2018

Accomplishments:

The primary goal of the STTR was to develop an efficient two-electron reduced-density matrix (2-RDM) based library for large-scale complete active space self-consistent field (CASSCF) computations within the Q-Chem electronic structure package. We have succeeded in this goal. As noted in the release log for Q-Chem 5.1 (http://www.q-chem.com/qchem-website/releaselog_51.html), our variational 2-RDM (v2RDM) library is fully incorporated into Q-Chem. The features of the publicly available version include:

- v2RDM and v2RDM-CASSCF energy computations on closed- or open-shell systems,
- full use of abelian point group symmetry
- analytic energy gradients for geometry optimizations and, in principle, *ab initio* molecular dynamics simulations
- use of the density fitting (DF) approximation for the two-electron repulsion integrals (ERIs), which greatly enhances the efficiency of the orbital optimization procedure and analytic energy gradient evaluation
- enforcement two-particle (PQG)[1] and partial three-particle (T1/T2)[2] *N*-representability conditions
- compatibility with effective core potentials (ECPs) and implicit solvent models (i.e. the polarizable continuum model, PCM)
- one-electron properties, including multipole moments (up to molecular hexadecapoles), atomic charge decomposision (Mulliken and Lowdin charges), natural bond orbital analysis, natural orbitals and their occupation numbers
- natural orbital visualization through the IQMol molecular viewer

The section of the Q-Chem user manual relevant to the v2RDM library can be found at the end of this report. Additional features that are nearly complete and will be advertised in future releases include

- a graphical processing unit (GPU) accelerated algorithm for v2RDM-CASSCF
- a dynamical correlation model for v2RDM-CASSCF based on the multiconfigurational pair-density functional theory (MCPDFT)

The STTR has also produced two manuscripts detailing our implementation of (i) analytic energy gradients within the DF approximation and (ii) v2RDM-CASSCF coupled to the MCPDFT approach. These manuscripts were submitted in October 2018 and, as of the writing of this report, are still under review. A third manuscript detailing our GPU-accelerated v2RDM algorithm is in preparation.

The remainder of this section addresses the sub-aims of this STTR under the overarching software development effort.

1. Enhancing computational efficiency of v2RDM-CASSCF through new algorithms that exploit either (i) the advanced tensor library, libtensor,[3] (ii) parallel eigensolvers such as ScaLAPACK or Elemental, or (iii) graphical processing units (GPUs).

A significant amount of effort was dedicated to improving the computational efficiency of each component of the v2RDM-CASSCF procedure. In order to understand the relative performance of various implementations, we must first review the structure of the boundary-point semidefinite programming (SDP) algorithm for the v2RDM problem, which is a two-step procedure. In step 1, we update the dual solution to the SDP (**y**) by solving

$$\mathbf{A}\mathbf{A}^{\mathrm{T}}\mathbf{y} = \mathbf{A}(\mathbf{c}\text{-}\mathbf{z}) + \mu(\mathbf{b}\text{-}\mathbf{A}), \tag{1}$$

using the conjugate gradient (CG) method. Here, **x** represents the primal solution vector, **y** and **z** represent dual solution vectors, **c** represents a vector containing the one- and two-electron integrals that define the quantum system, and **A** and **b** represent the constraint matrix and vector, respectively. The symbol μ represents a penalty parameter. The solution of Eq. 1 requires the repeated evaluation of matrix-vector products of the form **Au** and $\mathbf{A}^{\mathrm{T}}\mathbf{u}$. The second step in the optimization is a diagonalization/transformation step whereby the matrix

$$\mathbf{U}(\mathbf{x}) = \mu\mathbf{x} + \mathbf{A}^{\mathrm{T}}\mathbf{y} - \mathbf{c} \tag{2}$$

is separated into positive and negative components via diagonalization to update the primal solution (**x**), as well as a secondary dual vector (**z**). For v2RDM-driven CASSCF, we must also consider an orbital optimization step, the cost of which is dominated by the transformation of the two-electron repulsion integrals.

As part of Phase I, we developed a closed-shell boundary-point solver for the v2RDM approach with two-particle (PQG) *N*-representability conditions using Q-Chem's libtensor library, and we demonstrated that the libtensor implementation was roughly three times more efficient than our original hand-tuned ("loops") code for solving Eq. 1 for large systems (with no point group symmetry). One of our first goals in Phase II was to extend the applicability of the libtensor implementation to open-shell systems and active-space computations required for v2RDM-CASSCF. By the conclusion of month three, we had developed a libtensor implementation of the v2RDM solver for both closed- and open-shell systems that enforced the PQG conditions. For closed shells, the solver can enforce the PQG constraints for either spin-adapted and non-spin-adapted reduced-density matrices. Unfortunately, once we had further optimized the "loops" code and we considered the total time to solution for the algorithm as a whole, it became clear that the hand-tuned code is superior in general. Nonetheless, we completed implementations of the T1 and T2 partial three-particle *N*-representability conditions within libtensor as well.

We next began developing an implementation of v2RDM-CASSCF that utilized graphical processing units (GPUs) in each of steps described above. The majority of the work in solving Eq. 1 reduces to level-1 BLAS functions (e.g. DCOPY, DAXPY, etc.) or other memory-bound operations such as tensor transposes. GPUs can be used to accelerate such operations because the memory bandwidth on a GPU is several times higher than on a modern CPU. For example, the memory bandwidth on a NVIDIA Kepler K40c GPU is roughly 4.2 times higher than that of an Intel Core i7-5930K CPU. On the other hand, the solution to the eigenvalue problem, surprisingly, is more efficient when carried out on the CPU than on the GPU, provided that the diagonalization routines employed are parallelized to make use of several computer cores or several matrices are diagonalized in parallel.

We have developed a GPU-enabled v2RDM-CASSCF solver in a development version of Q-Chem (technically, the a prototype code is present in the 5.1 release, but it will not be advertised until a future release). If a user wishes to exploit GPU hardware, they simply need to (i) have access to a compute-oriented GPU (preferably at least as new as the Kepler generation of the NVIDIA Tesla GPU line), (ii) compile the Q-Chem source code with a simple configure flag ("CUDA"), and (iii) specify in the Q-Chem input file an option ("RDM_RUN_ON_GPU TRUE"). Figure 1 illustrates the relative times required to carry out each major step of the v2RDM-CASSCF procedure on a CPU (Intel core i7-6850k, six cores) and a GPU (NVIDIA GP100). The "dual update" refers to the solution of Eq. 1 by the CG method, and the "primal update" refers to the diagonalization/transformation step involving $\mathbf{U}(\mathbf{x})$ (Eq. 2). The systems on which we tested the code are the singlet states of the linear polyacene series (in the cc-pVDZ basis set) with one to 12 fused benzene rings (k). The active space in each computation was comprised of 4k+2 π and 4k+2 π^* orbitals. In the case of dodecacene (k=12), this corresponds to an active space of 50 electrons in 50 orbitals.

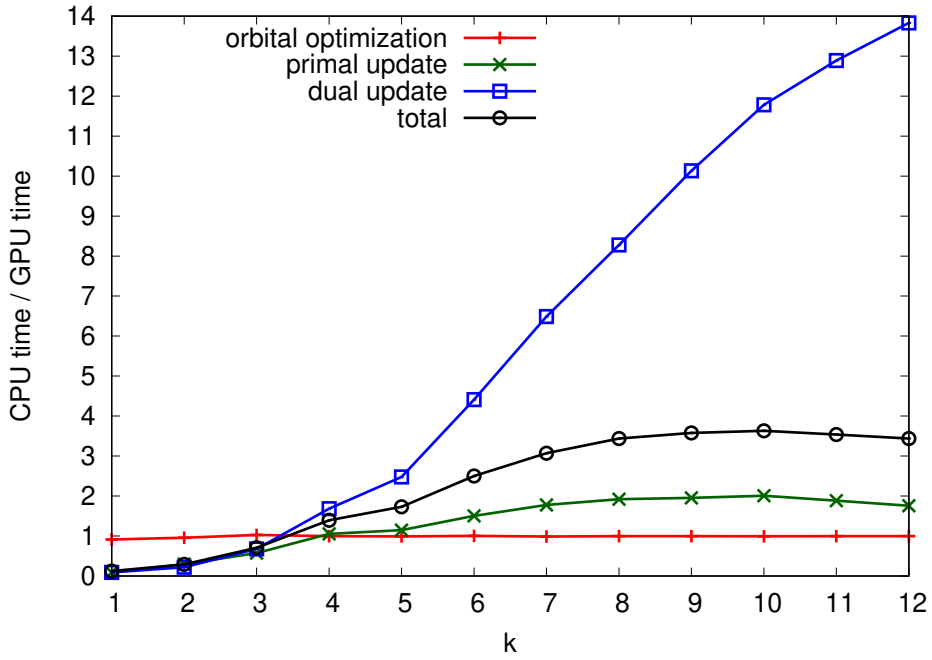

Figure 1. Relative times for various steps in the v2RDM-CASSCF algorithm when executed on six cores of a core i7-6850K CPU and an NVIDIA GP100 GPU.

First, it appears that the orbital optimization step requires essentially the same wall time with and without the use of the GPU. Second, the solution to Eq. 1 is far more efficient on the GPU than on the CPU; for large systems, we observe speedups approaching a factor of 14. Third, the diagonalization transformation step ("update primal") is only accelerated by, at most, a factor of two. As mentioned above, the diagonalization of $\mathbf{U}(\mathbf{x})$ is, surprisingly, more efficiently performed on the CPU than on the GPU. So, we transfer the data off of the GPU for this step and copy it back onto the GPU once $\mathbf{U}(\mathbf{x})$ has been diagonalized (this step involves the only data motion between CPU and GPU during the v2RDM-CASSCF iterations). Most of the speedup observed

for this step can be traced to the transformation of the reduced density matrices from the eigenbasis of $\mathbf{U}(\mathbf{x})$ back to the original basis, which is performed on the GPU. For the largest system considered (dodecacene, 50 electrons in 50 orbitals), the entire v2RDM-CASSCF energy optimization requires 3.17 hours, when the algorithm is executed on the CPU. When executed on the GPU, this computation can be performed in only 55 minutes! So, we have demonstrated that we can perform v2RDM-CASSCF computations on active spaces involving as many 50 electrons in 50 orbitals in **less than one hour**; this result is possibly the greatest accomplishment of this STTR.

We note that we had originally intended to explore the utility of parallel eigensolvers for the diagonalization step such as ScaLAPACK or Elemental. However, we have since concluded that, at least in the case that we are enforcing the PQG conditions, it is unlikely that we would observe significant increases in the efficiency of this step. We are still considering the use of these libraries for the case that we enforce the T1/T2 partial three-particle *N*-representability conditions.

2. Improving convergence in the boundary-point semidefinite solver for the v2RDM problem.

We explored strategies to improve the convergence of the inner iterations of the boundary-point SDP solver. In our present implementation, the inner iterations that update the dual solution involve the solution of a system of equations (Eq. 1) by CG techniques. Our attempt at improving the convergence involved the following changes to the algorithm:

(i) Solve the linear system of equations using Jacobi iterations, rather than CG.
(ii) Accelerate the solution of the Jacobi iterations using the direct inversion of the iterative subspace (DIIS), as is routinely done in self-consistent field and coupled-cluster computations.

We found that the Jacobi iterations are ill suited for this problem, as the matrix AA^T is not diagonally dominant. A modified Jacobi procedure in which one scales the diagonal elements of AA^T will converge in many cases, and the DIIS procedure does indeed significantly reduce the number of Jacobi iterations required for convergence. However, for most cases, the performance of the Jacobi+DIIS procedure is inferior to our existing CG machinery.

We also performed a series of benchmark tests to determine the optimal balance between v2RDM and orbital optimization steps in v2RDM-CASSCF. In standard CASSCF, a two-step optimization strategy first fully converges the CI wave function describing the active space. In the second step, a single orbital optimization step is performed with fixed CI coefficients. In two-step v2RDM-CASSCF, we showed previously[4] that the total run time for the algorithm can be significantly reduced by performing orbital optimization steps at regular intervals with *unconverged* reduced density matrices. During this STTR, we explored how the number of orbital optimization steps performed at a given time influences the total wall time for the optimization. Figure 2 illustrates the ratio of the total v2RDM-CASSCF optimization time relative to the case where the orbital optimization is performed every 500 v2RDM iterations, and the orbital optimization involves only one optimization step.

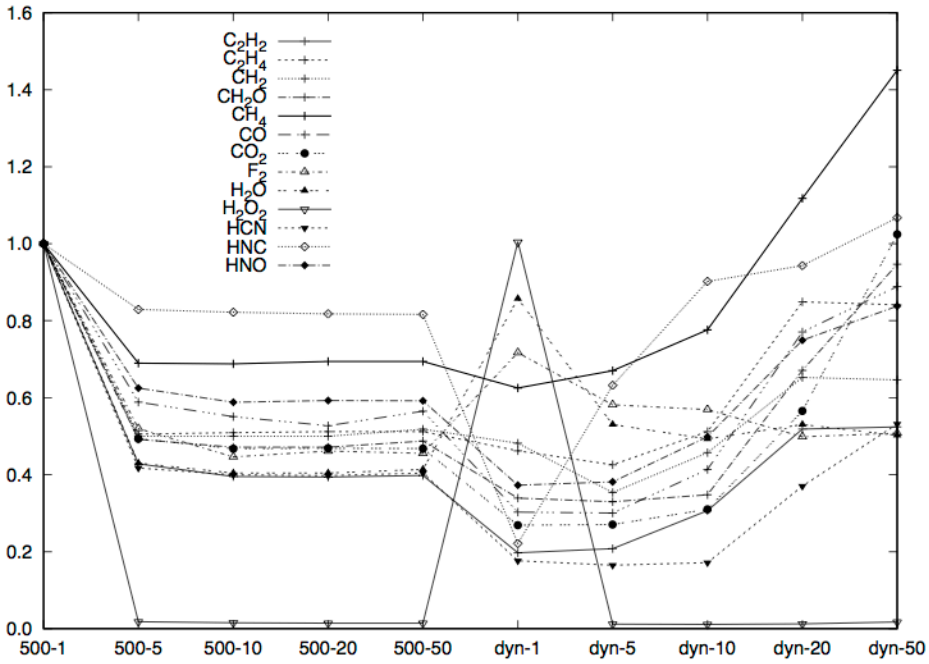

Figure 2. Relative total v2RDM-CASSCF times for static and dynamic orbital optimization schedules. See text for details.

The label "500-X" indicates that the orbital optimization is called every 500 v2RDM iterations, and the orbital optimization can take a maximum of X steps. The label "dyn-X" indicates that the v2RDM and orbital optimization criteria are updated dynamically throughout the computation, and that the orbital optimization is allowed to take a maximum of X steps. We can draw two conclusions from these data. First, for static the optimization schedule ("500-X"), the computations are universally more efficient if the orbital optimizer is allowed to take more than one step at a time. Second, the dynamic update scheme we have developed appears to be slightly more efficient overall than the static scheme for a maximum number of orbital optimization steps of five or 10. Upon reviewing these results, we have determined the algorithm should employ the dynamic scheme with a maximum of 10 orbital optimization steps at each time the orbital optimizer is called.

3. Fully integrating the library with Q-Chem so as to have access to its rich set of existing features. The library should also be compatible with the IQmol molecular visualizer.

As mentioned above, the v2RDM library is fully integrated into Q-Chem. Single-point energy computations and geometry optimizations can be set up using the standard text interface for Q-Chem. The user can choose to enforce a variety of N-representability conditions, including the two-particle (PQG) conditions of Garrod and Percus and the partial three-particle conditions known as the T1 and T2 conditions. The user can choose one of three algorithms for the v2RDM optimization based on (i) a hand-tuned "loop"-based code, (ii) the tensor library, libtensor, or (iii) a hand-tuned GPU-accelerated algorithm. Of the CPU-based codes, the hand-tuned algorithm is the more efficient and flexible and thus the default choice. Active space selection for v2RDM-CASSCF according is straightforward and can be done according to the symmetry of the orbitals. Effective core potentials can be easily incorporated into computations on heavy elements, as with any other method in Q-Chem, and the polarizable continuum model can be used within the "non-

equilibrium" mode. As shown in Figure 3, the natural orbitals from a v2RDM-CASSCF computation can be visualized using the IQMol molecular viewer.

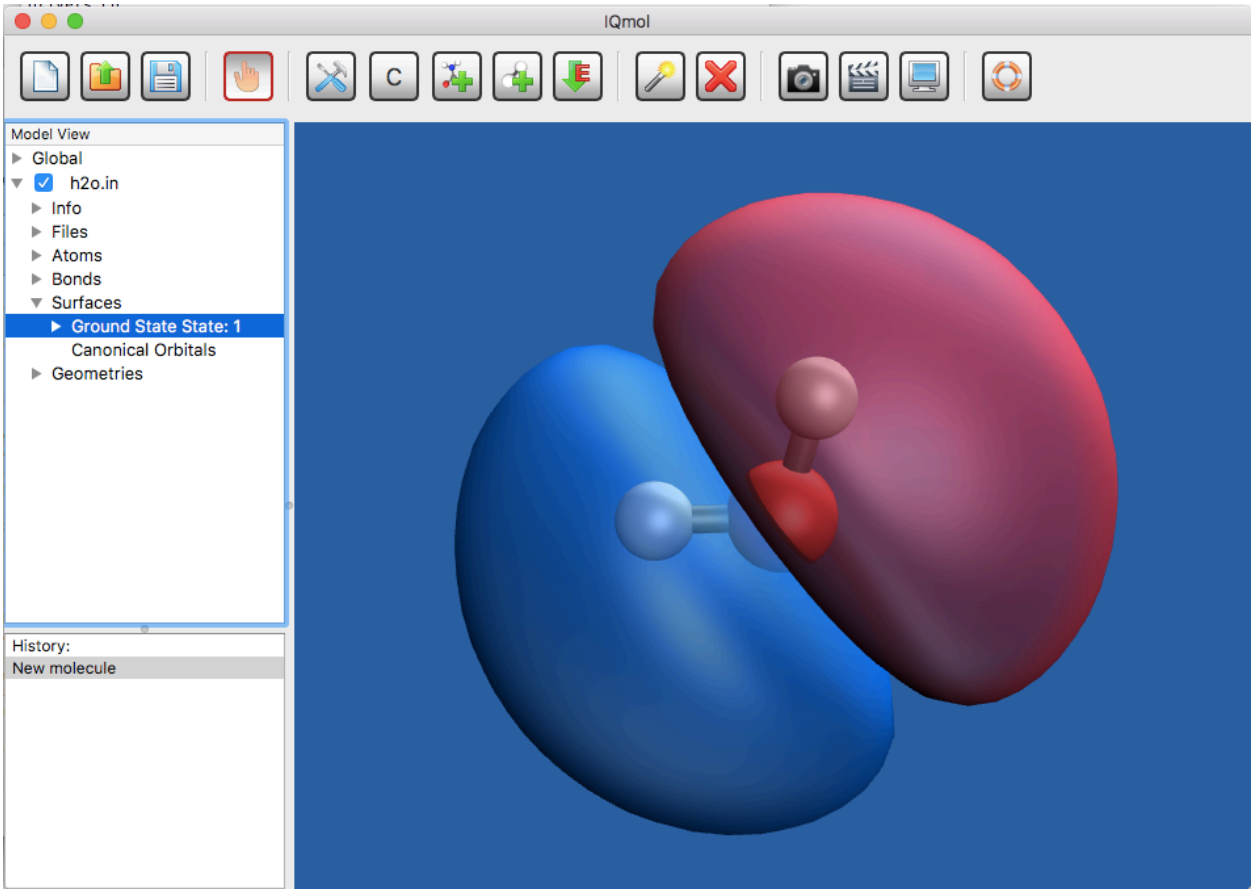

Figure 3. The highest occupied natural orbital for H_2O described at the full-valence v2RDM-CASSCF/6-31G level of theory, as visualized in IQMol.

4. Enhancing the capabilities of the software, including analytic energy gradient evaluation for v2RDM-CASSCF, methods to model excited states, and models for dynamical correlation effects on top of v2RDM-CASSCF.

With the core functionality for v2RDM-CASSCF in place, we were able to explore additional capabilities for the library. We have developed an analytic energy gradient implementation that makes use of the DF approximation to the ERIs. The DF approximation dramatically reduces the floating-point cost and storage requirements for analytic energy gradients from v2RDM-CASSCF. We have submitted a manuscript describing our implementation which is currently under review. In that work, we benchmarked the quality of v2RDM-CASSCF equilibrium geometries and harmonic vibrational frequencies for a set of 25 open- and closed-shell molecules. The second derivatives required for the frequency analysis were obtained from finite differences of analytic energy gradients. We also explored the applicability of the v2RDM-CASSCF analytic gradient implementation to large molecular systems by computing equilibrium geometries and singlet/triplet energy gaps for the linear polyacene series up to dodecacene, which consists of 12 fused benzene rings. Using an active space comprised of $4k+2$ π and $4k+2$ π^* orbitals, where k represents the number of fused benzene rings, the dodecacene computation

involves an active space of 50 electrons in 50 orbitals, which is far larger than that which could be treated using a conventional, full CI-based CASSCF algorithm.

We also developed a dynamical correlation correction to the v2RDM-CASSCF energy. CASSCF and related active-space-based methods are typically employed to describe strong or nondynamical correlation effects that are difficult to capture using standard single-reference approaches, such as coupled-cluster (CC) theory or density functional theory (DFT). However, active-space methods do not capture important dynamical correlation effects that are in general well-described by CC and DFT. A number of dynamical correlation corrections for CASSCF-type methods have been proposed in the literature to date, and many of these methods (e.g. those based on multireference perturbation theory [CASPT2]) require the storage and manipulation of high-order density matrices. The multiconfigurational pair-density functional theory (MCPDFT) approach, on the other hand, is substantially simpler in that it represents the dynamical correlation energy as a functional of the on-top pair density, which is simply the diagonal of the 2-RDM in its real-space representation. We have explored this MCPDFT-based strategy due to the conceptual and computational simplicity of the approach.

In the approach to MCPDFT outlined in Ref. 5, the on-top pair density functional is approximated by a standard functional of the spin density and gradient of the spin density; the input spin density and gradient are "translated" versions of these quantities that incorporate knowledge of the on-top pair density. In this way, given a translated spin density and gradient, one can in principle apply MCPDFT using any number of standard density functionals. Reference 6 describes a slightly more complicated "fully translated" version of the approach that retains the simplicity of the procedure proposed in Ref. 5. We developed a pilot version of the MCPDFT approach that employs RDMs from v2RDM-CASSCF as a plugin to the Psi4 package. More recently, we have ported this code to a development version of Q-Chem. We have generalized the interface between our MCPDFT code and Q-Chem so that MCPDFT can be combined with any multiconfigurational method, not just the v2RDM-CASSCF approach. Potential underlying methods of interest implemented in Q-Chem include complete active space adaptive sampling configuration interaction, nonorthogonal configuration interaction, spin-flip DFT, spin-flip equation-of-motion coupled cluster methods, and restricted active space spin flip methods.

We have submitted a manuscript describing our pilot MCPDFT implementation and exploring its accuracy for some common multireference problems. As an example, Fig. 4 illustrates the potential energy curve for the dissociation of molecular nitrogen in the cc-pVTZ basis set. The v2RDM-CASSCF and reference CASPT2 results employed a (6e, 6o) active space. Also included in this figure are v2RDM-CASSCF + MCPDFT results for the translated PBE, SVWN, and BLYP functionals (denoted tPBE, tSVWN, and tBLYP, respectively). We can draw several conclusions from these data. First, none of the PDFT methods yield the correct dissociation limit, and these limits vary wildly depending on the choice of functional. Nonetheless, the shapes of each potential energy curve are reasonable. In this case, the best performing functional is tPBE, which slightly overestimates the dynamical correlation effects absent in the v2RDM-CASSCF energy. Figure 5 illustrates the potential energy curves for the same system using the "fully translated" functionals [5] (denoted by "ft"). We see here that the fully translated variants of each functional yield curves of essentially the same shape as the translated variants, but the total energies in all cases are slightly lower. It appears that, for this system, full translation does not do

much to improve the quality of any of the curves, and thus the translated PBE functional provides the best results overall, relative to the CASPT2 reference.

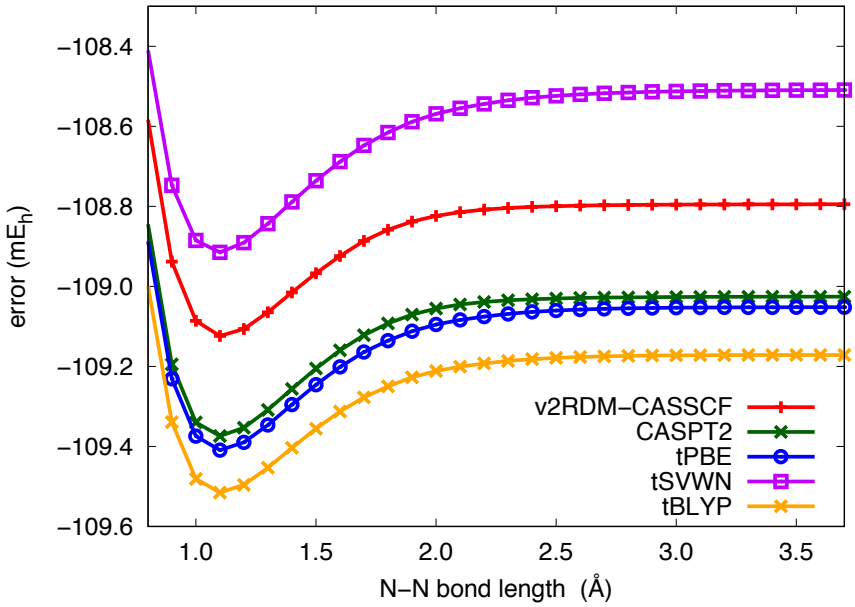

Figure 4. Potential energy curves for the dissociation of molecular nitrogen in the cc-pVTZ basis set. PDFT computations employed "translated" functionals [5].

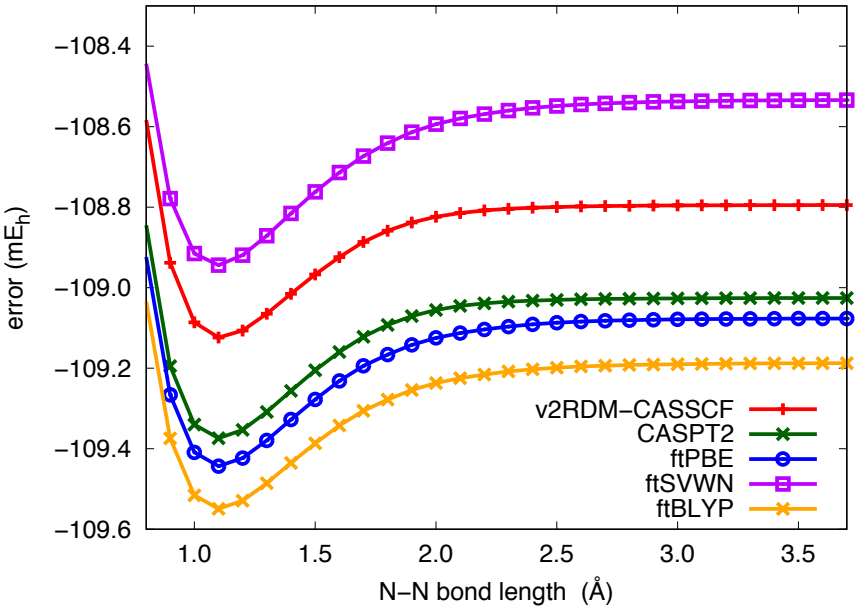

Figure 5. Potential energy curves for the dissociation of molecular nitrogen in the cc-pVTZ basis set. PDFT computations employed "fully translated" functionals [6].

Regarding excited-state computations, we originally intended to port a previously developed[7] implementation of the extended random phase approximation (ERPA)[8] to Q-Chem for computing excitations out of v2RDM-CASSCF ground states. However, the ERPA appears to be

somewhat less reliable for computing excited states than we anticipated, and further theoretical developments outside the scope of this STTR are required before a useful, production-level ERPA-based excited-state module can be developed.

[1] C. Garrod and J. K. Percus, *J. Math. Phys.* **5**, 1756-1776 (1964).
[2] Z. Zhao, B. J. Braams, M. Fukuda, M. L. Overton, and J. K. Percus, *J. Chem. Phys.* **120**, 2095-2104 (2004).
[3] E. Epifanovsky, M. Wormit, T. Ku, A. Landau, D. Zuev, K. Khistyaev, P. Manohar, I. Kaliman, A. Dreuw, and A. I. Krylov, J. Comput. Chem. **34**, 2293 (2013).
[4] J. Fosso-Tande, T.-S. Nguyen, G. Gidofalvi, A. E. DePrince, III. *J. Chem. Theory Comput.* **12**, 2260-2271 (2016).
[5] G. Li Manni, R. K. Carlson, S. Luo, D. Ma, J. Olsen, D. G. Truhlar, L. Gagliardi, *J. Chem. Theory Comput.* **10**, 3669 (2014).
[6] R. K. Carlson, D. G. Truhlar, L. Gagliardi, *J. Chem. Theory Comput.* **11**, 4077-4085 (2015).
[7] A. E. DePrince, III, *J. Chem. Phys.* **145**, 164109 (2016).
[8] K. Chatterjee and K. Pernal, *J. Chem. Phys.* **137**, 204109 (2012).

The following pages are the v2RDM-specific portion of the Q-Chem 5.1 manual.

remaining geminals are:

Geminal 10 E = -1.342609
0.99128 -0.12578 -0.03563 -0.01149 -0.01133 -0.00398

Geminal 11 E = -0.757086
0.96142 -0.17446 -0.16872 -0.12414 -0.03187 -0.01227 -0.01204 -0.00435 -0.00416 -0.00098

Mulliken population analysis shows that geminal 10 is delocalized between Sc and H, indicating a bond. It is moderately correlated, with second expansion coefficient of a magnitude 0.126. The geminal of highest energy is localized on Sc. It represents $4s^2$ electrons and describes their excitation into $3d$ orbitals. Presence of three large expansion coefficients show that this effect cannot be described within GVB framework.[13]

6.16.2 Perturbative Corrections

The SSG description of molecular electronic structure can be improved by perturbative description of missing inter-geminal correlation effects. We have implemented Epstein-Nesbet form of perturbation theory[27,73] that permits a balanced description of one- and two-electron contributions to excited states' energies in SSG model. This form of perturbation theory is especially accurate for calculation of weak intermolecular forces. Also, two-electron $[i\bar{j}, j\bar{i}]$ integrals are included in the reference Hamiltonian in addition to intra-geminal $[i\bar{j}, i\bar{j}]$ integrals that are needed for reference wave function to be an eigenfunction of the reference Hamiltonian.[83]

All perturbative contributions to the SSG(EN2) energy (second-order Epstein-Nesbet perturbation theory of SSG wave function) are analyzed in terms of largest numerators, smallest denominators, and total energy contributions by the type of excitation. All excited states are subdivided into dispersion-like with correlated excitation within one geminal coupled to the excitation within another geminal, single, and double electron charge transfer. This analysis permits careful assessment of the quality of SSG reference wave function. Formally, the SSG(EN2) correction can be applied both to RSSG and USSG wave functions. Experience shows that molecules with broken or nearly broken bonds may have divergent RSSG(EN2) corrections. USSG(EN2) theory is balanced, with largest perturbative corrections to the wave function rarely exceeding 0.1 in magnitude.

SSG
Controls the calculation of the SSG wave function.
TYPE:
INTEGER
DEFAULT:
0
OPTIONS:
0 Do not compute the SSG wave function
1 Do compute the SSG wave function
RECOMMENDATION:
See also the UNRESTRICTED and DIIS_SUBSPACE_SIZE *$rem* variables.

6.17 Variational Two-Electron Reduced-Density-Matrix Methods

6.17.1 Introduction

The methods described in this section involve the direct variational optimization of the two-electron reduced-density matrix (2-RDM, $^2\mathbf{D}$), subject to necessary ensemble N-representability conditions.[29,30,34,35,71,85] Such conditions place restrictions on the 2-RDM in order to ensure that it is derivable from an antisymmetrized N-electron wavefunction. In

the limit that the N-representability of the 2-RDM is exactly enforced, the variational 2-RDM (v2RDM) approach is equivalent to full configuration interaction (CI). Such computations are, in general, computationally infeasible, so the v2RDM optimization is typically carried out under a subset of two- or three-particle conditions. When only partially enforcing N-representability, the v2RDM approach yields a lower bound to the full CI energy.

In Q-Chem, all v2RDM optimizations are carried out under the following conditions:

- the 2-RDM is positive semidefinite
- the one-electron reduced-density matrix (1-RDM) is positive semidefinite
- the trace of the 2-RDM is equal to the number of pairs of electrons, $N(N-1)$
- each spin block of the 2-RDM properly contracts to the appropriate spin block of the 1-RDM
- the expectation value of $\hat{M}_S$ is $\frac{1}{2}(N_\alpha - N_\beta)$ (the maximal spin projection)

Additionally, an optional spin constraint can be placed on the 2-RDM such that $\langle S^2 \rangle = S(S+1)$, where the S is the spin quantum number. Note that this constraint on the expectation value of $\hat{S}^2$ does not strictly guarantee that the 2-RDM corresponds to an eigenfunction of $\hat{S}^2$. Without additional constraints, a v2RDM optimization would yield poor-quality 2-RDMs with energies far below those of full CI. Reasonable results require, at a minimum, that one enforce the positivity of additional pair-probability density matrices, including the two-hole reduced-density matrix (${}^2\mathbf{Q}$) and the particle-hole reduced-density matrix (${}^2\mathbf{G}$). The positivity of ${}^2\mathbf{D}$, ${}^2\mathbf{Q}$, and ${}^2\mathbf{G}$ constitute the DQG constraints of Garrod and Percus.[35] For many systems, the DQG constraints yield a reasonable description of the electronic structure. However, if high accuracy is desired, it is sometimes necessary to consider constraints on higher-order reduced-density matrices (e.g. the three-electron reduced-density matrix [3-RDM]). In Q-Chem, v2RDM optimizations can be performed under the T1 and T2 partial three-particle conditions,[28,110] which do not explicitly depend upon the 3-RDM. The positivity conditions imposed in v2RDM computations are controlled through the *$rem* keyword RDM_POSITIVITY.

The main utility of the v2RDM approach is in the context of active-space-based descriptions of strong or nondynamical correlation. The most common active-space-based approach for strong correlation is the compete active space self-consistent field (CASSCF) method. By performing a v2RDM computation within an active space and coupling v2RDM to an orbital optimization procedure, one can achieve a v2RDM-driven CASSCF procedure[32,36,69] that provides a lower bound the conventional CI-based CASSCF energy. Because the v2RDM-CASSCF method scales polynomially with respect to the number of active orbitals, v2RDM-CASSCF can handle much larger active spaces (e.g., 50 electrons in 50 orbitals) compared to CI-CASSCF (e.g., 18 electrons in 18 orbitals).

The current v2RDM and v2RDM-CASSCF implementations can make use of the density fitting (DF) approximation to the two-electron integrals. The use of DF integrals is particularly advantageous for v2RDM-CASSCF computations with large active spaces because of the increased efficiency in the orbital optimization/integral transformation step. The use of DF integrals is triggered by using the *$rem* keyword AUX_BASIS. Analytic gradients are only available for DF integrals and are not available when frozen molecular orbitals are requested. Specification of the active space is demonstrated in the examples below. Additionally, a GPU-accelerated implementation of v2RDM and v2RDM-CASSCF employing the DQG conditions is available.

6.17.2 Theory

The electronic energy is an exact functional of the 1-RDM and 2-RDM

$$E = \frac{1}{2} \sum_{pqrs} {}^2D^{pq}_{rs}(pr|qs) + \sum_{pq} {}^1D^p_q h_{pq}, \tag{6.48}$$

where the 1-RDM (${}^1\mathbf{D}$) and 2-RDM are represented in a given spin-orbital basis indexed by p, q, r, and s. The one-hole RDM (${}^1\mathbf{Q}$), ${}^2\mathbf{Q}$, ${}^2\mathbf{G}$, and partial three-particle RDMs ($\mathbf{T1}$ and $\mathbf{T2}$) are linear functions of ${}^1\mathbf{D}$ and ${}^2\mathbf{D}$.[32] Minimizing the electronic energy with respect to ${}^2\mathbf{D}$ while enforcing the linear relations among these RDMs, the contraction and

spin constraints placed on ${}^2\mathbf{D}$, and the positive semidefinite property of all RDMs constitutes a semidefinite program (SDP). The current v2RDM implementation uses a boundary-point SDP (BPSDP) algorithm to solve the SDP.[68,70,76]

The primal formulation of the SDP is

$$\begin{aligned} \text{minimize} \quad & E_{\text{primal}} = \mathbf{c}^T \cdot \mathbf{x} \\ \text{such that} \quad & \mathbf{A}\mathbf{x} = \mathbf{b} \\ \text{and} \quad & M(\mathbf{x}) \succeq 0. \end{aligned} \tag{6.49}$$

Here, $\mathbf{x}$ represents the primal solution vector, the vector $\mathbf{c}$ contains all information defining the quantum system (the one- and two-electron integrals), and the mapping $M(\mathbf{x})$ maps the primal solution onto the set of positive semidefinite RDMs

$$M(\mathbf{x}) = \begin{pmatrix} {}^1\mathbf{D} & 0 & 0 & 0 & 0 & 0 & 0 \\ 0 & {}^1\mathbf{Q} & 0 & 0 & 0 & 0 & 0 \\ 0 & 0 & {}^2\mathbf{D} & 0 & 0 & 0 & 0 \\ 0 & 0 & 0 & {}^2\mathbf{Q} & 0 & 0 & 0 \\ 0 & 0 & 0 & 0 & {}^2\mathbf{G} & 0 & 0 \\ 0 & 0 & 0 & 0 & 0 & \mathbf{T1} & 0 \\ 0 & 0 & 0 & 0 & 0 & 0 & \mathbf{T2} \end{pmatrix} \succeq 0. \tag{6.50}$$

The action of the constraint matrix, $\mathbf{A}$, on $\mathbf{x}$ is a compact representation of the N-representability conditions. $\mathbf{A}$ maintains the appropriate mappings between each block of $M(\mathbf{x})$ and enforces the appropriate spin and contraction conditions. Alternatively, one could consider the dual formulation of the semidefinite problem, expressed as

$$\begin{aligned} \text{maximize} \quad & E_{\text{dual}} = \mathbf{b}^T \cdot \mathbf{y} \\ \text{such that} \quad & \mathbf{z} = \mathbf{c} - \mathbf{A}^T\mathbf{y} \\ \text{and} \quad & M(\mathbf{z}) \succeq 0 \end{aligned} \tag{6.51}$$

where $\mathbf{y}$ and $\mathbf{z}$ are the dual solutions, and $M(\mathbf{z})$ is constrained to be positive semidefinite.

The BPSDP algorithm involves an iterative two-step procedure:

1. Solve $\mathbf{A}\mathbf{A}^T\mathbf{y} = \mathbf{A}(\mathbf{c} - \mathbf{z}) + \tau\mu(\mathbf{b} - \mathbf{A}\mathbf{x})$ for $\mathbf{y}$ by conjugate gradient methods.
2. Update $\mathbf{x}$ and $\mathbf{z}$ by separating $\mathbf{U} = M(\mu\mathbf{x} + \mathbf{A}^T\mathbf{y} - \mathbf{c})$ into its positive and negative components (by diagonalization). The updated primal and dual solutions $\mathbf{x}$ and $\mathbf{z}$ are given by $M(\mathbf{x}) = \mathbf{U}(+)/\mu$ and $M(\mathbf{z}) = -\mathbf{U}(-)$.

Here, τ is a step-length parameter that lies in the interval [1.0,1.6][70]. The penalty parameter μ controls how strictly the primal or dual constraints are enforced and is updated dynamically according to the protocol outlined in Ref. 70. The frequency with which μ is updated is controlled by the *$rem* keyword RDM_MU_UPDATE_FREQUENCY. The algorithm is considered converged when the primal error $||\mathbf{A}\mathbf{x} - \mathbf{b}||$, the dual error $||\mathbf{A}^T\mathbf{y} - \mathbf{c} + \mathbf{z}||$, and the primal/dual energy gap $|E_{\text{primal}} - E_{\text{dual}}|$ are sufficiently small. The convergence in the primal/dual errors and the primal/dual energy gap are controlled by the *$rem* keywords RDM_EPS_CONVERGENCE and RDM_E_CONVERGENCE, respectively. The BPSDP algorithm scales n^6 for the DQG conditions and n^9 for the T1 and T2 conditions where n is the number of active orbitals in the v2RDM computation. In v2RDM-CASSCF (if the *$rem* keyword RDM_OPTIMIZE_ORBITALS is set to true), the molecular orbitals are optimized after a chosen number of v2RDM iterations (Steps 1. and 2. above) indicated by the *$rem* keyword RDM_ORBOPT_FREQUENCY.

6.17.3 Examples

Example 6.32 Single-point v2RDM/STO-3G energy computation.

```
$molecule
    0 1
    O  0.0000  0.0000  0.1173
    H  0.0000  0.7572 -0.4692
    H  0.0000 -0.7572 -0.4692
$end

$rem
    jobtype                         sp
    basis                           sto-3g
    method                          rdm
    unrestricted                    false
    rdm_solver                      vector
    rdm_positivity                  dqg
    rdm_constrain_spin              true
    rdm_mu_update_frequency         200
    rdm_eps_convergence             4
    rdm_e_convergence               4
    rdm_maxiter                     500000
    rdm_tau                         10
    rdm_print                       1
    rdm_optimize_orbitals           false
$end
```

Example 6.33 Single-point v2RDM/STO-3G energy computation with frozen core orbital.

```
$molecule
    0 1
    O  0.0000  0.0000  0.1173
    H  0.0000  0.7572 -0.4692
    H  0.0000 -0.7572 -0.4692
$end

$rem
    jobtype                         sp
    basis                           sto-3g
    method                          rdm
    unrestricted                    false
    rdm_solver                      vector
    rdm_positivity                  dqg
    rdm_constrain_spin              true
    rdm_mu_update_frequency         200
    rdm_eps_convergence             4
    rdm_e_convergence               4
    rdm_maxiter                     500000
    rdm_tau                         10
    rdm_print                       1
    rdm_optimize_orbitals           false
$end

$rdm_active_space
1 0 0 0   ! frozen orbitals
0 0 0 0 ! restricted orbitals
3 0 2 1 ! active orbitals
$end
```

Example 6.34 Single-point v2RDM-CASSCF/cc-pVDZ energy computation.

```
$molecule
    0 1
    O  0.0000  0.0000  0.1173
    H  0.0000  0.7572 -0.4692
    H  0.0000 -0.7572 -0.4692
$end

$rem
    jobtype                         sp
    basis                           cc-pvdz
    method                          rdm
    unrestricted                    false
    rdm_solver                      vector
    rdm_positivity                  dqg
    rdm_constrain_spin              true
    rdm_mu_update_frequency         200
    rdm_eps_convergence             4
    rdm_e_convergence               4
    rdm_maxiter                     500000
    rdm_tau                         10
    rdm_print                       1
    rdm_optimize_orbitals           true
    rdm_orbopt_energy_convergence   7
    rdm_orbopt_gradient_convergence 4
    rdm_orbopt_frequency            500
    rdm_orbopt_maxiter              5
$end

$rdm_active_space
0 0 0 0 ! frozen orbitals
1 0 0 0 ! restricted orbitals
3 0 2 1 ! active orbitals
$end
```

6.17.4 v2RDM Job Control

RDM_POSITIVITY

Indicates positivity conditions enforced in the v2RDM optimization.

TYPE:

STRING

DEFAULT:

DQG

OPTIONS:

DQG,	Two-electron conditions
DQGT1	Two-electron conditions plus the T1 partial three-electron conditions
DQGT2	Two-electron conditions plus the T2 partial three-electron conditions
DQGT1T2	Two-electron conditions plus the T1 and T2 partial three-electron conditions

RECOMMENDATION:

Use DQGT1T2 or DQGT2 for best accuracy, but such computations may become infeasible for large active spaces.

RDM_E_CONVERGENCE

The threshold for the primal-dual energy gap.

TYPE:

INTEGER

DEFAULT:

4

OPTIONS:

N for a threshold of 10^{-N}

RECOMMENDATION:

Increase for gradient computations.

RDM_EPS_CONVERGENCE

The threshold for the error in the primal and dual constraints.

TYPE:

INTEGER

DEFAULT:

4

OPTIONS:

N for a threshold of 10^{-N}

RECOMMENDATION:

Increase for gradient computations.

RDM_MAXITER

Maximum number of diagonalization steps in the BPSDP solver.

TYPE:

INTEGER

DEFAULT:

50000

OPTIONS:

$N > 0$

RECOMMENDATION:

Increase for computations that are difficult to converge.

RDM_CG_CONVERGENCE

The minimum threshold for the conjugate gradient solver.

TYPE:

INTEGER

DEFAULT:

12

OPTIONS:

N for a threshold of 10^{-N}

RECOMMENDATION:

Should be at least (RDM_EPS_CONVERGENCE+2).

RDM_CG_MAXITER

Maximum number of iterations for each conjugate gradient computations in the BPSDP algorithm.

TYPE:

INTEGER

DEFAULT:

1000

OPTIONS:

$N > 0$

RECOMMENDATION:

Use default unless problems arise.

RDM_TAU

Step-length parameter used in the BPSDP solver.

TYPE:

INTEGER

DEFAULT:

10

OPTIONS:

N for a value of 0.1 * N

RECOMMENDATION:

RDM_TAU should range between 10 and 16 for $1.0 \leq \tau \leq 1.6$.

RDM_MU_UPDATE_FREQUENCY

The number of v2RDM iterations after which the penalty parameter μ is updated.

TYPE:

INTEGER

DEFAULT:

200

OPTIONS:

$N > 0$

RECOMMENDATION:

Change if convergence problems arise.

RDM_SOLVER

Indicates which solver to use for the v2RDM optimization.

TYPE:

STRING

DEFAULT:

VECTOR

OPTIONS:

VECTOR	Picks the hand-tuned loop-based code.
BLOCK_TENSOR	Picks the libtensor-based code.

RECOMMENDATION:

Use the default.

RDM_CONSTRAIN_SPIN

Indicates if the spin-constraints are enforced.

TYPE:

BOOLEAN

DEFAULT:

TRUE

OPTIONS:

TRUE Enforce spin-constraints.

FALSE Do not enforce spin-constraints.

RECOMMENDATION:

Use default.

RDM_OPTIMIZE_ORBITALS

Indicates if the molecular orbitals will be optimized.

TYPE:

BOOLEAN

DEFAULT:

TRUE

OPTIONS:

TRUE Optimize orbitals.

FALSE Do not optimize orbitals.

RECOMMENDATION:

Use default unless all orbitals are active.

RDM_ORBOPT_FREQUENCY

The number of v2RDM iterations after which the orbital optimization routine is called.

TYPE:

INTEGER

DEFAULT:

500

OPTIONS:

$N > 0$

RECOMMENDATION:

Use default unless convergence problems arise.

RDM_ORBOPT_GRADIENT_CONVERGENCE

The threshold for the orbital gradient during orbital optimization.

TYPE:

INTEGER

DEFAULT:

4

OPTIONS:

N for threshold of 10^{-N}

RECOMMENDATION:

Tighten for gradient computations.

RDM_ORBOPT_ENERGY_CONVERGENCE

The threshold for energy convergence during orbital optimization.

TYPE:

INTEGER

DEFAULT:

8

OPTIONS:

N for threshold of 10^{-N}

RECOMMENDATION:

Tighten for gradient computations.

RDM_ORBOPT_MAXITER

The maximum number of orbital optimization steps each time the orbital optimization routine is called.

TYPE:

INTEGER

DEFAULT:

20

OPTIONS:

$N > 0$

RECOMMENDATION:

Use default unless convergence problems arise.

RDM_PRINT

Controls the amount of printing.

TYPE:

INTEGER

DEFAULT:

0

OPTIONS:

0 Print minimal information.

1 Print information about all iterations.

RECOMMENDATION:

Use 1 to analyze convergence issues.

Analytic energy gradients for variational two-electron reduced-density matrix methods within the density-fitting approximation

J. Wayne Mullinax,[1] Evgeny Epifanovsky,[2] Gergely Gidofalvi,[3] and A. Eugene DePrince III[1]

[1] *Department of Chemistry and Biochemistry, Florida State University, Tallahassee, FL 32306*
[2] *Q-Chem, Inc., 6601 Owens Drive, Suite 105, Pleasanton, CA 94588*
[3] *Department of Chemistry and Biochemistry, Gonzaga University, Spokane, Washington 99258*

Analytic energy gradients are presented for a variational two-electron reduced-density-matrix-driven complete active space self-consistent field (v2RDM-CASSCF) procedure that employs the density-fitting (DF) approximation to the two-electron repulsion integrals. The DF approximation significantly reduces the computational cost of v2RDM-CASSCF gradient evaluation, in terms of both the number of floating-point operations and memory requirements, enabling geometry optimizations on much larger chemical systems than could previously be considered at the this level of theory [E. Maradzike *et al.*, *J. Chem. Theory Comput*, 2017, **13**, 4113–4122]. The efficacy of v2RDM-CASSCF for computing equilibrium geometries and harmonic vibrational frequencies is assessed using a set of 25 small closed- and open-shell molecules. Equilibrium bond lengths from v2RDM-CASSCF differ from those obtained from configuration-interaction-driven CASSCF (CI-CASSCF) by 0.62 pm and 0.05 pm, depending on whether the optimal reduced-density matrices from v2RDM-CASSCF satisfy two-particle N-representability conditions (PQG) or PQG plus partial three-particle conditions (PQG+T2), respectively. Harmonic vibrational frequencies, which are obtained by finite differences of v2RDM-CASSCF analytic energy gradients, similarly demonstrate that quantitative agreement between v2RDM- and CI-CASSCF requires the consideration of partial three-particle N-representability conditions. Lastly, optimized geometries are obtained for the lowest-energy singlet and triplet states of the linear polyacene series up to dodecacene ($C_{50}H_{28}$), in which case the active space is comprised of 50 electrons in 50 orbitals. The v2RDM-CASSCF singlet-triplet energy gap extrapolated to an infinitely-long linear acene molecule is found to be 7.8 kcal mol^{-1}.

I. INTRODUCTION

Nondynamical correlation effects in large molecular systems are notoriously difficult to model, particularly as the number of strongly-correlated electrons increases. For small systems, the complete active space self-consistent field (CASSCF) method[1–4] provides a reliable zeroth-order description of the electronic structure that can be improved by the additional consideration of dynamical correlation effects, for example, through perturbation theory [5]. However, the steep computational scaling of configuration-interaction (CI) based descriptions of the electronic structure of the active space limits the applicability of CI-CASSCF to active spaces comprised of at most 20 electrons in 20 orbitals.[6] As a result, several approximations to CASSCF that are also based on a CI-type *ansatz* have been proposed, including the restricted active space self-consistent field,[7, 8] the generalized active space (GAS) self-consistent field,[9, 10] the split GAS,[11] the occupation-restricted multiple active spaces self-consistent field,[12] and full CI quantum Monte Carlo self-consistent field methods.[13, 14] While these methods are applicable to larger active spaces than are permitted by current CI-CASSCF implementations, abandoning the CI-based *ansatz* altogether allows one to achieve formally polynomially-scaling approximations to CASSCF. For example, one of the most popular alternatives to the CI parameterization of the wave function expansion is the density-matrix renormalization group (DMRG) approach, wherein the wave function is expressed as a matrix product state.[15–27] An approximation to CASSCF can be achieved by coupling a DMRG calculation within an active space to an orbital optimization scheme.[28–33] The result is a polynomially-scaling method that can treat large active spaces required, for example, in extended π-conjugated molecules, transition metal dimers, and organometallic complexes.[24]

Alternatively, the electronic structure of the active space can be described without considering *any* wave function parameterization. The key to this strategy is the realization that the electronic Hamiltonian contains at most two-body interactions, and, as such, the electronic energy can be evaluated exactly with knowledge of the two-electron reduced-density matrix (2RDM). The allure of replacing the wave function with the 2RDM lies in the fact that the latter offers a far more compact representation of electronic structure than that offered by the exact wave function. The 2RDM can be determined directly by minimizing the energy with respect to variations in its elements, subject to a set of N-representability conditions, which are constraints placed on the 2RDM to ensure that it is derived from an N-electron wave function.[34–49] By coupling an orbital optimization to a variational 2RDM (v2RDM) based description of the active space, one can achieve a v2RDM-driven approximation to CASSCF that scales polynomially with respect to the number of active orbitals.[50, 51]

We have recently described software to compute v2RDM-CASSCF energies[51] and analytic energy gradients,[52] which is avaiable as a plugin[53] to the Psi4

electronic structure package.[54, 55] This implementation has been applied to energy computations involving active spaces as large as 50 electrons in 50 orbitals with the simultaneous optimization of 1892 orbitals.[51] The consideration of large numbers of external orbitals in energy computations is facilitated by the use of the density-fitting (DF) approximation to the electron repulsion integrals (ERIs),[56–59] which leads to significant decreases in the storage requirements and floating-point cost of the orbital optimization procedure. However, the analytic energy gradient implementation described in Ref. 52 employs only conventional ERIs, which limits its applicability to modestly sized systems and basis sets. In this paper, we describe a new implementation of analytic energy gradients for v2RDM-CASSCF that employs the DF approximation to the ERIs and is thus applicable to much larger molecular systems. This new implementation is available in version 5.1 of the Q-Chem electronic structure package.[60]

This paper is organized as follows. In Sec. II, we review the theoretical details of v2RDM-CASSCF, summarize the semidefinite optimization algorithm used within our software, and present the analytic gradient expressions. In Sec. IV, we benchmark the method by comparing v2RDM-CASSCF equilibrium geometries and harmonic vibrational frequencies for a set of 25 molecules to those computed with conventional CASSCF and to those derived from experiment. We then demonstrate the applicability of the code to large systems by computing the singlet-triplet energy gap of the linear acene series up to dodecacene ($C_{50}H_{28}$) using v2RDM-CASSCF optimized geometries. Computational details can be found in Sec. III.

II. THEORY

In this Section, we summarize the theoretical details underlying the v2RDM-CASSCF energy optimization procedure and v2RDM-CASSCF analytic gradient evaluation in the case that the ERIs are represented within the DF approximation. We employ a set of orthonormal molecular orbitals (MOs) indexed by p, q, r, and s throughout. The MOs are partitioned into a set of inactive (doubly occupied) orbitals indexed by i, j, k, and l; a set of active orbitals indexed by t, u, v, w, x, and y; and a set of external orbitals. When spin labels are employed and these labels are not explicitly specified as α or β, general spin labels are indicated by σ, τ, κ, λ, μ, and ν. The auxiliary basis functions employed within the DF approximation are indexed by P, Q, R, and S. For the sake of brevity, we will refer to v2RDM-CASSCF computations performed subject to PQG or PQG+T2 conditions simply as PQG and PQG+T2. Table I summarizes this notation.

TABLE I: Summary of Notation

Label	Summary
p, q, r, s	general molecular orbitals
i, j, k, l	inactive (doubly occupied) orbitals
t, u, v, w, x, y	active orbitals
P, Q, R, S	auxiliary basis functions
$\sigma, \tau, \kappa, \lambda, \mu, \nu$	spin functions
PQG	v2RDM-CASSCF subject to the PQG conditions
PQG+T2	v2RDM-CASSCF subject to the PQG+T2 conditions

A. CASSCF energy and density

The non-relativistic electronic energy for a many-electron system is given by

$$E = \sum_{pq}(T_{pq} + V_{pq})\gamma_{pq} + \sum_{pqrs}(pq|rs)\Gamma_{pqrs}, \tag{1}$$

where T_{pq} and V_{pq} represent the electron kinetic energy and electron-nuclear potential energy integrals, respectively, $(pq|rs)$ represents an element of the ERI tensor, and γ_{pq} and Γ_{pqrs} represent elements of the spin-free one-electron reduced-density matrix (1RDM) and the spin-free 2RDM, respectively. For a CASSCF wave function, $\boldsymbol{\gamma}$ and $\boldsymbol{\Gamma}$ exhibit block structure based on the partitioning of the orbitals. The non-zero blocks of $\boldsymbol{\gamma}$ are

$$\gamma_{ij} = 2\delta_{ij}, \tag{2}$$

and

$$\gamma_{tu} = {}^1D^{t_\alpha}_{u_\alpha} + {}^1D^{t_\beta}_{u_\beta}, \tag{3}$$

and the elements of the spin blocks that comprise the active-active block of $\boldsymbol{\gamma}$ are defined as

$${}^1D^{t_\sigma}_{u_\sigma} = \langle\Psi|\hat{a}^\dagger_{t_\sigma}\hat{a}_{u_\sigma}|\Psi\rangle\,, \tag{4}$$

where $\hat{a}^\dagger$ and $\hat{a}$ represent creation and annihilation operators of second quantization, respectively. The non-zero elements of $\boldsymbol{\Gamma}$ are

$$\Gamma_{ijkl} = 2\delta_{ij}\delta_{kl} - \delta_{il}\delta_{jk}, \tag{5}$$

$$\Gamma_{ijtu} = \Gamma_{tuij} = \gamma_{tu}\delta_{ij}, \tag{6}$$

$$\Gamma_{iutj} = \Gamma_{tjiu} = -\frac{1}{2}\gamma_{tu}\delta_{ij}, \tag{7}$$

and

$$\Gamma_{tuvw} = \frac{1}{2}\Big(\,{}^2D^{t_\alpha v_\alpha}_{u_\alpha w_\alpha} + {}^2D^{t_\alpha v_\beta}_{u_\alpha w_\beta} + {}^2D^{t_\beta v_\alpha}_{u_\beta w_\alpha} + {}^2D^{t_\beta v_\beta}_{u_\beta w_\beta}\Big), \tag{8}$$

where the elements of the active-space spin-blocks are defined by

$${}^2D^{t_\sigma v_\tau}_{u_\sigma w_\tau} = \langle\Psi|\hat{a}^\dagger_{t_\sigma}\hat{a}^\dagger_{v_\tau}\hat{a}_{w_\tau}\hat{a}_{u_\sigma}|\Psi\rangle\,. \tag{9}$$

Given the block structure of $\boldsymbol{\gamma}$ and $\boldsymbol{\Gamma}$, Eq. 1 can be reexpressed as

$$E \;=\; E_{\rm core} + E_{\rm active} \tag{10}$$

where

$$E_{\rm core} = 2\sum_i (T_{ii} + V_{ii}) + \sum_{ij}[2(ii|jj) - (ij|ij)], \tag{11}$$

and

$$E_{\rm active} = \sum_{tu} h_{tu}\gamma_{tu} + \sum_{tuvw}(tu|vw)\Gamma_{tuvw}. \tag{12}$$

Here, the one-electron matrix elements, h_{tu}, are defined by

$$h_{tu} = T_{tu} + V_{tu} + \sum_i [2(ii|tu) - (iu|it)]. \tag{13}$$

The ERIs entering Eqs. 11-13 are computed using the DF approximation; we have

$$(pq|rs) \;\approx\; (pq|rs)_{\rm DF} = \sum_P B^P_{pq} B^P_{rs}, \tag{14}$$

and the coefficients, B^P_{pq}, are determined using the Coulomb metric as

$$B^P_{pq} \;=\; \sum_Q (pq|Q) V^{-1/2}_{QP} \tag{15}$$

where

$$V_{PQ} = (P|Q) = \int {\rm d}\mathbf{r}_1 \int {\rm d}\mathbf{r}_2 \; \chi_P(\mathbf{r}_1)\chi_Q(\mathbf{r}_2)/r_{12}, \tag{16}$$

and χ_P and χ_Q represent auxiliary basis functions.

B. N-representability

In v2RDM-CASSCF, the active-space 2RDM is determined by minimizing the energy with respect to variations in its elements, subject to constraints intended to guarantee that the 2RDM is derivable from an ensemble of antisymmetrized N-electron wavefunctions (such a 2RDM is said to be ensemble N-representable [61]). Here, we outline some necessary ensemble N-representability conditions. First, an ensemble N-representable 2RDM is Hermitian

$${}^2D^{t_\sigma u_\tau}_{v_\sigma w_\tau} = {}^2D^{v_\sigma w_\tau}_{t_\sigma u_\tau}, \tag{17}$$

and it is antisymmetric with respect to the exchange of its indices

$${}^2D^{t_\sigma u_\tau}_{v_\sigma w_\tau} = -{}^2D^{u_\tau t_\sigma}_{v_\sigma w_\tau} = -{}^2D^{t_\sigma u_\tau}_{w_\tau v_\sigma} = {}^2D^{u_\tau t_\sigma}_{w_\tau v_\sigma}. \tag{18}$$

Second, the 2RDM should map onto the 1RDM through a set of contractions given by

$$(N_\sigma - 1)\,{}^1D^{t_\sigma}_{u_\sigma} = \sum_v {}^2D^{t_\sigma v_\sigma}_{u_\sigma v_\sigma}, \tag{19}$$

and

$$N_\sigma\,{}^1D^{t_\tau}_{u_\tau} = \sum_v {}^2D^{t_\tau v_\sigma}_{u_\tau v_\sigma} \quad \text{for} \;\; \sigma \neq \tau \tag{20}$$

where N_σ is the number of active electrons with spin σ. The trace of the 2RDM must also preserve the number of pairs of electrons, according to

$$\sum_{tu} {}^2D^{t_\sigma u_\sigma}_{t_\sigma u_\sigma} = N_\sigma(N_\sigma - 1), \tag{21}$$

and

$$\sum_{tu} {}^2D^{t_\sigma u_\tau}_{t_\sigma u_\tau} = N_\sigma N_\tau \quad \text{for} \;\; \sigma \neq \tau. \tag{22}$$

Moreover, because the eigenvalues of the 1RDM and 2RDM can be interpreted as occupation numbers for natural orbitals and geminals, respectively, both of these matrices should be positive semidefinite:

$${}^1\mathbf{D} \;\succeq\; 0 \tag{23}$$

$${}^2\mathbf{D} \;\succeq\; 0 \tag{24}$$

Additional ensemble N-representability conditions can be obtained by considering the positivity of other reduced-density matrices (RDMs) that are related to the 1RDM and 2RDM. For example, the algebra of the creation and annihilation operators implies linear relations that map the 1RDM and 2RDM to the one-hole RDM ($^1\mathbf{Q}$), the two-hole RDM ($^2\mathbf{Q}$), and the electron-hole RDM ($^2\mathbf{G}$), the elements of which are defined as

$${}^1Q^{t_\sigma}_{u_\sigma} = \langle\Psi|\hat{a}_{t_\sigma}\hat{a}^\dagger_{u_\sigma}|\Psi\rangle\,, \tag{25}$$

$${}^2Q^{t_\sigma u_\tau}_{v_\sigma w_\tau} = \langle\Psi|\hat{a}_{t_\sigma}\hat{a}_{u_\tau}\hat{a}^\dagger_{w_\tau}\hat{a}^\dagger_{v_\sigma}|\Psi\rangle\,, \tag{26}$$

and

$${}^2G^{t_\sigma u_\tau}_{v_\kappa w_\lambda} = \langle\Psi|\hat{a}^\dagger_{t_\sigma}\hat{a}_{u_\tau}\hat{a}^\dagger_{w_\lambda}\hat{a}_{v_\kappa}|\Psi\rangle\,. \tag{27}$$

The N-representability of the 2RDM requires that each of these matrices be positive semidefinite; these constraints comprise the "PQG" constraints of Garrod and Percus.[34]. In this work, we also consider the partial three-body constraint that enforces the nonnegativity of the three-body RDM, $\mathbf{T2}$,[44, 62] with elements

$$\begin{aligned} T2^{t_\sigma u_\tau v_\kappa}_{w_\lambda x_\mu y_\nu} \;&=\; \langle\Psi|\hat{a}^\dagger_{t_\sigma}\hat{a}^\dagger_{u_\tau}\hat{a}_{v_\kappa}\hat{a}^\dagger_{y_\nu}\hat{a}_{x_\mu}\hat{a}_{w_\lambda}|\Psi\rangle \\ &+\; \langle\Psi|\hat{a}^\dagger_{y_\nu}\hat{a}_{x_\mu}\hat{a}_{w_\lambda}\hat{a}^\dagger_{t_\sigma}\hat{a}^\dagger_{u_\tau}\hat{a}_{v_\kappa}|\Psi\rangle\,. \end{aligned} \tag{28}$$

For a non-relativistic Hamiltonian, we may exploit the spin-block structure of each of these RDMs; this structure is described in Refs. 48 and 51.

For a non-relativistic Hamiltonian, the 2RDM can also be constrained to satisfy ensemble spin-state conditions. For example, when Eqs. 19-21 are satisfied, we have

$\langle \hat{S}_z \rangle = \frac{1}{2}(N_\alpha - N_\beta)$. By considering the expectation value of $\hat{S}^2$, we arrive at the equality

$$\sum_{tu} {}^2D^{t_\alpha u_\beta}_{t_\alpha u_\beta} = \frac{1}{2}(N_\alpha + N_\beta) + \frac{1}{4}(N_\alpha - N_\beta)^2 - S(S+1), \quad (29)$$

where S represents the total spin angular momentum quantum number. Slightly stronger [63] spin constraints can be derived for the case that the state in question is the maximal spin projection, $|\Psi\rangle = |\Psi_{S,M_S=S}\rangle$, by considering action of the raising operator, $\hat{S}^+$, on the wavefunction

$$\hat{S}^+ |\Psi_{S,M_S=S}\rangle = 0. \quad (30)$$

Equation 30 implies two sets of constraints given by

$$\langle \Psi_{S,M_S=S} | \hat{a}_t^\dagger \hat{a}_u \hat{S}^+ | \Psi_{S,M_S=S} \rangle = 0 \quad \forall t,u, \quad (31)$$

and

$$\langle \Psi_{S,M_S=S} | \hat{S}^+ \hat{a}_t^\dagger \hat{a}_u | \Psi_{S,M_S=S} \rangle = 0 \quad \forall t,u \quad (32)$$

which are expressible in terms of the elements of the particle-hole RDM as

$$\sum_v {}^2G^{v_\beta v_\alpha}_{t_\beta u_\alpha} = 0 \quad \forall t,u \quad (33)$$

$$\sum_v {}^2G^{t_\beta u_\alpha}_{v_\beta v_\alpha} = 0 \quad \forall t,u \quad (34)$$

Optimizations performed under these maximal spin constraints yield essentially the same results as those performed by enforcing the Eq. 29 alone (for the maximal spin state). We include them nonetheless because we have found that their presence sometimes improves the convergence properties of the v2RDM-CASSCF optimizations on open-shell systems.

C. Semidefinite optimization

The minimization of Eq. 12 with respect to the elements of the active-space 2RDM, subject to the constraints outlined above, is a semidefinite optimization problem. The primal formulation of this problem is

$$\begin{aligned} \text{minimize} \quad & E_{\text{primal}} &&= \mathbf{c^T} \cdot \mathbf{x}, \\ \text{such that} \quad & \mathbf{Ax} &&= \mathbf{b}, \\ \text{and} \quad & M(\mathbf{x}) &&\succeq 0 \end{aligned} \quad (35)$$

where the vector $\mathbf{x}$ is the primal solution vector and the vector $\mathbf{c}$ contains the one- and two-electron integrals. The constraint matrix $\mathbf{A}$ and constraint vector $\mathbf{b}$ encode the N-representability conditions that $\mathbf{x}$ must satisfy. The mapping $M(\mathbf{x})$ maps the primal solution onto the set of positive semidefinite active-space RDMs

$$M(\mathbf{x}) = \begin{pmatrix} {}^1\mathbf{D} & 0 & 0 & 0 & 0 & 0 \\ 0 & {}^1\mathbf{Q} & 0 & 0 & 0 & 0 \\ 0 & 0 & {}^2\mathbf{D} & 0 & 0 & 0 \\ 0 & 0 & 0 & {}^2\mathbf{Q} & 0 & 0 \\ 0 & 0 & 0 & 0 & {}^2\mathbf{G} & 0 \\ 0 & 0 & 0 & 0 & 0 & \mathbf{T2} \end{pmatrix}. \quad (36)$$

The corresponding dual formulation of the problem is

$$\begin{aligned} \text{maximize} \quad & E_{\text{dual}} &&= \mathbf{b}^T \cdot \mathbf{y}, \\ \text{such that} \quad & \mathbf{z} &&= \mathbf{c} - \mathbf{A}^T\mathbf{y}, \\ \text{and} \quad & M(\mathbf{z}) &&\succeq 0, \end{aligned} \quad (37)$$

where the vectors $\mathbf{y}$ and $\mathbf{z}$ are the dual solution vectors.

The optimial RDMs are determined using a boundary-point semidefinite optimization algorithm.[64–66] This approach maximizes the augmented Lagrangian for the dual problem

$$\mathcal{L}_{\text{act}} = \mathbf{b}^T\mathbf{y} - \mathbf{x}^T(\mathbf{A}^T\mathbf{y} - \mathbf{c} + \mathbf{z}) - \frac{1}{2\mu}||\mathbf{A}^T\mathbf{y} - \mathbf{c} + \mathbf{z}||^2 \quad (38)$$

by the following two-step procedure:

1. Solve $\mathbf{A}\mathbf{A}^T\mathbf{y} = \mathbf{A}(\mathbf{c} - \mathbf{z}) + \mu(\mathbf{b} - \mathbf{A}\mathbf{x})$ for $\mathbf{y}$ by conjugate gradient methods.
2. Update $\mathbf{x}$ and $\mathbf{z}$ by separating $\mathbf{U} = M(\mu\mathbf{x} + \mathbf{A}^T\mathbf{y} - \mathbf{c})$ into its positive and negative components (by diagonalization). The updated primal and dual solutions $\mathbf{x}$ and $\mathbf{z}$ are given by $M(\mathbf{x}) = \mathbf{U}(+)/\mu$ and $M(\mathbf{z}) = -\mathbf{U}(-)$.

The penalty parameter μ is dynamically updated during the course of the v2RDM calculation.[66] The v2RDM optimization is considered converged when

$$||\mathbf{A}\mathbf{x} - \mathbf{b}|| < \epsilon_{\text{error}}, \quad (39)$$

$$||\mathbf{A}^T\mathbf{y} - \mathbf{c} + \mathbf{z}|| < \epsilon_{\text{error}}, \quad (40)$$

and

$$|E_{\text{primal}} - E_{\text{dual}}| < \epsilon_{\text{gap}}, \quad (41)$$

for given thresholds ϵ_{error} and ϵ_{gap}.

D. Orbital optimization

In v2RDM-CASSCF, the energy is minimized with respect to both the elements of the RDMs and the orbital parameters. We employ an algorithm in which the orbitals are optimized after a preselected number of v2RDM iterations (steps 1 and 2 in Sec. II C) or after the v2RDM optimization converges. Because the v2RDM-CASSCF energy is invariant to rotations among inactive, active, or external orbitals, the energy is optimized with

respect to rotations between inactive and active, inactive and virtual, and active and virtual orbitals. The optimization utilizes an exponential parameterization of the orbital transformation matrix $\mathbf{U} = e^{\mathbf{K}}$, where the skew-symmetric matrix $\mathbf{K}$ contains the nonredundant rotation parameters. The unique matrix elements of $\mathbf{K}$ can be organized into the vector $\boldsymbol{\kappa}$, and the energy expression, truncated at second order in $\boldsymbol{\kappa}$, is

$$E(\boldsymbol{\kappa}) = E(\mathbf{0}) + \boldsymbol{\kappa}^T \mathbf{g} + \frac{1}{2}\boldsymbol{\kappa}^T \mathbf{B} \boldsymbol{\kappa}. \tag{42}$$

The energy is minimized with respect to the orbital parameters using a quasi-Newton approach that only requires the computation of the orbital gradient ($\mathbf{g}$) and diagonal elements of the orbital Hessian ($\mathbf{B}$). For details of the orbital optimization procedure, the reader is referred to Ref. 51. We consider the orbitals to be converged when the norm of the orbital gradient falls below the threshold ϵ_{ograd} and the energy computed before and after the orbitals optimization step differs by less than ϵ_{oene}.

E. Analytic gradients

To facilitate the derivation of the analytic gradients, we define the Lagrangian

$$\mathcal{L} = E_{\text{core}} + \mathcal{L}_{\text{act}}, \tag{43}$$

which is stationary with respect to variations in the active-space 1-RDM and 2-RDM (the reader is referred to Ref. 52 for a discussion on the stationarity of $\mathcal{L}_{\text{act}}$). The gradient of the energy with respect to an arbitrary perturbation χ is

$$\begin{aligned} \frac{\mathrm{d}E}{\mathrm{d}\chi} = \frac{\partial \mathcal{L}}{\partial \chi} &= \sum_{pq} (T^{\chi}_{pq} + V^{\chi}_{pq}) \gamma_{pq} \\ &+ \sum_{pqrs} (pq|rs)^{\chi}_{\text{DF}} \Gamma_{pqrs} - \sum_{pq} X_{pq} S^{\chi}_{pq} \end{aligned} \tag{44}$$

where T^{χ}_{pq}, V^{χ}_{pq}, and S^{χ}_{pq} are the kinetic energy, electron-nucleus potential energy, and overlap derivative integrals, respectively. The term involving the electron repulsion derivative integrals, $(pq|rs)^{\chi}_{\text{DF}}$, is evaluated as[67]

$$\begin{aligned} \sum_{pqrs} (pq|rs)^{\chi}_{\text{DF}} \Gamma_{pqrs} &= 2 \sum_{pq} \sum_{P} \Gamma^{P}_{pq} (P|pq)^{\chi} \\ &- \sum_{PQ} \Gamma_{PQ} V^{\chi}_{PQ} \end{aligned} \tag{45}$$

where

$$\Gamma^{P}_{pq} = \sum_{rs} \sum_{Q} \Gamma_{pqrs} B^{Q}_{rs} V^{-1/2}_{QP}, \tag{46}$$

and

$$\Gamma_{PQ} = \sum_{pq} \sum_{R} \Gamma^{P}_{pq} \Gamma^{R}_{pq} V^{-1/2}_{RQ}. \tag{47}$$

Although we present the gradient expressions in the MO basis, in practice, the gradient is evaluated in the AO basis. As such, the 1RDM and 2RDM must be transformed to the AO basis before contraction with the derivative integrals. Within the DF approximation, only two- and three-index quantities enter Eq. 44, meaning that we avoid the cost associated with transforming the full 2RDM to the AO basis, as was done in our previous implementation. This restructuring of the algorithm results in tremendous computational savings for derivative computations on large systems.

The last term in Eq. 44 arises from the orbital response to the perturbation. It can be shown[68] that for a CASSCF wave function with an energy that is stationary with respect to rotations between all nonredundant orbital pairs, the orbital response depends only on the overlap derivative integrals and the orbital Lagrangian, $\mathbf{X}$, with matrix elements

$$X_{pq} = \sum_{r} (T_{pr} + V_{pr}) \gamma_{rq} + 2 \sum_{rst} (pr|st) \Gamma_{qrst} \tag{48}$$

III. COMPUTATIONAL DETAILS

All v2RDM-CASSCF and B3LYP calculations were carried out in development version of Q-Chem 5.1. For geometry optimizations, v2RDM-CASSCF calculations were considered converged when $\epsilon_{\text{error}} < 1.0 \times 10^{-6}$, $\epsilon_{\text{gap}} < 1.0 \times 10^{-4}$ E_{h}, $\epsilon_{\text{ograd}} < 1.0 \times 10^{-6}$ E_{h}, and $\epsilon_{\text{oene}} < 1.0 \times 10^{-10}$ E_{h}. Geometry optimizations were considered converged when the maximum gradient component reached 1.5×10^{-5} $E_{\text{h}} a_0^{-1}$ and either the maximum atomic displacement was less than 6.0×10^{-5} a_0 or the energy change of successive optimization cycles was less than 1.0×10^{-8} E_{h}. Harmonic vibrational frequencies were computed by finite differences of the analytic energy gradients using a 5-point stencil with a displacement of 0.005 Å, and the "sow/reap" mode in the Psi4 software package was used to generate symmetry-adapted displacements. For the frequency calculations, we tightened the convergence criteria to $\epsilon_{\text{error}} < 1.0 \times 10^{-8}$, $\epsilon_{\text{gap}} < 1.0 \times 10^{-8}$ E_{h}, $\epsilon_{\text{ograd}} < 1.0 \times 10^{-8}$ E_{h}, and $\epsilon_{\text{oene}} < 1.0 \times 10^{-11}$ E_{h}. However, we note that we encountered some difficulties in converging some PQG+T2 computations this tightly. In these cases (which are noted in Table V), the convergence criteria were loosened to $\epsilon_{\text{error}} < 1.0 \times 10^{-6}$, $\epsilon_{\text{gap}} < 1.0 \times 10^{-6}$ E_{h}, $\epsilon_{\text{ograd}} < 1.0 \times 10^{-6}$ E_{h}, and $\epsilon_{\text{oene}} < 1.0 \times 10^{-9}$ E_{h}. We used finite difference frequency calculations to estimate the error introduced by the loose convergence thresholds. Computations were performed at the PQG level of theory using both sets of thresholds, and we estimate this error to be less than cm^{-1}, except in the case of the low-frequency mode for HNC which exhibited larger errors (see Supporting Information).

All CI-CASSCF calculations were performed using the GAMESS software package.[69] The CI-CASSCF cal-

TABLE II: Term symbols and active spaces for the small molecules that comprise our test set.

Molecule	Term	Active Space
BF	$^1\Sigma^+$	(10,8)
BH	$^1\Sigma^+$	(4,5)
C_2	$^1\Sigma_g^+$	(8,8)
CH_2	$^1A_1$	(6,6)
CH_4	$^1A_1$	(8,8)
CO	$^1\Sigma^+$	(10,8)
F_2	$^1\Sigma_g^+$	(14,8)
H_2O	$^1A_1$	(8,6)
HCN	$^1\Sigma^+$	(10,9)
HF	$^1\Sigma^+$	(8,5)
HNC	$^1\Sigma^+$	(10,9)
HNO	$^1A'$	(12,9)
HOF	$^1A'$	(14,9)
N_2	$^1\Sigma_g^+$	(10,8)
N_2H_2	^1A_g	(12,10)
NH_3	$^1A_1$	(8,7)
BO	$^2\Sigma^+$	(9,8)
CH	$^2\Pi$	(5,5)
NH_2	$^2B_1$	(7,6)
OH	$^2\Pi$	(7,5)
B_2	$^3\Sigma_g^-$	(6,8)
CH_2	$^3B_1$	(6,6)
NF	$^3\Sigma^-$	(12,8)
NH	$^3\Sigma^-$	(6,5)
O_2	$^3\Sigma_g^-$	(12,8)

culations were considered converged when the maximum asymmetry in the Lagrangian matrix fell below 1.0×10^{-7} E_h and the energy change was smaller than 1.0×10^{-10} E_h. The CI-CASSCF geometry optimizations were considered converged when the largest component of the gradient was below 1.0×10^{-7} $E_\mathrm{h} a_0^{-1}$ and the root mean square gradient was less than $\frac{1}{3} \times 10^{-7}$ $E_\mathrm{h} a_0^{-1}$. Harmonic vibrational frequencies were computed with GAMESS using analytic hessians, which are available for basis sets comprised of s, p, and d functions. Therefore, we report harmonic frequencies for the cc-pVDZ basis set only.

All calcualtions employed the cc-pVXZ[70] (X = D, T, Q) basis sets. The cc-pVXZ-JK[71] auxiliary basis sets were used in the DF approximation for the v2RDM-CASSCF computations. The cc-pVDZ-JK basis set is formed by removing the highest angular momentum functions from the cc-pVTZ-JK basis set.

IV. RESULTS AND DISCUSSION

A. Benchmark computations: equilibrium geometries

We optimized the geometries for the 25 molecules listed in Table II using CI- and v2RDM-CASSCF with a full-valence active space. Table III presents the error in the CI- and v2RDM-CASSCF bond lengths relative to those derived from experiment. Agreement with experimental geometries generally improves with the size of the basis set for both CI- and v2RDM-CASSCF. For the cc-pVQZ basis set, the mean unsigned error for the bond lengths are 1.0 pm, 1.6 pm, and 1.1 pm for CI-CASSCF, PQG, and PQG+T2, respectively. The unsigned errors are under 2.0 pm for CI-CASSCF and PQG+T2 using the cc-pVQZ basis except for two cases (F_2 and B_2). In general, bond lengths obtained from PQG tend to deviate more from experiment than those from PQG+T2 or CI-CASSCF.

Table IV provides errors in the CI- and v2RDM-CASSCF bond angles relative to those derived from experiment. Again, in general, these errors decrease with the size of the basis set. For the cc-pVQZ basis set the errors are all below 5.0° with mean unsigned errors of 1.5°, 1.7°, and 1.5° for CI-CASSCF, PQG, and PQG+T2, respectively. For this test set, v2RDM- and CI-CASSCF provide predictions in bond angles that are generally similar in quality, when comparing to angles derived from experiment. For example, CI-CASSCF and PQG+T2 both underestimate all bond angles with the exception of the H–N–O angle in HNO. The H–N–N angle in N_2H_2 is also overestimated when using PQG within the cc-pVTZ and cc-pVQZ basis sets. Although the maximum error for each level of theory exceeds 4.0° (CH_2), all other bond angles agree with those from experiment to within 2.0°.

Figure 1 illustrates the difference between the CI- and v2RDM-CASSCF bond lengths in the cc-pVXZ basis sets (X = D, T, Q). In general, these differences are insensitive to the size of the one-electron basis. The mean unsigned differences between the CI-CASSCF and PQG bond lengths are 0.67 pm, 0.74 pm, and 0.62 pm for the cc-pVDZ, cc-pVTZ, and cc-pVQZ, respectively. The mean unsigned differences in these basis sets decrease to, at most, 0.06 pm when the T2 condition is enforced. Similarly, the mean unsigned difference between the CI- and PQG bond angles is 0.4° for all basis sets and falls to 0.0° when enforcing the PQG+T2 conditions. These results demonstrate that the PQG+T2 conditions lead to quantitative agreement between CI- and v2RDM-CASSCF geometries. We recently reported similar deviations between CI- and v2RDM-CASSCF bond lengths and angles for a test set of 20 molecules with singlet spin states using analytic energy gradients and conventional (non-DF) ERIs.[52] The present results extend these observations to the case of non-singlet molecules and to gradients computed within the DF approximation. As seen in Fig. 1 (and in Ref. 52) v2RDM-CASSCF bond lengths are typically longer than those from CI-CASSCF. This effect can be rationalized in terms of the "over correlation" problem of v2RDM methods; for small molecules, more approximate N-representability conditions lead to longer bond lengths.

We note two clear outliers in Fig. 1, which correspond to bond lengths for C_2 and B_2 optimized under the PQG conditions. The CI-CASSCF wave functions for these two molecules exhibit the most multconfigurational character in the entire set, as measured by the magnitude of the largest CI-coefficients in the respective expansions

TABLE III: Errors in computed equilibrium bond lengths (Δr_e, pm)[a] from CI- and v2RDM-CASSCF using the cc-pVXZ (X = D, T, Q) basis sets. Computed bond lengths are compared to those obtained from experiment (r_e, Å). All values of r_e were taken from Ref. 72 and the references therein.

				Δr_e								
				cc-pVDZ			cc-pVTZ			cc-pVQZ		
Molecule	Term	Bond	r_e	CI	PQG	PQG+T2	CI	PQG	PQG+T2	CI	PQG	PQG+T2
BF	$^1\Sigma^+$	B-F	1.267	2.4	2.5	2.5	0.1	0.1	0.1	−0.2	−0.2	−0.2
BH	$^1\Sigma^+$	H-B	1.232	3.5	4.1	3.5	1.9	2.5	1.9	1.7	2.3	1.7
C_2	$^1\Sigma_g^+$	C-C	1.242	2.4	7.1	2.8	1.3	5.8	1.7	1.1	5.5	1.5
CH_2	$^1A_1$	H-C	1.107	3.2	3.6	3.2	1.8	2.3	1.8	1.7	2.2	1.7
CH_4	$^1A_1$	H-C	1.087	2.5	3.2	2.5	1.4	2.2	1.5	1.4	2.2	1.4
CO	$^1\Sigma^+$	C-O	1.128	1.4	1.8	1.4	0.7	1.1	0.8	0.5	0.9	0.5
F_2	$^1\Sigma_g^+$	F-F	1.412	10.5	10.5	10.5	4.9	4.9	4.9	4.8	4.8	4.8
H_2O	$^1A_1$	H-O	0.958	1.3	1.4	1.3	0.6	0.7	0.6	0.5	0.6	0.5
HCN	$^1\Sigma^+$	H-C	1.064	2.4	3.0	2.4	−0.7	1.9	−0.7	−0.7	−0.6	−0.7
		C-N	1.156	1.9	2.8	2.0	0.4	1.7	0.5	0.3	0.8	0.3
HF	$^1\Sigma^+$	H-F	0.917	0.5	0.5	0.5	0.0	0.0	0.0	−0.2	−0.2	−0.2
HNC	$^1\Sigma^+$	H-N	0.986	2.5	3.3	2.5	1.6	2.4	1.7	1.6	2.4	1.6
		C-N	1.173	1.6	2.5	1.7	0.5	1.3	0.5	0.3	1.2	0.4
HNO	$^1A'$	H-N	1.090	−0.2	0.0	−0.2	−1.3	−1.1	−1.2	−1.4	−1.3	−1.3
		N-O	1.209	0.6	1.4	0.7	0.2	1.0	0.3	0.0	0.8	0.1
HOF	$^1A'$	H-O	0.960	1.9	2.2	2.0	1.2	1.4	1.2	1.0	1.3	1.1
		O-F	1.442	4.9	5.4	4.9	2.1	2.6	2.1	1.9	2.4	1.9
N_2	$^1\Sigma_g^+$	N-N	1.098	1.9	2.3	1.9	0.8	1.3	0.9	0.6	1.1	0.7
N_2H_2	^1A_g	H-N	1.028	2.5	3.3	2.6	1.5	2.3	1.6	1.4	2.2	1.4
		N-N	1.252	1.3	1.3	1.4	0.7	0.7	0.8	0.5	0.5	0.6
NH_3	$^1A_1$	H-N	1.012	2.2	2.5	2.2	1.1	1.5	1.1	0.9	1.3	1.0
BO	$^2\Sigma^+$	B-O	1.204	1.3	1.9	1.4	0.9	1.5	1.0	0.6	1.2	0.7
CH	$^2\Pi$	H-C	1.120	2.7	2.5	2.7	1.3	1.2	1.3	1.1	1.0	1.1
NH_2	$^2B_1$	H-N	1.024	2.3	2.6	2.3	1.3	1.6	1.3	1.2	1.4	1.2
OH	$^2\Pi$	H-O	0.970	1.3	1.3	1.3	0.5	0.5	0.5	0.3	0.3	0.3
B_2	$^3\Sigma_g^-$	B-B	1.590	3.9	8.2	4.3	2.7	7.0	3.1	2.4	6.7	2.9
CH_2	$^3B_1$	H-C	1.085	1.7	1.9	1.7	0.5	0.7	0.5	0.4	0.7	0.4
NF	$^3\Sigma^-$	N-F	1.317	1.7	1.8	1.7	0.9	1.0	0.9	0.8	0.9	0.8
NH	$^3\Sigma^-$	H-N	1.036	2.3	2.3	2.3	1.1	1.1	1.1	1.0	1.0	1.0
O_2	$^3\Sigma_g^-$	O-O	1.208	1.3	2.0	1.4	1.0	1.7	1.1	0.8	1.4	0.9
		MSE[b]	–	2.3	3.0	2.4	1.0	1.8	1.1	0.9	1.5	0.9
		MUE[c]	–	2.3	3.0	2.4	1.2	1.8	1.2	1.0	1.6	1.1
		Max[d]	–	10.5	10.5	10.5	4.9	7.0	4.9	4.8	6.7	4.8

[a] $\Delta r_e = r_e^{\mathrm{CASSCF}} - r_e$. [b] mean signed error. [c] mean unsigned error. [d] maximum unsigned error.

TABLE IV: Errors in computed equilibrium bond angles ($\Delta\theta_e$, degrees)[a] from CI- and v2RDM-CASSCF using the cc-pVXZ (X=D,T,Q) basis sets. Computed bond angles are compared to those obtained from experiment (θ_e, degrees). All values of θ_e were taken from Ref. 72 and the references therein.

				$\Delta\theta_e$								
				cc-pVDZ			cc-pVTZ			cc-pVQZ		
Molecule	Term	Bond	θ_e	CI	PQG	PQG+T2	CI	PQG	PQG+T2	CI	PQG	PQG+T2
CH_2	$^1A_1$	H-C-H	102.4	−2.4	−1.8	−2.4	−1.4	−1.0	−1.4	−1.2	−0.9	−1.2
H_2O	$^1A_1$	H-O-H	104.5	−3.3	−3.5	−3.3	−1.9	−2.1	−1.9	−1.6	−1.8	−1.6
HNO	$^1A'$	H-N-O	108.0	0.5	1.1	0.5	0.9	1.4	0.9	1.0	1.5	1.0
HOF	$^1A'$	H-O-F	97.2	−1.3	−1.6	−1.3	−0.2	−0.5	−0.2	−0.1	−0.4	−0.1
N_2H_2	^1A_g	H-N-N	106.3	−1.3	−0.1	−1.3	−0.6	0.5	−0.7	−0.5	0.7	−0.5
NH_3	$^1A_1$	H-N-H	106.7	−3.9	−3.6	−3.9	−2.1	−2.1	−2.1	−1.8	−1.7	−1.8
NH_2	$^2B_1$	H-N-H	103.4	−3.2	−3.1	−3.2	−1.9	−2.0	−1.9	−1.6	−1.7	−1.7
CH_2	$^3B_1$	H-C-H	135.5	−4.5	−4.9	−4.5	−4.2	−4.5	−4.2	−4.2	−4.5	−4.2
		MSE[b]	–	−2.4	−2.2	−2.4	−1.4	−1.3	−1.5	−1.2	−1.1	−1.3
		MUE[c]	–	2.5	2.5	2.5	1.7	1.8	1.7	1.5	1.7	1.5
		Max[d]	–	4.5	4.9	4.5	4.2	4.5	4.2	4.2	4.5	4.2

[a] $\Delta\theta_e = \theta_e^{\mathrm{CASSCF}} - \theta_e$. [b] mean signed error. [c] mean unsigned error. [d] maximum unsigned error.

(0.83 for C_2 and 0.88 for B_2). For all other molecules considered herein, the largest CI-coefficient is greater than 0.95, with the exception of CH_4, which has a leading CI-coefficient of 0.92. These outliers suggest that the PQG conditions are insufficient to correctly describe the static correlation effects in B_2 and C_2.

FIG. 1: Difference in equilibrium bond lengths (Δr_e, pm; $\Delta r_e = r_e^{v2RDM} - r_e^{CI}$) obtained from full-valence v2RDM- and CI-CASSCF using the (a) cc-pVDZ, (b) cc-pVTZ, and (c) cc-pVQZ basis sets. The bond lengths considered correspond to those that are provided in Table III.

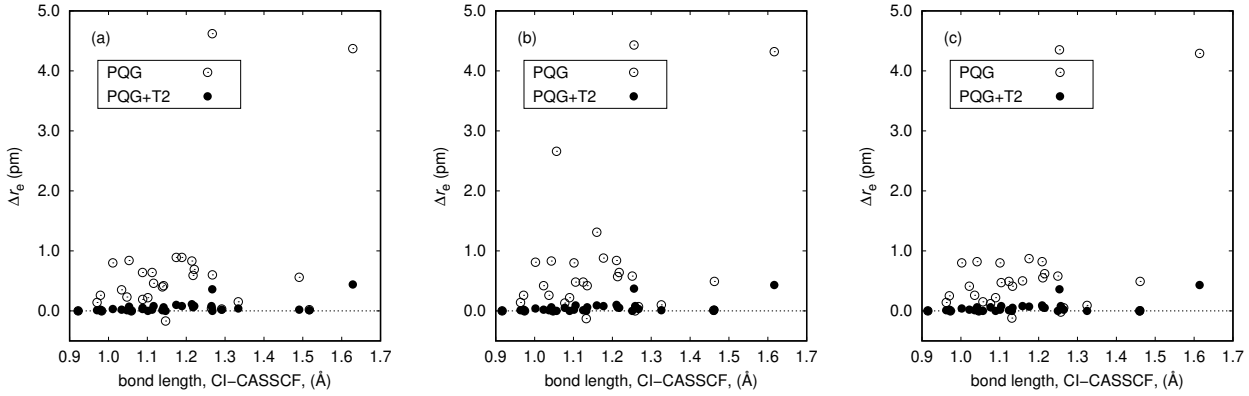

B. Benchmark computations: harmonic vibrational frequencies

In this section, we evaluate the quality of v2RDM-CASSCF harmonic vibrational frequencies computed from finite differences of analytic energy gradients. Table V presents the error in the harmonic frequencies obtained from CI- and v2RDM-CASSCF within the cc-pVDZ basis set, as compared to those derived from experiment. The mean unsigned errors are 64 cm^{-1}, 84 cm^{-1}, and 65 cm^{-1} at the CI-CASSCF, PQG, PQG+T2 levels of theory, respectively. The percent error is less than 9% for all CI-CASSCF frequencies, with the exception of four cases: (1) the Σ_g stretch of F_2 (-33%), (2) the $3A'$ bend of HOF (-16%), (3) the $2A_1$ wagging mode of NH_3 (29%), and (4) the $2A_1$ bend of triplet CH_2 (17%). The frequencies from PQG+T2 agree with those from CI-CASSCF for these four cases. For the remaining modes, the PQG+T2 frequencies similarly agree with those from experiment to within 9%. On the other hand, frequencies computed with the PQG conditions alone are less reliable; eight modes are predicted incorrectly by more than 10%, with the worst offender having a -51% error (the doubly-degenerate Π bend in HNC).

Figure 2 illustrates the difference between harmonic frequencies obtained from v2RDM-CASSCF (enforcing both the PQG and PQG+T2 conditions) and CI-CASSCF. It is clear that the consideration of the T2 condition dramatically improves the agreement between v2RDM- and CI-CASSCF. We find only two modes for which the PQG constraints alone provide better agreement with CI-CASSCF: (1) the $3A'$ bend of HNO and (2) the $3A_g$ mode of N_2H_2. However, we note that the discrepancies between CI-CASSCF and PQG+T2 frequencies are quite small in these cases (less than 10 cm^{-1}). For PQG, the percent difference in the predicted frequencies, relative to CI-CASSCF, is less than 4% in all but four cases: (1) the Σ_g stretch of C_2 (-19%), (2) the Π bend of HCN (-16%), (3) the Π bend of HNC (-51%), and (4) the Σ_g stretch B_2 (-14%). The agreement with CI-CASSCF is significantly improved upon considering the T2 condition, in which case the percent differences are less than 1% in all but two cases: (1) the Σ_g stretch of C_2 (-1%) and (2) the Σ_g stretch of B_2 (-2%). The mean unsigned differences between v2RDM- and CI-CASSCF frequencies are 44 cm^{-1} and 4 cm^{-1} when optimized RDMs satisfy the PQG and PQG+T2 constraints, respectively. In general, we note that the v2RDM-CASSCF frequencies are lower than those predicted by CI-CASSCF. Of the 52 frequencies considered, only five PQG and three PQG+T2 frequencies are significantly (more than 0.5 cm^{-1}) higher than the corresponding CI-CASSCF frequency. It appears that the over-correlation associated with approximate N-representability manifests itself in generally underestimated harmonic frequencies.

C. Linear acenes: equilibrium geometries and singlet-triplet gap

The linear polyacene series exhibits complex electronic structure, and an extensive literature considers the relative ordering of the lowest-energy singlet and triplet states, as well as the degree to which the singlet states of larger members of the series can be considered as having polyradical character. [48, 50, 51, 73–82] Here, we demonstrate the applicability of our v2RDM-CASSCF energy gradient implementation to large molecules with large active spaces by reporting equilibrium geometries and adiabatic singlet-triplet energy gaps for the linear polyacene series up to dodecacene. The active space is chosen to be comprised of the π-MO network, which, for an acene molecule consisting of k fused six-membered rings, corresponds to a $(4k+2, 4k+2)$ active space. For dodecacene, the active space consists of 50 electrons in 50 orbitals.

TABLE V: Errors in computed harmonic vibrational frequencies ($\Delta\omega_e$, cm^{-1})[a] computed using CI- and v2RDM-CASSCF for the cc-pVDZ basis set. Computed frequencies are compared to those obtained from experiment (ω_e, cm^{-1}). All values of ω_e were taken from Ref. 72 and the references therein.

					$\Delta\omega_e$		
Molecule	Term	Mode	Sym	ω_e	CI	PQG	PQG+T2
BF	$^1\Sigma^+$	1	Σ	1402	−67	−68	−68[b]
BH	$^1\Sigma^+$	1	Σ	2367	−100	−139	−99
C_2	$^1\Sigma_g^+$	1	Σ_g	1855	−5	−363	−31
CH_2	$^1A_1$	1	A_1	2806	−14	−45	−16
		2	A_1	1353	64	9	64
		3	B_2	2865	−11	−19	−12
CH_4	$^1A_1$	1	A_1	2917	22	−34	20[b]
		2	E	1534	22	−9	22[b]
		3	T_2	3019	49	66	48[b]
		4	T_2	1306	34	25	33[b]
CO	$^1\Sigma^+$	1	Σ	2170	−5	−43	−11
F_2	$^1\Sigma_g^+$	1	Σ_g	917	−304	−305	−304
H_2O	$^1A_1$	1	A_1	3657	65	42	62
		2	A_1	1595	121	114	121
		3	B_2	3756	78	55	79
HCN	$^1\Sigma^+$	1	Σ	3312	59	7	55[b]
		2	Σ	2089	6	−65	−4[b]
		3	Π	712	10	−107	7[b]
HF	$^1\Sigma^+$	1	Σ	4138	−83	−83	−83
HNC	$^1\Sigma^+$	1	Σ	3653	84	−14	79[b]
		2	Σ	2029	14	−59	6[b]
		3	Π	477	−1	−245	−5[b]
HNO	$^1A'$	1	A'	2684	−48	−26	−54
		2	A'	1565	36	15	29
		3	A'	1501	39	42	33
HOF	$^1A'$	1	A'	3537	125	88	121[b]
		2	A'	1393	−67	−80	−69[b]
		3	A'	886	−140	−150	−140[b]
N_2	$^1\Sigma_g^+$	1	Σ_g	2359	−4	−54	−15
N_2H_2	^1A_g	1	A_g	3058	37	−65	26[b]
		2	A_g	1583	37	30	35[b]
		3	A_g	1529	20	16	12[b]
		4	A_u	1289	27	−10	25[b]
		5	B_u	3120	3	−73	−5[b]
		6	B_u	1316	37	28	35[b]
NH_3	$^1A_1$	1	A_1	3337	−9	−52	−13
		2	A_1	950	279	257	280
		3	E	3444	8	−18	5
		4	E	1627	81	62	81
BO	$^2\Sigma^+$	1	Σ	1886	−14	−61	−19[b]
CH	$^2\Pi$	1	Σ	2859	−114	−83	−114[b]
NH_2	$^2B_1$	1	A_1	3219	−5	−30	−7[b]
		2	A_1	1497	76	68	76[b]
		3	B_2	3301	6	−19	5[b]
OH	$^2\Pi$	1	Σ	3738	−130	−130	−130
B_2	$^3\Sigma_g^-$	1	Σ_g	1051	−32	−173	−51
CH_2	$^3B_1$	1	A_1	2806	245	218	245[b]
		2	A_1	963	160	193	160[b]
		3	B_2	3190	71	42	70[b]
NF	$^3\Sigma^-$	1	Σ	1141	−65	−67	−66[b]
NH	$^3\Sigma^-$	1	Σ	3282	−171	−171	−171
O_2	$^3\Sigma_g^-$	1	Σ_g	1580	−51	−108	−62[b]
			MSE[c]	–	9	−31	6
			MUE[d]	–	64	84	65
			Max[e]	–	304	363	304

[a] $\Delta\omega_e = \omega_e^{\mathrm{CASSCF}} - \omega_e$. [b] "loose" convergence criteria used (Sec. III). [c] mean signed error. [d] mean unsigned error. [e] maximum unsigned error.

Figure 3 shows the adiabatic singlet-triplet excitation energies computed at the PQG/cc-pVDZ, DMRG-driven complete active space CI (CASCI)/DZ,[75] and quantum Monte Carlo (QMC) [82] levels of theory, along with vertical excitation energies derived from the particle-particle random phase approximation (PP-RPA, using the cc-pVDZ basis)[81] and experiment.[83–86] The QMC results taken from Ref. 82 were obtained using a Jastrow single determinant (JSD) wave function, optimized using lattice regularized diffusion Monte Carlo (LRDMC). PP-RPA, DMRG-CASCI, PQG, and experiment are all in reasonable agreement for the smaller members of

FIG. 2: Difference in equilibrium harmonic vibrational frequencies ($\Delta\omega_e = \omega_e^{v2RDM} - \omega_e^{CI}$) obtained from full-valence v2RDM- and CI-CASSCF using the cc-pVDZ basis sets. The cc-pVDZ-JK auxiliary basis set was used in the v2RDM-CASSCF optimizations. The frequencies considered correspond to those that are provided in Table V.

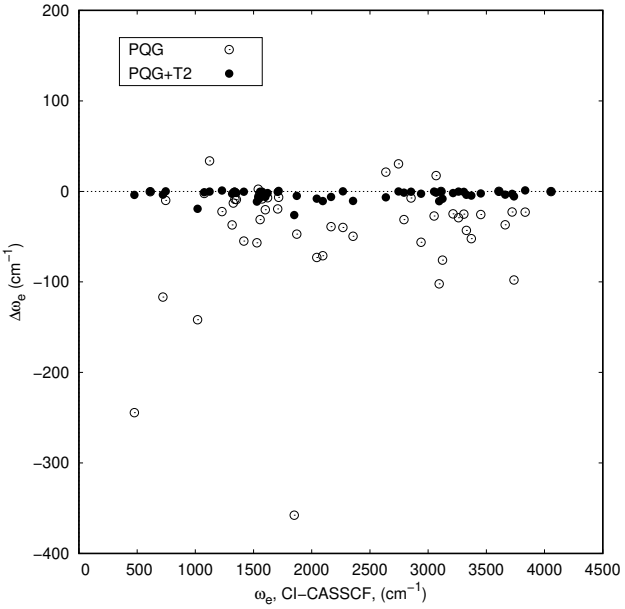

FIG. 3: Adiabatic singlet-triplet excitation energies for v2RDM-CASSCF PQG, DMRG-CASCI,[75] and JSD[82] along with vertical excitation energies using particle-particle random phase approximation[81] and experimental excitation energies.[83–86]

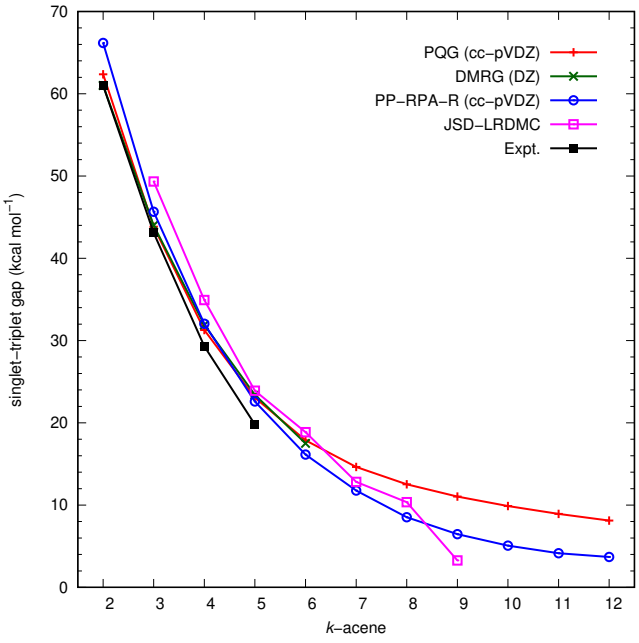

the series. Using the simple exponential decay formula $E = ae^{-n/b} + c$, the PQG estimate of the gap at the infinitely-long-molecule limit is 7.8 kcal mol^{-1}. This value is slightly larger than that recently estimated[81] using PP-RPA, but direct comparisons to this and other values is complicated for several reasons. First, the PP-RPA excitation energies presented in Ref. 81 are vertical; the singlet and triplet energies reproduced in Fig. 3 were evaluated at the singlet geometry, which was optimized using restricted B3LYP (hence, the "R" in PP-RPA-R). Second, comparisons to JSD are difficult because the JSD curve is far from smooth, and the second kink at nonacene can be attributed to the fact that this particular geometry was optimized at the JSD level of theory, while all of the other geometries were optimized using DFT (with the B3LYP functional).[82] Nonetheless, it does appear that the lack of dynamical correlation effects in our computations may lead to an overestimation of the singlet-triplet energy gap in the limit of infinitely long acene molecules.

Figure 4 shows the bond length alternation (BLA) for the C–C bonds along the long edge of each member of the linear polyacene series. The equilibrium cartesian coordinates are provided in the Supporting Information. In general, the alternation appears greatest toward the outer parts of the molecules, with smaller changes in the middle of the molecules; this trend applies to both the singlet and triplet states and is in agreement with previous work. For dodecacene, the C–C bond lengths lie within the range of 1.38 Å to 1.43 Å and approach a bond length of 1.41 Å in the center of the molecule. This bond equalization, which has been reported previously,[87, 88] is more noticeable in the geometry for the triplet state. Dupuis *et al.*[82] note that the equalization is associated with the localization of charge along the edges of the acene molecule, which, for the singlet state, is a signature of an antiferromagnetic arrangment of electrons that could be described as a di- or even polyradical. The central C–C bond length limit of 1.41 Å predicted by PQG is consistent with the limit of 1.406 Å separately reported using a spin-polarized DFT[87] and a DMRG valence bond model.[88]

For the smaller members of the series, the BLA pattern is qualitatively different for the singlet and triplet states, but, as the length of the molecules increases, the singlet and triplet BLA patterns become more similar. These results constrast with the JSD-derived geometry for nonacene presented in Ref. 82. For JSD, the BLA pattern for the singlet and triplet states of nonacene clearly differ, and large oscillations (on the order of 0.02 Å for the triplet) persist in the center of the molecule. Since the JSD wave function describes dynamical correlation effects not captured by v2RDM-CASSCF, it is tempting to attribute these differences to a lack of dynamical correlation in the present computations. However, we observe similar agreement between the BLA patterns of the singlet and triplet states as described by unrestricted B3LYP, which *only* captures dynamical corre-

FIG. 4: C–C bond lengths (Å) along the long edge of the linear polyacene molecules. Results are presented for the lowest-energy singlet and triplet states computed at the PQG/cc-pVDZ level of theory.

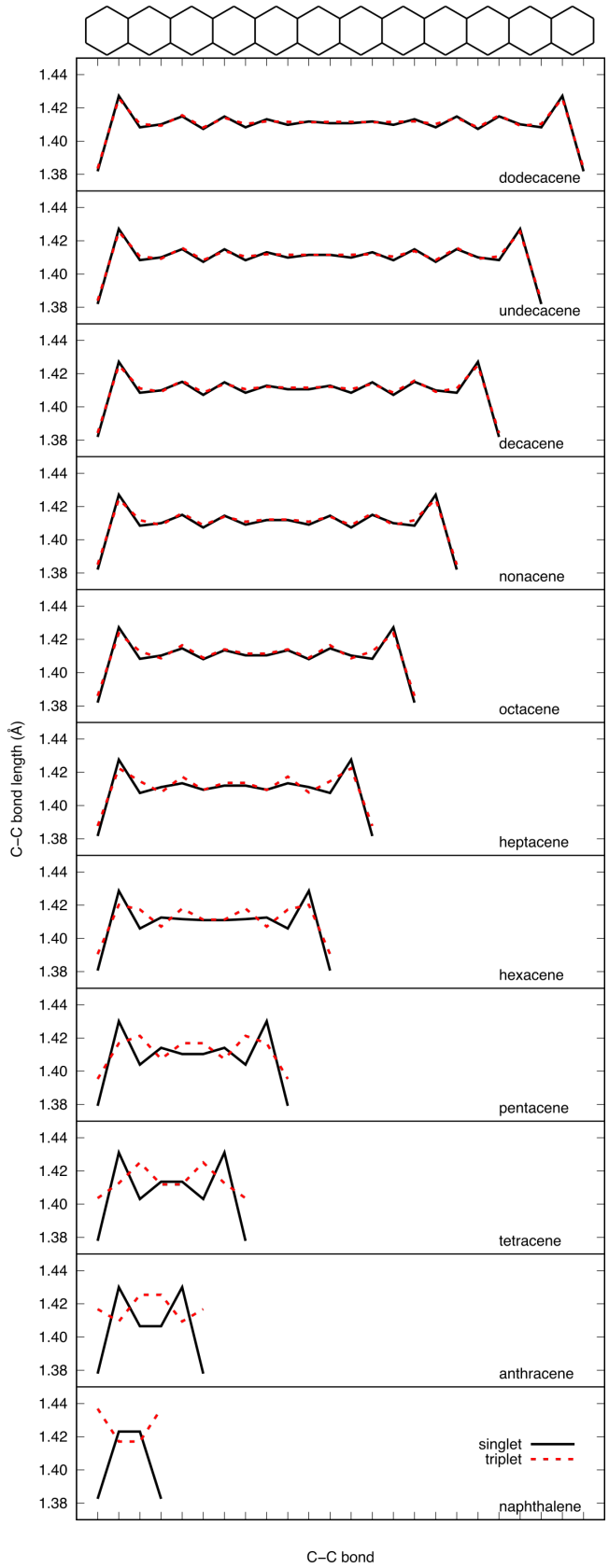

lation effects. Rather, the discrepancies between JSD and PQG can be traced to a lack of static correlation effects in the former method. This hypothesis is partially confirmed by the Jastrow double determinant (JDD) description of the geometry of the singlet state of nonacene, also provided in Ref. 82. JDD captures some static correlation effects that are missing in JSD, and differences between the predictions of JSD and JDD can be used to quantify whether or not the longer members of the acene series have open-shell singlet character. For the singlet state, JDD predicts that alternations in bond lengths are most apparent at the edge of the molecule, in agreement with the present PQG results. However, Ref. 82 also provides results using the Jastrow antisymmetric geminal power (JAGP) wave function that are more in line with those of JSD. The JAGP *ansatz* captures captures static correlation effects beyond those described by JDD, and, apparently, these additional considerations lead to a reduction in the open-shell character of the singlet state, as well as a commensurate reduction in the charge localization along the edges of the acene molecules. These observations, which are outlined in Ref. 82, are consistent with those of Ref. 89, which employed a coupled-cluster valence-bond singles and doubles (CCVB-SD) description of the valence space. At the CCVB-SD level of theory, the polyradical nature of the longer members of the linear polyacene series is significantly reduced when the σ-network is correlated alongside the π-network, as compared to the case where the π-network alone is correlated. Because our active space consists of only the π-network, signatures of polyradical character, such as the equalization of the BLA reported here and the natural orbital occupation numbers reported elsewhere,[48, 51] may be exaggerated.

We can further quantify the similarities between the singlet and triplet structures by comparing the root mean square (RMS) difference in the C–C bond lengths along the long edge of each linear acene molecule. Figure 5 illustrates this quantity using structures obtained at the PQG/cc-pVDZ and B3LYP/cc-pVDZ (restricted and unrestricted) levels of theory. The RMS difference in the bond lengths decreases monotonically for both restricted B3LYP and PQG, with the PQG value falling to less than 0.002 Å at dodecacene. On the other hand, from this metric, it appears that the singlet and triplet states of the longer members of the series are predicted to have quite different geometries at the restricted B3LYP level of theory. Indeed, when we look at the BLA patterns for restricted B3LYP, we find that this method recovers some of the characteristics of the nonacene geometry from JSD: (i) large changes in the bond lengths persist into the middle of the molecules, and (ii) the BLA patterns for the singlet and triplet states are qualitatively different. For molecules as large or larger than hexacene, spin-broken B3LYP solutions for the singlet states becomes energetically favorable, which leads to significant decreases in the RMS difference in the bond lengths.

FIG. 5: Root mean square (RMS) difference between the C–C bond lengths along the long edge of the linear polyacene molecules, as optimized for the lowest-energy singlet and triplet states.

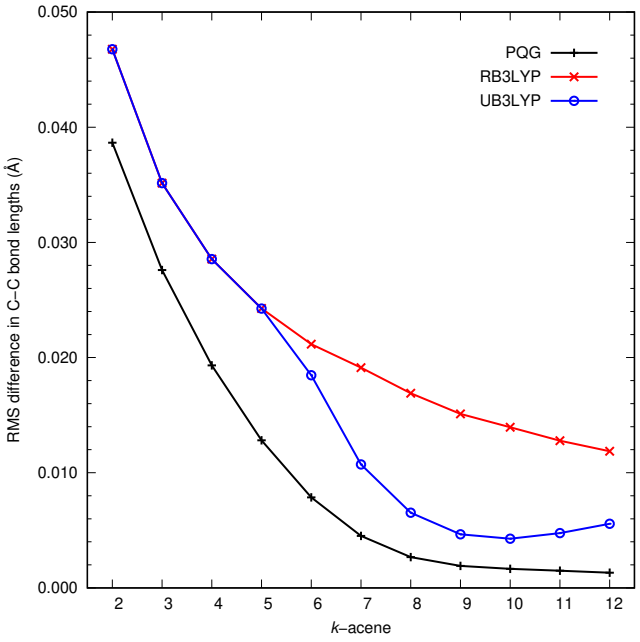

V. CONCLUSIONS

We have presented an implementation of analytic energy gradients for the v2RDM-driven CASSCF method using the density-fitting approximation to the electron repulsion integrals. Benchmark calculations for equilibrium geometries and harmonic vibrational frequencies indicate that v2RDM-CASSCF performs as well as CI-CASSCF in reproducing experimental results for a test set of small molecules. When the two-particle N-representability conditions are enforced, geometries and frequencies generally agree with those from CI-CASSCF, and significantly improved results are obtained when also enforcing three-particle N-representability conditions (T2). In the current implementation, enforcing the PQG and T2 conditions requires $\mathcal{O}(n^6)$ and $\mathcal{O}(n^9)$, floating-point operations, respectively, where n is the number of active space orbitals. For large-scale applications, the PQG conditions may be the only practically enforceable ones; fortunately, the present benchmark calculations indicate that these conditions should be adequate for equilibrium geometries. Some care should be taken, however, should one wish to compute harmonic frequencies under the PQG conditions alone.

The DF approximation facilitates the evaluation of v2RDM-CASSCF analytic energy gradients for large molecules with active spaces that are much larger than those that existing CI-CASSCF implementations can reasonably consider. We demonstrated this capability by optimizing the geometries for the lowest-energy singlet and triplet states of the linear polyacene series up to dodecacene. Using these optimized structures, we evaluated the adiabatic singlet-triplet energy gaps for the series and found that the v2RDM-CASSCF gap converges to 7.8 kcal mol^{-1} in the limit of an infinitely-long acene molecule; this estimate is larger than estimates from other methods that include dynamical correlation effects, such as the particle-particle random phase approximation. We also demonstrated that v2RDM-CASSCF predicts increasingly similar structures for the lowest-energy singlet and triplet states as the length of the acene molecules increases. This similarity is a signature of the open-shell nature of the singlet state. We caution, however, that several recent analyses[82, 89] suggest that the limited consideration of nondynamical correlation effects can lead to qualitatively different results than more rigorous considerations. In the present context, a more rigorous description of the system might include an expanded active space that incorporates some portion of the σ-network. Even then, a complete description of the system should include dynamical correlation effects beyond those inadvertently captured by large-active-space v2RDM-CASSCF.

Supporting information. Harmonic vibrational frequencies computed at the PQG/cc-pVDZ level of theory using "loose" and "tight" convergence criteria, equilibrium structures for the linear polyacene series computed at the PQG/cc-pVDZ level of theory, and C–C bond lengths for the long edge of the linear polyacene molecules up to dodecacene.

Acknowledgments. This material is based upon work supported by the Army Research Office Small Business Technology Transfer (STTR) program under Grant No. 65925CHST1.

[1] B. O. Roos and P. R. Taylor, Chem. Phys. **48**, 157 (1980).
[2] P. Siegbahn, A. Heiberg, B. Roos, and B. Levy, Phys. Scr. **21**, 323 (1980).
[3] P. E. M. Siegbahn, J. Almlöf, A. Heiberg, and B. O. Roos, J. Chem. Phys. **74**, 2384 (1981).
[4] B. O. Roos, *Advances in Chemical Physics; Ab Initio Methods in Quantum Chemistry Part 2* (John Wiley and Sons, Ltd., 1987), vol. 69, pp. 399–445.
[5] K. Andersson, P. A. Malmqvist, B. O. Roos, A. J. Sadlej, and K. Wolinski, J. Phys. Chem. **94**, 5483 (1990).

[6] K. D. Vogiatzis, D. Ma, J. Olsen, L. Gagliardi, and W. A. de Jong, J. Chem. Phys. **147**, 184111 (2017), URL https://doi.org/10.1063/1.4989858.
[7] J. Olsen and B. O. Roos, J. Chem. Phys. **89**, 2185 (1988).
[8] P. A. Malmqvist, A. Rendell, and B. O. Roos, J. Phys. Chem. **94**, 5477 (1990).
[9] T. Fleig, J. Olsen, and C. M. Marian, J. Chem. Phys. **114**, 4775 (2001).
[10] D. Ma, G. L. Manni, and L. Gagliardi, J. Chem. Phys. **135**, 044128 (2011).
[11] G. L. Manni, D. Ma, F. Aquilante, J. Olsen, and L. Gagliardi, J. Chem. Theory Comput. **9**, 3375 (2013).
[12] J. Ivanic, J. Chem. Phys. **119**, 9364 (2003).
[13] R. E. Thomas, Q. Sun, and G. H. Booth, J. Chem. Theory Comput. **11**, 5316 (2015).
[14] G. L. Manni, S. D. Smart, and A. Alavi, J. Chem. Theory Comput. **12**, 1245 (2016).
[15] S. R. White, Phys. Rev. Lett. **69**, 2863 (1992).
[16] S. R. White, Phys. Rev. B **48**, 10345 (1993).
[17] U. Schollwöck, Rev. Mod. Phys. **77**, 259 (2005).
[18] U. Schollwöck, Ann. Phys. **326**, 96 (2011).
[19] A. O. Mitrushenkov, R. Linguerri, and P. Palmieri, J. Chem. Phys. **119**, 4148 (2003).
[20] G. K.-L. Chan and M. Head-Gordon, J. Chem. Phys. **116**, 4462 (2002).
[21] K. H. Marti, I. M. Ondik, G. Moritz, and M. Reiher, J. Chem. Phys. **128**, 014104 (2008).
[22] D. Zgid and M. Nooijen, J. Chem. Phys. **128**, 014107 (2008).
[23] Y. Kurashige and T. Yanai, J. Chem. Phys. **130**, 234114 (2009).
[24] R. Olivares-Amaya, W. Hu, N. Nakatani, S. Sharma, J. Yang, and G. K.-L. Chan, J. Chem. Phys. **142**, 034102 (2015).
[25] S. Szalay, M. Pfeffer, V. Murg, G. Barcza, F. Verstraete, R. Schneider, and O. Legeza, Int. J. Quantum Chem. **115**, 1342 (2015).
[26] S. Wouters and D. V. Neck, Eur. Phys. J. D **68**, 272 (2014).
[27] S. Knecht, E. D. Hedegard, S. Keller, A. Kovyrshin, Y. Ma, A. Muolo, C. J. Stein, and M. Reiher, Chimia **70**, 244 (2016).
[28] D. Ghosh, J. Hachmann, T. Yanai, and G. K.-L. Chan, J. Chem. Phys. **128**, 144117 (2008).
[29] T. Yanai, Y. Kurashige, D. Ghosh, and G. K.-L. Chan, Int. J. Quantum Chem. **109**, 2178 (2009).
[30] T. Yanai, Y. Kurashige, E. Neuscamman, and G. K.-L. Chan, J. Chem. Phys. **132**, 024105 (2010).
[31] S. Wouters, W. Poelmans, P. W. Ayers, and D. V. Neck, Comput. Phys. Commun. **185**, 1501 (2014).
[32] Q. Sun, J. Yang, and G. K.-L. Chan, Chem. Phys. Lett. **683**, 291 (2017).
[33] Y. Ma, S. Knecht, S. Keller, and M. Reiher, J. Chem. Theory Comput. **13**, 2533 (2017).
[34] C. Garrod and J. K. Percus, J. Math. Phys. **5**, 1756 (1964).
[35] C. Garrod, M. V. Mihailović, and M. Rosina, J. Math. Phys. **16**, 868 (1975).
[36] M. V. Mihailović and M. Rosina, Nucl. Phys. A **237**, 221 (1975).
[37] M. Rosina and C. Garrod, J. Comp. Phys. **18**, 300 (1975).
[38] R. M. Erdahl, C. Garrod, B. Golli, and M. Rosina, J. Math. Phys. **20**, 1366 (1979).
[39] R. M. Erdahl, Rep. Math. Phys. **15**, 147 (1979).
[40] M. Nakata, H. Nakatsuji, M. Ehara, M. Fukuda, K. Nakata, and K. Fujisawa, J. Chem. Phys. **114**, 8282 (2001).
[41] D. A. Mazziotti and R. M. Erdahl, Phys. Rev. B **63**, 042113 (2001).
[42] D. A. Mazziotti, Phys. Rev. B **65**, 062511 (2002).
[43] D. A. Mazziotti, Phys. Rev. B **74**, 032501 (2006).
[44] Z. Zhao, B. J. Braams, M. Fukuda, M. L. Overton, and J. K. Percus, J. Chem. Phys. **120**, 2095 (2004).
[45] M. Fukuda, B. J. Braams, M. Nakata, M. L. Overton, J. K. Percus, M. Yamashita, and Z. Zhao, Math. Program., Ser. B **109**, 553 (2007).
[46] E. Cancès, G. Stoltz, and M. Lewin, J. Chem. Phys. **125**, 064101 (2006).
[47] B. Verstichel, H. V. Aggelen, D. V. Neck, P. W. Ayers, and P. Bultinck, Phys. Rev. B **80**, 032508 (2009).
[48] J. Fosso-Tande, D. R. Nascimento, and A. E. DePrince, Mol. Phys. **114**, 423 (2016).
[49] B. Verstichel, H. van Aggelen, D. V. Neck, P. Bultinck, and S. D. Baerdemacker, Comput. Phys. Commun. **182**, 1235 (2011).
[50] G. Gidofalvi and D. A. Mazziotti, J. Chem. Phys. **129**, 134108 (2008).
[51] J. Fosso-Tande, T.-S. Nguyen, G. Gidofalvi, and A. E. DePrince, J. Chem. Theory Comput. **12**, 2260 (2016).
[52] E. Maradzike, G. Gidofalvi, J. M. Turney, H. F. Schaefer, and A. E. DePrince, J. Chem. Theory Comput. **13**, 4113 (2017).
[53] https://github.com/edeprince3/v2rdm_casscf.
[54] J. M. Turney, A. C. Simmonett, R. M. Parrish, E. G. Hohenstein, F. A. Evangelista, J. T. Fermann, B. J. Mintz, L. A. Burns, J. J. Wilke, M. L. Abrams, et al., WIREs Comput. Mol. Sci. **2**, 556 (2012).
[55] R. M. Parrish, L. A. Burns, D. G. A. Smith, A. C. Simmonett, A. E. DePrince, E. G. Hohenstein, U. Bozkaya, A. Y. Sokolov, R. D. Remigio, R. M. Richard, et al., J. Chem. Theory Comput. **13**, 3185 (2017).
[56] J. L. Whitten, J. Chem. Phys. **58**, 4496 (1973).
[57] B. I. Dunlap, J. W. D. Connolly, and J. R. Sabin, J. Chem. Phys. **71**, 3396 (1979).
[58] M. Feyereisen, G. Fitzgerald, and A. Komornicki, Chem. Phys. Lett. **208**, 359 (1993).
[59] O. Vahtras, J. Almlöf, and M. W. Feyereisen, Chem. Phys. Lett. **213**, 514 (1993).
[60] Y. Shao, Z. Gan, E. Epifanovsky, A. T. Gilbert, M. Wormit, J. Kussmann, A. W. Lange, A. Behn, J. Deng, X. Feng, et al., Mol. Phys. **113**, 184 (2015), URL https://doi.org/10.1080/00268976.2014.952696.
[61] A. J. Coleman, Rev. Mod. Phys. **35**, 668 (1963).
[62] R. M. Erdahl, Int. J. Quantum Chem. **13**, 697 (1978).
[63] H. van Aggelen, B. Verstichel, P. Bultinck, D. V. Neck, and P. W. Ayers, J. Chem. Phys. **136**, 014110 (2012).
[64] J. Povh, F. Rendl, and A. Wiegele, Computing **78**, 277 (2006).
[65] J. Malick, J. Povh, F. Rendl, and A. Wiegele, SIAM J. Optim. **20**, 336 (2009).
[66] D. A. Mazziotti, Phys. Rev. Lett. **106**, 083001 (2011).
[67] F. Weigend and M. Häser, Theor. Chem. Acc. **97**, 331 (1997).
[68] J. E. Rice, R. D. Amos, N. C. Handy, T. J. Lee, and H. F. S. III, J. Chem. Phys. **85**, 963 (1986).
[69] M. W. Schmidt, K. K. Baldridge, J. A. Boatz, S. T. Elbert, M. S. Gordon, J. H. Jensen, S. Koseki, N. Matsunaga, K. A. Nguyen, S. Su, et al., J. Comput. Chem.

14, 1347 (1993).
[70] T. H. Dunning, J. Chem. Phys. **90**, 1007 (1989).
[71] F. Weigend, Phys. Chem. Chem. Phys. **4**, 4285 (2002).
[72] R. D. Johnson III, *Nist computational chemistry comparison and benchmark database*, release 16a, August 2013.
[73] K. N. Houk, P. S. Lee, and M. Nendel, J. Org. Chem. **66**, 5517 (2001).
[74] M. Bendikov, H. M. Duong, K. Starkey, K. N. Houk, E. A. Carter, and F. Wudl, J. Am. Chem. Soc. **126**, 7416 (2004).
[75] J. Hachmann, J. J. Dorando, M. Avilés, and G. K.-L. Chan, J. Chem. Phys. **127**, 134309 (2007).
[76] K. Pelzer, L. Greenman, G. Gidofalvi, and D. A. Mazziotti, J. Phys. Chem. A **115**, 5632 (2011).
[77] W. Mizukami, Y. Kurashige, and T. Yanai, J. Chem. Theory Comput. **9**, 401 (2013).
[78] F. Plasser, H. Pašalić, M. H. Gerzabek, F. Libisch, R. Reiter, J. Burgdörfer, T. Müller, R. Shepard, and H. Lischka, Angew. Chem. Int. Ed. **52**, 2581 (2013).
[79] S. Horn, F. Plasser, T. Müller, F. Libisch, J. Burgdörfer, and H. Lischka, Theor. Chem. Acc. **133**, 1511 (2014).
[80] S. Horn and H. Lischka, J. Chem. Phys. **142**, 054302 (2015).
[81] Y. Yang, E. R. Davidson, and W. Yang, Proc. Natl. Acad. Sci. U. S. A **113**, E5098 (2016).
[82] N. Dupuy and M. Casula, J. Chem. Phys. **148**, 134112 (2018).
[83] J. B. Birks, Photophysics of Aromatic Molecules Wiley, London, (1970).
[84] J. Burgos, M. Pope, C. E. Swenberg, and R. R. Alfano, Phys. Status Solidi B **83**, 249 (1977).
[85] N. Sabbatini, M. T. Indelli, M. T. Gandolfi, and V. Balzani, J. Phys. Chem. **86**, 3585 (1982).
[86] J. Schiedt and R. Weinkauf, Chem. Phys. Lett. **266**, 201 (1997).
[87] D. Jiang and S. Dai, J. Phys. Chem. A **112**, 332 (2008).
[88] Z. Qu, D. Zhang, C. Liu, and Y. Jiang, J. Phys. Chem. A **113**, 7909 (2009).
[89] J. Lee, D. W. Small, E. Epifanovsky, and M. Head-Gordon, J. Chem. Theory Comput. **13**, 602 (2017), URL `https://doi.org/10.1021/acs.jctc.6b01092`.

Combining pair-density functional theory and variational two-electron reduced-density matrix methods

Mohammad Mostafanejad[1] and A. Eugene DePrince III[1]

[1] *Department of Chemistry and Biochemistry, Florida State University, Tallahassee, FL 32306-4390*

Complete active space self-consistent field (CASSCF) computations can be realized at polynomial cost via the variational optimization of the active-space two-electron reduced-density matrix (2-RDM). Like conventional approaches to CASSCF, variational 2-RDM (v2RDM)-driven CASSCF captures nondynamical electron correlation in the active space, but it lacks a description of the remaining dynamical correlation effects. Such effects can be modeled through a combination of v2RDM-CASSCF and on-top pair-density functional theory (PDFT). The resulting v2RDM-CASSCF-PDFT approach provides a computationally inexpensive framework for describing both static and dynamical correlation effects in multiconfigurational and strongly correlated systems. On-top pair-density functionals can be derived from familiar Kohn-Sham exchange-correlation (XC) density functionals through the translation of the v2RDM-CASSCF reference densities [Li Manni *et al.*, J. Chem. Theory Comput. **10**, 3669-3680 (2014)]. Translated and fully-translated on-top PDFT versions of several common XC functionals are applied to the potential energy curves of N_2, H_2O, and CN^-, as well as to the singlet/triplet energy splittings in the linear polyacene series. Using v2RDM-CASSCF-PDFT and the translated PBE functional, the singlet/triplet energy splitting of an infinitely-long acene molecule is estimated to be 4.87 kcal mol^{-1}.

I. INTRODUCTION

The accurate and computationally affordable description of the electronic structure of many-body systems remains a major challenge within the quantum chemistry and molecular physics communities.[1–3] Specifically, the realization of general approaches that account for both dynamical and nondynamical correlation effects in multiconfigurational [4] or strongly-correlated systems is particularly difficult. The main issue is that many approaches designed to deal with the multireference (MR) problem are not particularly efficient for capturing dynamical correlation effects. A similar statement can be made regarding the ability of methods designed to model dynamical correlation to capture MR effects.

One can broadly classify approaches to the electron correlation problem as either falling within wave function theory (WFT), in which the many-electron wave function is obviously the central quantity, [5–7] or density-based theories, which include both density functional theory (DFT) [8–12] and reduced-density matrix (RDM)-based approaches. [13–17] In principle, WFT is preferable, as it allows for systematic improvement in the calculated energies and properties of the system.[18] In practice, however, the computational complexity of post-Hartree-Fock wave-function-based methods, specifically MR approaches, limits their application to small systems.[19] The wide-ranging success of DFT, on the other hand, stems from the its ability to provide a reasonable description of electron correlation at significantly lower costs. Nonetheless, DFT often fails for MR systems, and it does not offer a systematic approach for improving its accuracy. [8–12]

Within WFT, one of the most familiar approaches to the MR problem is the complete active space self-consistent field (CASSCF) method [20–23]. In CASSCF, the molecular orbitals are partitioned into inactive (doubly occupied), active (partially occupied), and external (empty) orbitals, and the active space is chosen with some knowledge as to which orbitals are important for the chemical problem at hand. In the canonical form of CASSCF, the active-space electronic structure is described by a full configuration interaction (CI) wave function, and it is assumed that all nondynamical correlation effects are captured by this procedure. Dynamical correlation effects can then be incorporated through a variety of approaches, including perturbation theory (using, for example, complete active space second-order perturbation theory (CASPT2) [24, 25]). CASPT2 requires knowledge of the four-electron reduced-density matrix (4-RDM), or some approximation to it, which can become problematic as the size of the active space increases. Accordingly, several approaches have been proposed that eliminate the manipulation of the 4-RDM, including the anti-Hermitian contracted Schrödinger equation (ACSE) [26–28] and the driven similarity renormalization group (DSRG) [29]. Both of these approaches require knowledge of the three-electron reduced-density matrix (3-RDM) or some approximation to it.

A long sought-after alternative to the methods described above involves the combination of the MR approach to the static correlation problem with a DFT-based description of dynamical correlation. Since the advent of the MR+DFT framework, [30, 31] a substantial amount of effort has been devoted to increasing the accuracy and efficiency of this approach. [32–50] There are several issues that one must carefully consider when developing a MR+DFT scheme, including (i) the symmetry dilemma that plagues Kohn-Sham (KS)-DFT in general, (ii) the double counting of electron correlation within the active space, and (iii) the steep computational scaling of many commonly used MR methods. The framework of the multiconfiguration pair-density func-

tional theory (MCPDFT) [51, 52] addresses the first two issues while leaving open the question of the cost of the evaluation of the underlying MR wave function. The success of the original formulation of MCPDFT[52] notwithstanding, Garza *et al.*[32] rightly note that, if the MR component is determined using an approach such as CASSCF, its utility is potentially limited by the exponential complexity of the CI-based active-space wave function. Hence, those authors propose that the static correlation within MCPDFT be described by the pair coupled-cluster doubles (pCCD) method, the scaling of which increases only polynomially with system size. More recently, the MCPDFT scheme has also been employed in conjunction with other active-space-based methods that scale more favorably than CASSCF, including the density matrix renormalization group (DMRG)[53] and the generalized active-space self-consistent field (GASSCF)[54].

Here, we offer an alternative strategy to overcome the problematic scaling of CI-based CASSCF within the MCPDFT framework. We elect to maintain the CASSCF-based description of the static correlation problem utilized in the original formulation of the approach,[52] but we represent the electronic structure of the active space with the two-electron reduced-density matrix (2-RDM), as opposed to the CI wave function. The computational complexity of variational 2-RDM-driven CASSCF (v2RDM-CASSCF) [55, 56] increases only polynomially with the size of the active space, thereby facilitating v2RDM-based MCPDFT computations (denoted v2RDM-CASSCF-PDFT) on active spaces as large as 50 electrons in 50 orbitals.

This paper is organized as follows. Section II provides an overview of v2RDM-CASSCF-PDFT, including brief discussions of the theory underlying the v2RDM-CASSCF and MCPDFT schemes. The computational details of the work are then given in Sec. III. In Sec. IV, we apply v2RDM-CASSCF-PDFT to the potential energy curves (PECs) of N_2, H_2O, and CN^-, as well as to the singlet/triplet energy gaps of the linear polyacene series. Some concluding remarks can be found in Sec. V.

II. THEORY

Throughout this work, we adopt the conventional notation employed within MR methods for labeling molecular orbitals (MOs, $\{\psi\}$): the indices i, j, k, and l represent inactive orbitals; t, u, v, and w indicate active orbitals; a, b, c, and d denote external orbitals; and p, q, r, and s represent general orbitals.

Let Ψ be an N-electron wave function in Fock space. One- and two- particle excitation operators can be expressed as [57]

$$\hat{E}^p_q = \hat{a}^\dagger_{p_\sigma}\hat{a}_{q_\sigma} \tag{1a}$$

$$\hat{e}^{pr}_{qs} = \hat{E}^p_q\hat{E}^r_s - \delta^q_r\hat{E}^p_s = \hat{a}^\dagger_{p_\sigma}\hat{a}^\dagger_{r_\tau}\hat{a}_{s_\tau}\hat{a}_{q_\sigma} \tag{1b}$$

where $\hat{a}^\dagger$ and $\hat{a}$ represent second-quantized creation and annihilation operators, respectively, and the Greek labels run over α and β spins. Einstein's summation convention is implied throughout. The non-relativistic Born-Oppenheimer (BO) electronic Hamiltonian is

$$\hat{\mathscr{H}} = h^p_q\hat{E}^p_q + \frac{1}{2}\nu^{pq}_{rs}\hat{e}^{pq}_{rs} \tag{2}$$

where $h^p_q = \langle\psi_p|\hat{h}|\psi_q\rangle$ is the sum of the electron kinetic energy and electron-nucleus potential energy integrals, and $\nu^{pq}_{rs} = \langle\psi_p\psi_q|\psi_r\psi_s\rangle$ represents the two-electron repulsion integral tensor. Because the electronic Hamiltonian includes up to only pair-wise interactions, the ground-state energy of a many-electron system can be expressed as an exact linear functional of the 2-RDM and the one-electron reduced-density matrix (1-RDM) [58–60]

$$E = {}^1D^p_q h^p_q + \frac{1}{2}{}^2D^{pq}_{rs}\nu^{pq}_{rs}. \tag{3}$$

Here, the 1-RDM and the 2-RDM are represented in their spin-free forms, defined as

$${}^1D^p_q = {}^1D^{p_\sigma}_{q_\sigma} = \langle\Psi|\hat{E}^p_q|\Psi\rangle \tag{4}$$

and

$${}^2D^{pq}_{rs} = {}^2D^{p_\sigma q_\tau}_{r_\sigma s_\tau} = \langle\Psi|\hat{e}^{pq}_{rs}|\Psi\rangle\,. \tag{5}$$

Summation over the spin labels is implied.

A. v2RDM-driven CASSCF

The CASSCF non-relativistic BO electronic Hamiltonian is

$$\hat{\mathscr{H}}_{\text{CASSCF}} = (h^t_u + 2\nu^{ti}_{ui} - \nu^{tu}_{ii})\hat{E}^t_u + \frac{1}{2}\nu^{tu}_{vw}\hat{e}^{tu}_{vw}, \tag{6}$$

and the CASSCF energy is expressible in terms of the active-space 1- and 2-RDMs

$$E_{\text{CASSCF}} = (h^t_u + 2\nu^{ti}_{ui} - \nu^{tu}_{ii})^1D^t_u + \frac{1}{2}\nu^{tv}_{uw}{}^2D^{tv}_{uw}. \tag{7}$$

The central idea of v2RDM-CASSCF is that the spin blocks of the active-space RDMs can be determined directly by minimizing the energy with respect to variations in their elements (and to variations in the orbital parameters).[55, 56] Because not every 2-RDM can be derived from an N-electron wave function, this procedure can lead to unphysically low energies;[13] a physically meaningful 2-RDM should fulfill certain N-representability conditions. These conditions are most easily expressed in terms of the individual spin blocks that contribute to the spin-free 2-RDM. Specifically, each spin block of the 2-RDM should (i) be Hermitian, (ii) be antisymmetric with respect to the permutation of particle labels, (iii) conserve the number of pairs of particles

(have a fixed trace), and (iv) contract to the appropriate spin block(s) of the 1-RDM. Constraints on the expectation value of $\hat{S}^2$ can also be applied.[61]

In addition to these trivial constraints on the 2-RDM, all spin blocks of all RDMs should be positive semidefinite. Such positivity conditions applied to the spin blocks of the 2-RDM, the two-hole RDM, and the particle-hole RDM constitute the two-body (PQG) constraints of Garrod and Percus.[62] Additional positivity conditions can be applied to higher-order RDMs. In this work, we consider the PQG constraints as well as the T2 partial three-particle conditions.[63, 64] The spin blocks of each of these RDMs are interrelated through linear mappings implied by the anticommutation properties of the creation and annihilation operators that define them. The v2RDM-CASSCF procedure thus involves a large-scale semidefinite optimization that we carry out using a boundary-point algorithm [65–67], the specific details of which can be found in Ref. 56.

B. Multi-configuration Pair-Density Functional Theory

One of the main pitfalls of the MR+DFT scheme is the double counting of electron correlation within the active space. The most expedient solution is to employ a small active space or modified functionals;[30, 31, 33] however, such strategies may not always lead to satisfactory results. A seemingly robust solution[52] partitions the interelectronic Coulomb contribution to the energy into a classical Coulomb component (obtained from a MR method) and all other exchange and pure two-electron contributions (described by DFT). Because the two-electron correlations are modeled entirely within the framework of DFT, double counting of such contributions to the energy is automatically avoided.

A second complication in MR+DFT is related to the "symmetry dilemma" [68] of standard KS-DFT. One manifestion of this issue within MR+DFT is the incompatibility of standard XC functionals with MR-method-derived spin densities for low-spin (i.e. $|M_S| < S$) states. Fortunately, this difficulty is easily overcome by replacing the usual independent variables that enter KS-DFT XC functionals, the total density, $\rho(\mathbf{r}) = \rho_\alpha(\mathbf{r}) + \rho_\beta(\mathbf{r})$, and the spin magnetization, $m(\mathbf{r}) = \rho_\alpha(\mathbf{r}) - \rho_\beta(\mathbf{r})$, with the total density and the on-top pair-density (OTPD), $\Pi(\mathbf{r})$.[35, 68, 69]

Both double counting and the symmetry dilemma are addressed through the framework of MCPDFT,[52] in which the total energy is defined as

$$E_{\mathrm{MCPDFT}} = (h^t_u + 2\nu^{ti}_{ui})^1 D^t_u + \frac{1}{2}\nu^{tv}_{uw}\,{}^1D^t_u\,{}^1D^v_w + E_{\mathrm{OTPD}}\left[\rho(\mathbf{r}), \Pi(\mathbf{r}), |\nabla\rho(\mathbf{r})|, |\nabla\Pi(\mathbf{r})|\right]. \quad (8)$$

Here, the two-electron term from Eq. 7 has been replaced by a classical Coulombic term, and the remaining exchange and correlation effects are folded into a functional of the OTPD. The total electronic density and its gradient are defined by the 1-RDM as

$$\rho(\mathbf{r}) = {}^1D^p_q\ \psi^*_p(\mathbf{r})\psi_q(\mathbf{r}), \quad (9)$$

and

$$\nabla\rho(\mathbf{r}) = {}^1D^p_q\left[\nabla\psi^*_p(\mathbf{r})\psi_q(\mathbf{r}) + \psi^*_p(\mathbf{r})\nabla\psi_q(\mathbf{r})\right], \quad (10)$$

respectively. The 1-RDM is obtained from a MR computation. The OTPD and its gradient can similarly be defined in terms of the 2-RDM as

$$\Pi(\mathbf{r}) = {}^2D^{pq}_{rs}\ \psi^*_p(\mathbf{r})\psi^*_q(\mathbf{r})\psi_r(\mathbf{r})\psi_s(\mathbf{r}), \quad (11)$$

and

$$\begin{aligned}\nabla\Pi(\mathbf{r}) = {}^2D^{pq}_{rs}\ \Big[\ & \nabla\psi^*_p(\mathbf{r})\psi^*_q(\mathbf{r})\psi_r(\mathbf{r})\psi_s(\mathbf{r}) \\ +\ & \psi^*_p(\mathbf{r})\nabla\psi^*_q(\mathbf{r})\psi_r(\mathbf{r})\psi_s(\mathbf{r}) \\ +\ & \psi^*_p(\mathbf{r})\psi^*_q(\mathbf{r})\nabla\psi_r(\mathbf{r})\psi_s(\mathbf{r}) \\ +\ & \psi^*_p(\mathbf{r})\psi^*_q(\mathbf{r})\psi_r(\mathbf{r})\nabla\psi_s(\mathbf{r})\ \Big], \end{aligned} \quad (12)$$

respectively. The 2-RDM, like the 1-RDM, is obtained from a MR computation.

Armed with a potentially robust framework for MR+DFT, we must identify a suitable OTPD functional for use within MCPDFT. The simplest class of functionals can be derived from existing approximate XC functionals employed within KS-DFT by first recognizing that, for a density derived from a single Slater determinant, the spin magnetization can be expressed exactly in terms of the OTPD and the total density.[35, 69] More specifically, the spin polarization factor, $\zeta(\mathbf{r}) = m(\mathbf{r})/\rho(\mathbf{r})$, can be expressed as

$$\zeta(\mathbf{r}) = \sqrt{1 - R(\mathbf{r})}, \quad (13)$$

where

$$R(\mathbf{r}) = \frac{4\,\Pi(\mathbf{r})}{\rho^2(\mathbf{r})}. \quad (14)$$

The basic assumption underlying the "translated" (t) OTPD functionals proposed in Ref. 52 is that the spin polarization factor can be similarly defined for a density and OTPD obtained from a MR method, as

$$\zeta_{\mathrm{tr}}(\mathbf{r}) = = \begin{cases} \sqrt{1 - R(\mathbf{r})} & R(\mathbf{r}) \le 1 \\ 0 & R(\mathbf{r}) > 1 \end{cases} \quad (15)$$

where the second case accounts for the fact that the argument of the square root can become negative for $\rho(\mathbf{r})$ and $\Pi(\mathbf{r})$ that are not derived from a single-configuration wave function. The translated OTPD functional is then defined as

$$E_{\mathrm{OTPD}}\left[\rho(\mathbf{r}), \Pi(\mathbf{r}), |\nabla\rho(\mathbf{r})|\right] \equiv E_{\mathrm{XC}}[\tilde{\rho}_\alpha(\mathbf{r}), \tilde{\rho}_\beta(\mathbf{r}), |\nabla\tilde{\rho}_\alpha(\mathbf{r})|, |\nabla\tilde{\rho}_\beta(\mathbf{r})|], \quad (16)$$

where the tilde refers to translated densities and their gradients, given by [51, 52]

$$\tilde{\rho}_\sigma(\mathbf{r}) = \frac{\rho(\mathbf{r})}{2}\left(1 + c_\sigma \zeta_{\mathrm{tr}}(\mathbf{r})\right), \tag{17}$$

and

$$\nabla\tilde{\rho}_\sigma(\mathbf{r}) = \frac{\nabla\rho(\mathbf{r})}{2}\left(1 + c_\sigma \zeta_{\mathrm{tr}}(\mathbf{r})\right), \tag{18}$$

respectively. Here, $c_\sigma = 1$ (-1) when $\sigma = \alpha$ (β).

It is important to note that, in deriving the translated OTPD functional expression in Eq. 16, no dependence on $\nabla\Pi(\mathbf{r})$ is assumed. A scheme in which the OTPD functional depends explicitly upon $\nabla\Pi(\mathbf{r})$ has also been proposed.[70] The corresponding "fully-translated" (ft) functionals are defined as

$$\begin{aligned} E_{\mathrm{OTPD}}\left[\rho(\mathbf{r}), \Pi(\mathbf{r}), |\nabla\rho(\mathbf{r})|, |\nabla\Pi(\mathbf{r})|\right] \equiv \\ E_{\mathrm{XC}}[\tilde{\rho}_\alpha(\mathbf{r}), \tilde{\rho}_\beta(\mathbf{r}), |\nabla\tilde{\rho}_\alpha(\mathbf{r})|, |\nabla\tilde{\rho}_\beta(\mathbf{r})|] \end{aligned} \tag{19}$$

Expressions for the fully-translated spin densities and their respective gradients, taken from Ref. 71, are provided in the Appendix.

III. COMPUTATIONAL DETAILS

The 1- and 2-RDMs entering Eqs. 9-12 are obtained from v2RDM-CASSCF computations using the v2RDM-CASSCF plugin [72] to the Psi4 electronic structure package. [73] For v2RDM-CASSCF-PDFT, we have implemented translated and fully-translated versions of the Slater and Vosko-Wilk-Nusair random-phase approximation expression III (SVWN3), [74–76] Perdew-Burke-Ernzerhof (PBE) [77] and Becke and Lee-Yang-Parr (BLYP) [78, 79] XC functionals. The XC energy, along with the one-electron and classical Coulomb contributions to the MCPDFT energy (Eq. 8) are evaluated using a new plugin to Psi4.

The results of v2RDM-CASSCF-PDFT computations of the PECs for N_2, H_2O, and CN^- are compared to those from reference computations performed using CASPT2, as implemented in the Open-MOLCAS electronic structure package. [80] The standard imaginary shift [81] of 0.20 E_h and Open-MOLCAS's default value of 0.25 E_h for ionization potential electron affinity (IPEA) [82] were applied in all CASPT2 computations. All CASPT2 computations employed a full-valence CI-driven CASSCF reference.

All v2RDM-CASSCF-PDFT computations employ the density-fitting approximation to the electron repulsion integrals.[83, 84] The N_2, H_2O, and CN^- PECs were computed using full-valence v2RDM-CASSCF, the correlation-consistent polarized-valence triple-ζ (cc-pVTZ) basis set, and the corresponding JK-type auxiliary basis set. Singlet/triplet energy gaps for the linear polyacene series were computed within the cc-pVTZ basis with the corresponding JK-type auxiliary basis set. Here, the v2RDM-CASSCF computations employ a $(4k+2, 4k+2)$ active space ($2k+1$ π bonding orbitals and $2k+1$ antibonding π^* orbitals), where k represents the number of fused six-membered rings in the polyacene molecule. Equilibrium geometries for the singlet and triplet states of the polyacene series were determined at the v2RDM-CASSCF/cc-pVDZ level of theory using a development version of the Q-Chem 5.1 electronic structure package[85] and the analytic gradient implementation described in Ref. 86.

IV. RESULTS AND DISCUSSION

A. Potential Energy Curves

Figure 1(a) provides dissociation curves for molecular nitrogen computed at the v2RDM-CASSCF, CASPT2, and v2RDM-CASSCF-PDFT levels of theory. The 2-RDMs in the v2RDM-CASSCF computations satisfied two-body (PQG) N-representability conditions. The v2RDM-CASSCF-PDFT computations employed the translated variants of the SVWN3, PBE, and BLYP functionals (denoted tSVWN3, tPBE, and tBLYP, respectively). Figure 1(b) illustrates the dissociation limit for each method, where each curve is shifted such that the energy at 3.0 Å is zero E_h. The overall shape of the CASPT2 PEC is reasonably reproduced by both the v2RDM-CASSCF and v2RDM-CASSCF-PDFT methods, but we note that the dissociation limits of CASPT2 (with an IPEA shift of 0.25 E_h) and tBLYP show an unphysical hump at 3.7 and 3.5 Å, respectively. Table I provides the non-parallelity errors (NPEs) for the PECs computed using each method, using CASPT2 as the reference. The NPEs in the v2RDM-CASSCF, tSWVN, tPBE, and tBLYP PECs are 35.5, 91.8, 17.7, and 20.9 mE_h, respectively; for comparison, the NPE for CI-based CASSCF (not illustrated in Fig. 1) is 30.1 mE_h. With the exception of v2RDM-CASSCF and tBLYP, the maximum error contributing to the NPE occurs at 5.0 Å, after CASPT2 begins to fail. Table I also provides NPEs computed when the v2RDM-CASSCF and v2RDM-CASSCF-PDFT computations were carried out using RDMs that satisfy the PQG+T2 N-representability conditions (the corresponding dissociation curves can be found in the Supporting Information). The NPE is 29.5 mE_h for v2RDM-CASSCF, which is in much better agreement with that from CI-based CASSCF. The NPEs for v2RDM-CASSCF-PDFT appear to be less sensitive to the N-representability of the RDMs; the largest change we observe is for tBLYP, where the NPE is reduced by 2.7 mE_h.

The remaining four panels in Fig. 1 illustrate the same PECs, but the v2RDM-CASSCF-PDFT computations employed the fully-translated variants of SVWN3, PBE, and BLYP functionals (denoted ftSVWN3, ftPBE, and ftBLYP, respectively). In terms of absolute energies, full translation universally lowers the energy obtained from

TABLE I: Non-parallelity errors (mE_h) in the potential energy curves with respect to that of CASPT2

Molecule	Positivity	v2RDM-CASSCF	tSVWN3	tPBE	tBLYP	ftSVWN3	ftPBE	ftBLYP
N_2		35.5	91.8	17.7	20.9	99.6	29.7	33.0
H_2O	PQG	55.5	64.0	24.5	23.7	66.4	27.2	28.6
CN^-		65.9	56.5	33.1	46.3	64.5	24.8	31.6
N_2		29.5	92.6	18.3	18.2	100.8	30.1	33.5
H_2O	PQG+T2	57.7	64.4	25.1	23.2	67.0	27.2	28.5
CN^-		68.0	63.6	31.3	43.8	71.8	23.4	29.6

FIG. 1: Potential energy curves for the dissocation of N_2 within the cc-pVTZ basis set [(a), (c)], as well as their asymptotic long-range behavior [(b), (d)]. RDMs from v2RDM-CASSCF employed within v2RDM-CASSCF-PDFT satisfy the PQG N-representability conditions. Results are provided using both the translated [(a), (b)] and fully-translated [(c), (d)] v2RDM-CASSCF-PDFT schemes.

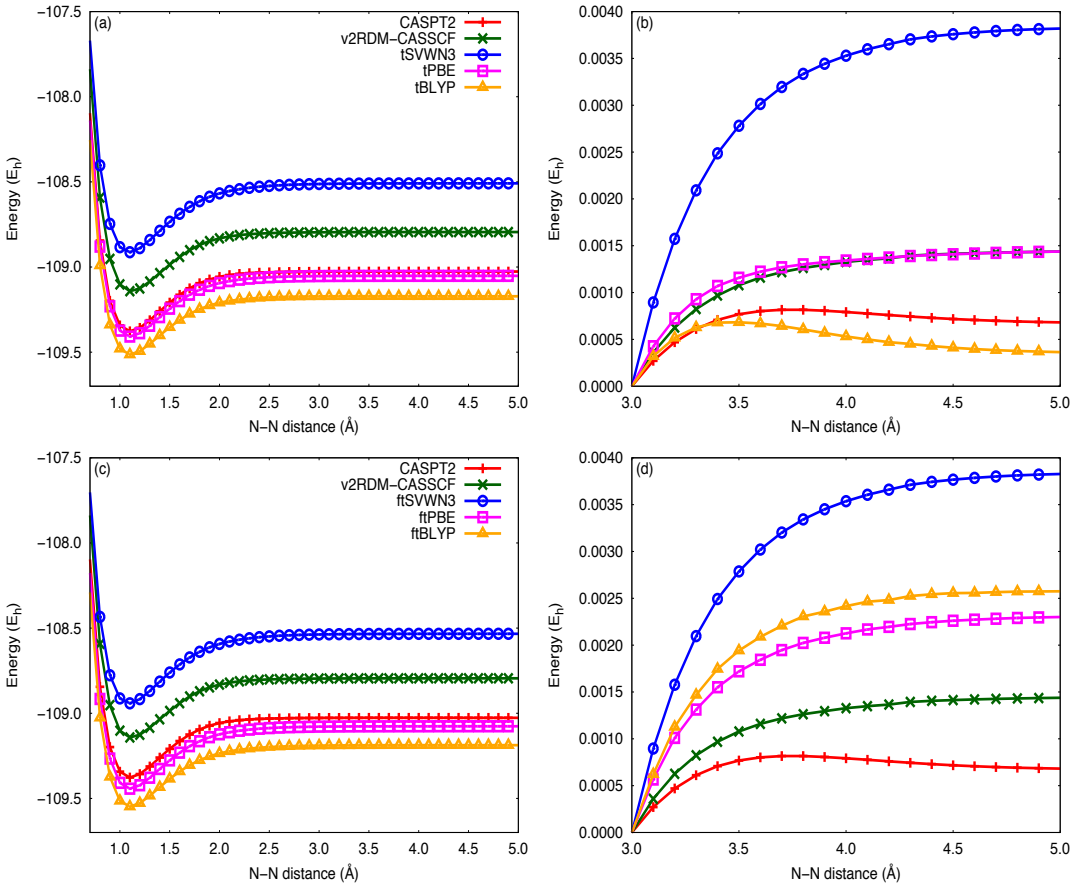

v2RDM-CASSCF-PDFT using all functionals, relative to the case in which regular translation was employed. The computed NPEs are considerably worse, increasing by as much as 12.0 and 12.1 mE_h in the cases of ftPBE and ftBLYP, respectively. Notably, full translation improves the qualitative description of the dissociation limit in the case of ftBLYP. Again, as can be seen in Table I, the NPEs for fully-translated functionals are quite insensitive to the N-representability of the reference RDMs.

Figure 2 illustrates PECs corresponding to the symmetric double dissociation of H_2O, with a fixed H–O–H angle of 104.5°, computed using the same levels of theory discussed above. Similar conclusions can be drawn in this case, regarding the qualitative agreement of the shapes of the PECs derived from v2RDM-CASSCF and v2RDM-CASSCF-PDFT, relative to that from CASPT2. However, tBLYP is the only method that displays an unphysical hump in the dissociation limit. The NPEs for v2RDM-CASSCF, tSVWN3, tPBE, and tBLYP are 55.5, 64.0, 24.5, and 23.7 mE_h, respectively, when using RDMs that satisfy the PQG conditions. As noted above, the NPE for v2RDM-CASSCF is in much better agreement with that from CI-based CASSCF (57.7 mE_h) when the RDMs satisfy the T2 condition. Again, full

translation universally lowers the energy obtained from v2RDM-CASSCF-PDFT, and the corresponding NPEs are insensitive to the N-representability of the underlying RDMs. The largest change observed in the NPE is an increase of 0.6 mE_h, in the case of ftSVWN3 and tPBE.

The last PECs considered are those for the dissociation of CN^- in the cc-pVTZ basis set, which are depicted in Fig. 3. Some of the qualitative features of the v2RDM-CASSCF and v2RDM-CASSCF-PDFT derived PECs follow the some of the same trends observed for N_2 and H_2O; for example, fully-translated functionals yield lower energies than translated ones, and tPBE and ftPBE are the most accurate flavors of v2RDM-CASSCF-PDFT, as measured by the absolute deviations from CASPT2. On the other hand, one notable difference stands out in this case: all v2RDM-based methods behave qualitatively incorrectly in the dissociation limit. It is well known that v2RDM-based approaches dissociate heteronuclear diatomic molecules into fractionally charged species;[87] the description of CN^- with v2RDM-CASSCF is one such case. This issue stems from a lack of derivative discontinuity in the energy as a function of electron number in isolated atoms, which has long been known to impact the quality of the description of the dissociation limit. [88] It is not surprising that v2RDM-CASSCF-PDFT built upon reference RDMs from v2RDM-CASSCF would display the same incorrect behavior. We also note that enforcing partial three-particle N-representability does not improve the situation; additional dissociation curves that demonstrate this failure can be found the Supporting Information.

B. Singlet-Triplet Energy Gaps: Polyacenes

The electronic structure of the linear polyacene series has long been of interest to experimentalists and theorticians alike. The optical properties of these molecules, particularly their propensity to undergo singlet fission,[89–93] make them desirable components in photovoltaic devices.[94–99] The instability of the longer members of the series usually limits practical devices to those containing four or five fused benzene rings, but synthesis of polyacenes with up to nine fused benzene rings has been reported.[100–107]

The fascinating electronic structure of the larger members of the polyacene series has fueled a series of contentious interpretations of the results of state-of-the-art electronic structure computations. These controversies began with debates over the ground spin state of the longer members of the series[108–113] and have evolved into a discussion over the degree to which the lowest-energy singlet state can be considered a closed-shell di- or polyradical.[56, 109, 111, 114–122] The former question has been settled; it is generally agreed upon that the singlet state is lower in energy than the triplet state for all linear acene molecules. Only recently, however, has it become clear that even methods capable of describing non-dynamical correlation effects in large active spaces (e.g. DMRG- or v2RDM-based CASSCF) tend to overestimate the polyradical character of the larger members of the series when correlations among the $\sigma/\sigma*$ network are ignored.[119–122] A detailed history of the progression of these controversies is recounted in Ref. 122.

In this Section, we explore the utility of v2RDM-CASSCF-PDFT for modeling the singlet/triplet energy gap in linear acene molecules. The literature is cluttered with estimates of this quantity generated using a variety of MR methods, including v2RDM-, [56, 117, 123] DMRG-, [53, 114, 116] adaptive CI (ACI)-, [118, 124] and MCPDFT-based[53, 54] approaches, as well as with multireference-averaged quadratic coupled-cluster (MR-AQCC)[125, 126] and quantum Monte-Carlo methods.[122]. Nevertheless, no one approach has emerged as a panacea for this particular problem, for a variety of reasons. First, as mentioned above, nondynamical correlation effects are quite important for large members of the series, and, yet, even active spaces comprised of the full π/π^* valence space fail to correctly describe the onset of closed-shell diradical behavior. A proper description of these systems requires that one at least consider dynamical correlation effects, if not additional nondynamical correlation effects among the remaining valence orbitals. Second, most studies employ inconsistent levels of theory to evaluate the equilibrium molecular geometries and the singlet/triplet energy gaps; equilibrium geometries are usually determined using restricted or unrestricted DFT and the B3LYP functional. Such a choice often results in singlet/triplet energy gap curves that are not completely smooth.[54, 56, 122]

Figure 4 illustrates the singlet/triplet energy gap for the linear polyacene series computed using a variety of methods, including v2RDM-CASSCF and v2RDM-CASSCF-PDFT (labeled tPBE and tBLYP). All v2RDM-based computations employed an active space comprised of the $\pi/\pi*$ valence space ($4k$+2 electrons in $4k$+2 orbitals, where k is the number of fused benzene rings in the molecule). The v2RDM-based energy gaps presented here were computed within the cc-pVTZ basis set using equilibrium geometries optimized for the singlet and triplet states at the v2RDM-CASSCF/cc-pVDZ level of theory .[86] We thus have some guarantee that the equilibrium geometries reflect the presence of nondynamical correlation effects, but we note that the structures display signatures of the overestimation of polyradical character discussed above (see Refs. 122 and 86 for a discussion of these effects). Nonetheless, the v2RDM-CASSCF energy gaps agree well with those from DMRG[114], despite the fact that the DMRG data were generated using a smaller basis set and B3LYP-derived geometries. As expected, the dynamical correlation effects captured by v2RDM-CASSCF-PDFT close the singlet/triplet energy gap considerably for larger molecules, and we note that the tPBE and tBLYP functionals yield essentially equivalent gaps for all molecules. Surpris-

FIG. 2: Potential energy curves for the symmetric dissocation of H_2O within the cc-pVTZ basis set [(a), (c)], as well as their asymptotic long-range behavior [(b), (d)]. RDMs from v2RDM-CASSCF employed within v2RDM-CASSCF-PDFT satisfy the PQG N-representability conditions. Results are provided using both the translated [(a), (b)] and fully-translated [(c), (d)] v2RDM-CASSCF-PDFT schemes.

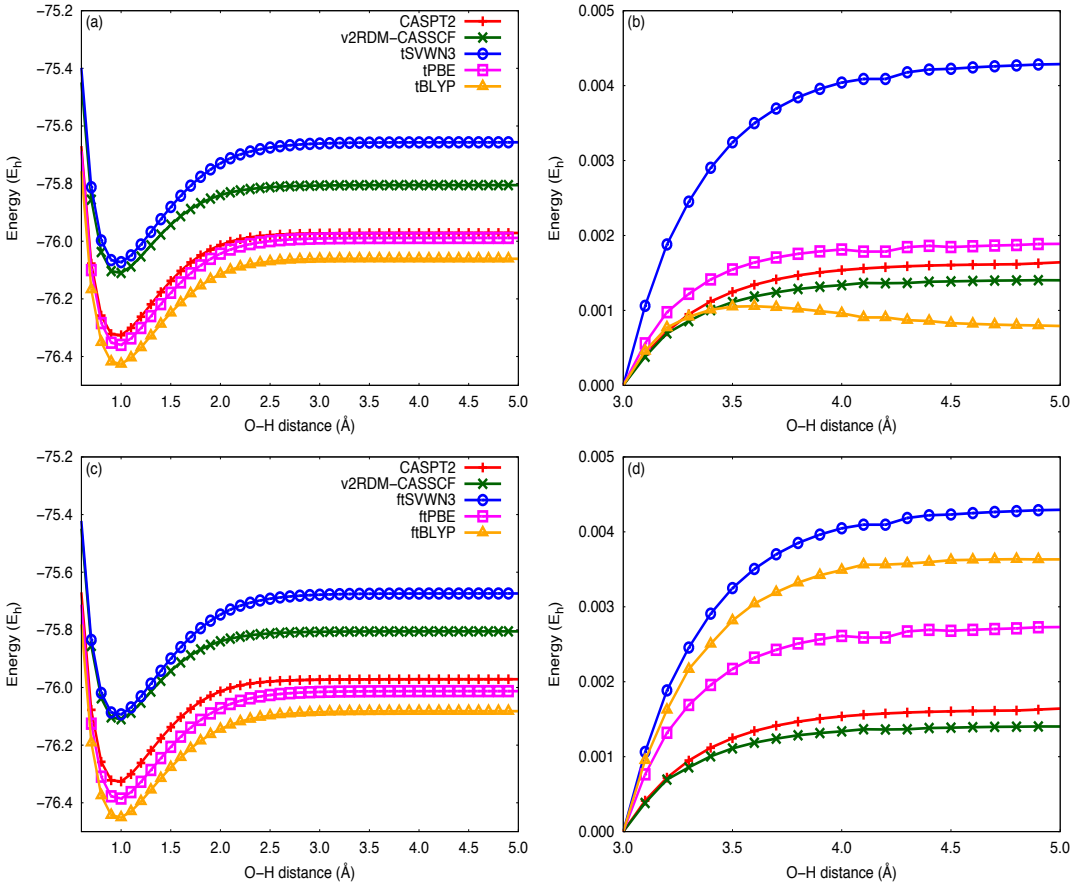

ingly, DMRG-PDFT and v2RDM-CASSCF-PDFT give quite different results for hexacene and heptacene. The DMRG-PDFT data of Ref. 53 were generated within the 6-31+G(d,p) basis set, using B3LYP-derived geometries, but, these differences are still unanticipated, considering the good agreement we observe between the DMRG results of Ref. 114 and the present v2RDM-CASSCF results.

Figure 4 also includes data generated using a combined ACI / second-order perturbative multireference driven similarity renormalization group (DSRG-MRPT2) approach and the particle-particle random phase approximation (pp-RPA), taken from Refs. 124 and 127, respectively. Of all methods considered here, ACI-DSRG-MRPT2 yields the best agreement with experimental results, up to heptacene. Assuming that ACI and DSRG-MRPT2 can be extended to larger members of this series, ACI-DSRG-MRPT2 appears to be an extremely promising approach for this problem. Comparisons against pp-RPA results are complicated, however, by the fact that these gaps are vertical, whereas the present results and all others reproduced here are adiabatic. The label pp-RPA-R (pp-RPA-T) refers to computations performed at equilibrium geometries generated for the singlet (triplet) at the restricted (unrestricted) B3LYP level of theory. The pp-RPA data were also generated in a smaller basis set (cc-pVDZ) than was employed in the present v2RDM-CASSCF-PDFT computations. The pp-RPA-T predicts singlet/triplet energy gaps that are significantly lower than those predicted by all other methods. Further, pp-RPA-T is the only method that yields gaps that do not decrease monotonically with increasing polyacene length. We note that the gaps from pp-RPA-R, however, are in good agreement with the present tPBE/tBLYP gaps, for acene molecules smaller than nonacene.

Lastly, we consider the singlet/triplet energy gap extrapolated to the limit of an infinitely large molecule. The computed singlet/triplet energy gaps ($\Delta E_{\text{S-T}}$) for finite molecules were fit to an exponential decay formula of the form

$$\Delta E_{\text{S-T}}(k) = ae^{-k/b} + c \tag{20}$$

where, a, b and c are adjustable parameters, and k represents the number of fused benzene rings in the molecule. In the limit that k approaches infinity, $c \sim \Delta E_{\text{S-T}}(\infty)$.

FIG. 3: Potential energy curves for the dissocation of CN^- within the cc-pVTZ basis set [(a), (c)], as well as their asymptotic long-range behavior [(b), (d)]. RDMs from v2RDM-CASSCF employed within v2RDM-CASSCF-PDFT satisfy the PQG N-representability conditions. Results are provided using both the translated [(a), (b)] and fully-translated [(c), (d)] v2RDM-CASSCF-PDFT schemes.

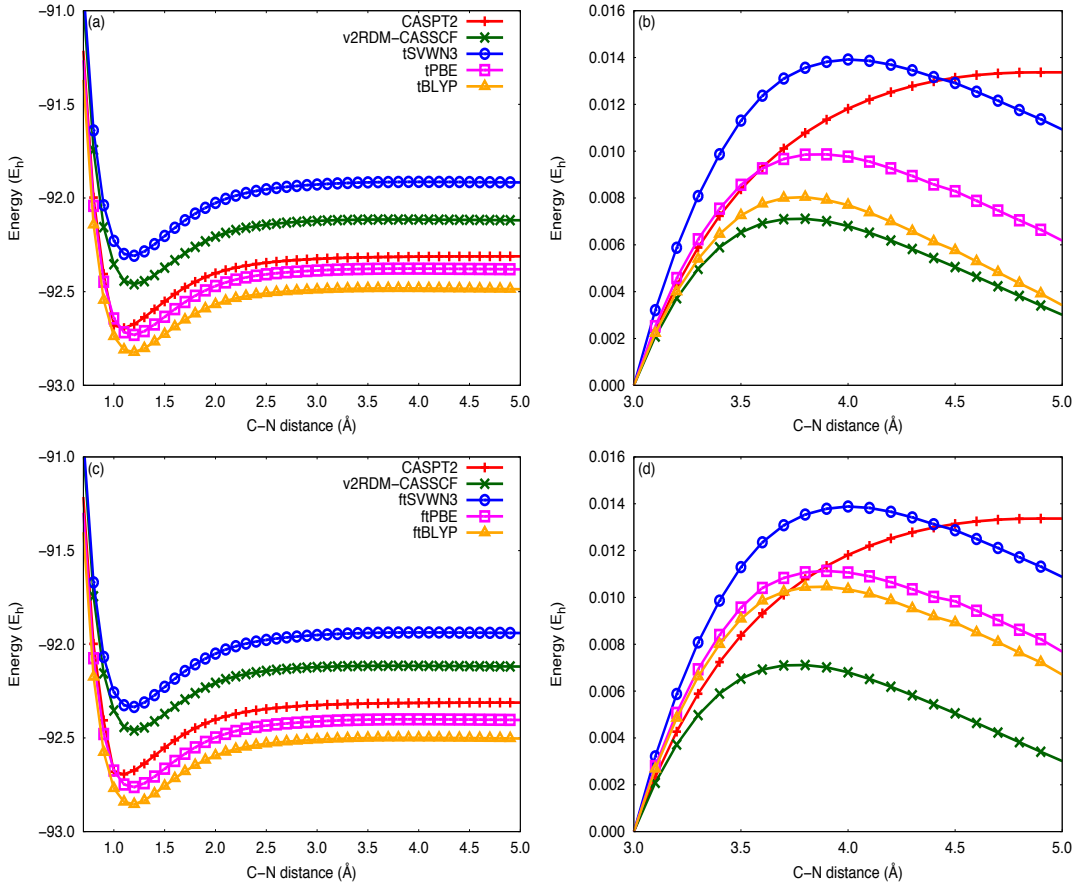

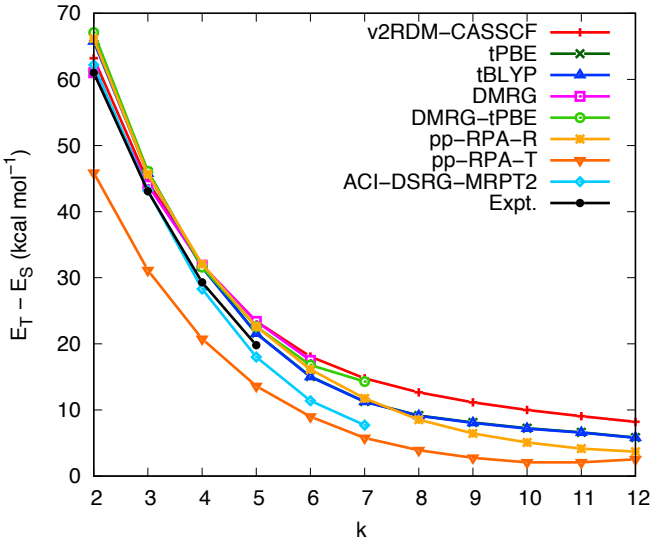

FIG. 4: Singlet-triplet energy gaps of the linear polyacene series. The label "k" refers to the number of fused benzene rings in each molecule.

Table II summarizes the fitting parameters and predictions for $\Delta E_{\text{S-T}}(\infty)$ for a subset of methods considered above for which data are available up to $k = 12$. The largest predicted gap is obtained by v2RDM-CASSCF, which indicates that the limited considerations of nondynamical correlation, combined with a lack of dynamical correlation, artificially stabilize the singlet state. The gaps predicted by tPBE and tBLYP are 4.87 and 4.79 kcal mol^{-1}, respectively. These values are in good agreement with the "best estimate" value of 5.06 kcal mol^{-1} of Ref. 113, which was computed using a combination of spin-flip coupled-cluster and spin-flip time-dependent DFT. The smallest estimates for the infinite-acene singlet/triplet gap are given by pp-RPA-R and pp-RPA-T.

V. CONCLUSIONS

Multiconfigurational pair-density functional theory provides a conceptually and technically straightfoward framework within which one can combine the reliable description of nondynamical correlation effects afforded by multireference methods with the simplicity of DFT for

TABLE II: Fitting formulas for singlet-triplet energy gaps of polyacenes as a function of number of fused benzene rings k where $k \in [2, 12]$

Level of Theory	Fitting Formula
v2RDM-CASSCF/cc-pVTZ[a]	$127.79\exp(-k/2.39) + 7.85$
tPBE/cc-pVTZ[a]	$147.15\exp(-k/2.32) + 4.87$
tBLYP/cc-pVTZ[a]	$145.04\exp(-k/2.33) + 4.79$
pp-RPA-R/cc-pVDZ[b]	$137.04\exp(-k/2.63) + 2.11$
pp-RPA-T/cc-pVDZ[b]	$105.87\exp(-k/2.37) + 0.81$

[a] Geometries are optimized at v2RDM-CASSCF/cc-pVDZ level of theory.
[b] Geometries are optimized at B3LYP/6–31G(d) level of theory.

modeling dynamical correlation. In practice, the computational cost of MCPDFT is dominated entirely by the effort required to generate the 1- and 2-RDM using the underlying MR approach. Hence, polynomially-scaling approaches to the nondynamical correlation problem (e.g. v2RDM-CASSCF, DMRG-CASSCF[53], or pair coupled-cluster doubles[32]) are naturally suited to this purpose. Accordingly, we have presented an implementation of v2RDM-CASSCF-PDFT and benchmarked its performance on challenging MR problems.

We applied v2RDM-CASSCF-PDFT with the translated and fully-translated variants of the PBE, BLYP, and SVWN3 functionals to the dissociation of N_2 and CN^- and to the double dissociation of H_2O. In general, the best agreement with potential energy curves generated at the CASPT2 level of theory was obtained using tPBE. Surprisingly, the quality of the v2RDM-CASSCF-PDFT curves, as measured by the non-parallelity error relative to CASPT2, was somewhat insensitive to the N-representability of the underlying 2-RDM.

We also applied the tPBE and tBLYP functionals to the singlet/triplet energy gap of the linear polyacene series; these functionals predict the gap in the limit of an infinitely long acene molecule to be 4.87 and 4.79 kcal mol^{-1}, respectively. We note that a similar study has been carried out using MCPDFT where the 1- and 2-RDM were generated using the generalized active space self-consistent field (GASSCF) method.[54] However, direct comparisons to the data presented in Ref. 54 are difficult because the GASSCF and GASSCF-PDFT results are sensitive to the partitioning chosen for the active space. For example, one choice leads to the prediction that the GASSCF-PDFT-derived singlet/triplet gap in the large molecule limit closes, relative to that from GASSCF, while another choice leads to the prediction that it opens. Further, regardless of how the active space was partitioned in that work, GASSCF-PDFT failed to yield a smooth singlet/triplet energy gap curve.

VI. APPENDIX

The fully-translated densities and gradients entering the fully-translated OTPD functional (defined in Eq. 19) are given by [71]

$$\tilde{\rho}_\sigma(\mathbf{r}) = \begin{cases} \frac{\rho(\mathbf{r})}{2}\left(1 + c_\sigma \zeta_{\mathrm{tr}}(\mathbf{r})\right) & R(\mathbf{r}) < R_0 \\ \frac{\rho(\mathbf{r})}{2}\left(1 + c_\sigma \zeta_{\mathrm{ftr}}(\mathbf{r})\right) & R_0 \le R(\mathbf{r}) \le R_1 \\ \frac{\rho(\mathbf{r})}{2} & R(\mathbf{r}) > R_1 \end{cases} \qquad \nabla\tilde{\rho}_\sigma(\mathbf{r}) = \begin{cases} \frac{\nabla\rho(\mathbf{r})}{2}\left(1 + c_\sigma \zeta_{\mathrm{tr}}(\mathbf{r})\right) + c_\sigma \frac{\rho(\mathbf{r})}{2}\nabla\zeta_{\mathrm{tr}}(\mathbf{r}) & R(\mathbf{r}) < R_0 \\ \frac{\nabla\rho(\mathbf{r})}{2}\left(1 + c_\sigma \zeta_{\mathrm{ftr}}(\mathbf{r})\right) + c_\sigma \frac{\rho(\mathbf{r})}{2}\nabla\zeta_{\mathrm{ftr}}(\mathbf{r}) & R_0 \le R(\mathbf{r}) \le R_1 \\ \frac{\nabla\rho(\mathbf{r})}{2} & R(\mathbf{r}) > R_1 \end{cases} \tag{21}$$

where $R_0 = 0.9$ and $R_1 = 1.15$. [70, 71] The fully-translated spin-polarization factor $\zeta_{\mathrm{ftr}}(\mathbf{r})$ is taken to be

$$\zeta_{\mathrm{ftr}} = A\Delta R^5(\mathbf{r}) + B\Delta R^4(\mathbf{r}) + C\Delta R^3(\mathbf{r}) \tag{22}$$

where, $\Delta R(\mathbf{r}) = R(\mathbf{r}) - R_1$ and [70, 71]

$$A = -475.60656009 \tag{23}$$
$$B = -379.47331922 \tag{24}$$
$$C = -85.38149682 \tag{25}$$

The gradients of the translated and fully-translated spin-polarization factors are [70, 71]

$$\nabla\zeta_{\mathrm{tr}}(\mathbf{r}) = -\frac{1}{2}\frac{\nabla R(\mathbf{r})}{\zeta_{\mathrm{tr}}(\mathbf{r})} \tag{26}$$

$$\nabla\zeta_{\mathrm{ftr}}(\mathbf{r}) = \nabla R(\mathbf{r})\ \left[5A\Delta R^4(\mathbf{r}) + 4B\Delta R^3(\mathbf{r}) + 3C\Delta R^2(\mathbf{r})\right] \tag{27}$$

where the gradient of the on-top ratio is [70]

$$\nabla R(\mathbf{r}) = \frac{4\nabla\Pi(\mathbf{r})}{\rho^2(\mathbf{r})} - \frac{8\Pi(\mathbf{r})\nabla\rho(\mathbf{r})}{\rho^3(\mathbf{r})}. \tag{28}$$

Supporting information. Potential energy curves for N_2, CN^- and H_2O dissociation computed using v2RDM-CASSCF / v2RDM-CASSCF-PDFT and the PQG+T2 N-representability conditions, as well as singlet/triplet energy gaps for linear polyacene molecules computed using v2RDM-CASSCF / v2RDM-CASSCF-PDFT and RDMs that satisfy the PQG N-representability conditions.

Acknowledgments This material is based upon work supported by the Army Research Office Small Business

Technology Transfer (STTR) program under Grant No. W911NF-16-C-0124.

[1] W. Kutzelnigg, *Theory of Electron Correlation in: Explicitly correlated wave functions in Chemistry and Physics* (Springer Netherlands, 2003), pp. 3–90, Progress in Theoretical Chemistry and Physics.

[2] W. Kutzelnigg, *Electron correlation and electron pair theories* (Springer, Berlin, Heidelberg, 1973), pp. 31–73.

[3] C. Hättig, W. Klopper, A. Köhn, and D. P. Tew, Chem. Rev. **112**, 4 (2012).

[4] B. O. Roos, R. Lindh, P. A. Malmqvist, V. Veryazov, and P.-O. Widmark, *Multiconfigurational quantum chemistry* (Wiley, 2016).

[5] T. Helgaker, P. Jørgensen, and J. Olsen, *Molecular electronic-structure theory* (Wiley, 2000).

[6] A. Szabo and N. S. Ostlund, *Modern quantum chemistry : introduction to advanced electronic structure theory* (Dover Publications, 1996).

[7] D. R. Yarkony, *Modern Electronic Structure Theory*, vol. 2 of *Advanced Series in Physical Chemistry* (World Scientific Publishing Company, 1995).

[8] R. G. Parr and W. Yang, *Density-functional theory of atoms and molecules* (Oxford University Press, 1989).

[9] C. Fiolhais, F. Nogueira, and M. A. L. Marques, eds., *A Primer in Density Functional Theory*, vol. 620 of *Lecture Notes in Physics* (Springer Berlin Heidelberg, Berlin, Heidelberg, 2003).

[10] A. J. Garza, G. E. Scuseria, A. Ruzsinszky, J. Sun, and J. P. Perdew, Mol. Phys. **114**, 928 (2016).

[11] A. J. Cohen, P. Mori-Sánchez, and W. Yang, Chem. Rev. **112**, 289 (2012).

[12] A. D. Becke, J. Chem. Phys. **140** (2014).

[13] J. Cioslowski, ed., *Many-Electron Densities and Reduced Density Matrices*, Mathematical and Computational Chemistry (Springer US, Boston, MA, 2000).

[14] E. R. Davidson, *Reduced density matrices in quantum chemistry* (Academic Press, 1976).

[15] A. J. Coleman and V. I. Yukalov, *Reduced density matrices : Coulson's challenge* (Springer, 2000).

[16] D. A. Mazziotti, *Reduced-density-matrix mechanics : with applications to many-electron atoms and molecules* (Wiley, 2007).

[17] N. I. Gidopoulos and S. Wilson, *The Fundamentals of Electron Density, Density Matrix and Density Functional Theory in Atoms, Molecules and the Solid State* (Springer Netherlands, 2003).

[18] T. Helgaker, S. Coriani, P. Jørgensen, K. Kristensen, J. Olsen, and K. Ruud, Chem. Rev. **112**, 543 (2012).

[19] P. G. Szalay, T. Müller, G. Gidofalvi, H. Lischka, and R. Shepard, Chem. Rev. **112**, 108 (2012).

[20] B. O. Roos, P. R. Taylor, and P. E. M. Siegbahn, Chem. Phys. **48**, 157 (1980).

[21] P. Siegbahn, A. Heiberg, B. Roos, and B. Levy, Phys. Scripta **21**, 323 (1980).

[22] P. E. M. Siegbahn, J. Almlöf, A. Heiberg, and B. O. Roos, J. Chem. Phys. **74**, 2384 (1981).

[23] B. O. Roos, *The Complete Active Space Self-Consistent Field Method and its Applications in Electronic Structure Calculations* (John Wiley & Sons, Inc., 1987), vol. 68, pp. 399–445.

[24] K. Andersson, P. A. Malmqvist, B. O. Roos, A. J. Sadlej, and K. Wolinski, J. Phys. Chem. **94**, 5483 (1990).

[25] K. Andersson, P. Å. Malmqvist, and B. O. Roos, J. Chem. Phys. **96**, 1218 (1992).

[26] D. Mukherjee and W. Kutzelnigg, J. Chem. Phys. **114**, 2047 (2001).

[27] W. Kutzelnigg and D. Mukherjee, J. Chem. Phys. **120**, 7350 (2004).

[28] D. A. Mazziotti, Phys. Rev. Lett. **97**, 143002 (2006).

[29] F. A. Evangelista, J. Chem. Phys. **141** (2014).

[30] G. C. Lie and E. Clementi, J. Chem. Phys. **60**, 1275 (1974).

[31] G. C. Lie and E. Clement, J. Chem. Phys. **60**, 1288 (1974).

[32] A. J. Garza, I. W. Bulik, T. M. Henderson, and G. E. Scuseria, J. Chem. Phys. **142** (2015).

[33] A. J. Pérez-Jiménez and J. M. Pérez-Jordá, Phys. Rev. A **75**, 012503 (2007).

[34] R. Colle and O. Salvetti, Theor. Chim. Acta **53**, 55 (1979).

[35] F. Moscardó and E. San-Fabián, Phys. Rev. A **44**, 1549 (1991).

[36] A. J. Garza, C. A. Jiménez-Hoyos, and G. E. Scuseria, J. Chem. Phys. **138**, 134102 (2013).

[37] S. Paziani, S. Moroni, P. Gori-Giorgi, and G. B. Bachelet, Phys. Rev. B **73**, 155111 (2006).

[38] S. Gusarov, P. Malmqvist, R. Lindh, and B. O. Roos, Theor. Chim. Acta **112**, 84 (2004).

[39] S. Gusarov, P.-Å. Malmqvist, and R. Lindh, Mol. Phys. **102**, 2207 (2004).

[40] R. Takeda, S. Yamanaka, and K. Yamaguchi, Chem. Phys. Lett. **366**, 321 (2002).

[41] H. Stoll, Chem. Phys. Lett. **376**, 141 (2003).

[42] J. Gräfenstein and D. Cremer, Chem. Phys. Lett. **316**, 569 (2000).

[43] J. Gräfenstein and D. Cremer, Mol. Phys. **103**, 279 (2005).

[44] B. Miehlich, H. Soll, and A. Savin, Mol. Phys. **91**, 527 (1997).

[45] S. Grimme and M. Waletzke, J. Chem. Phys. **111**, 5645 (1999).

[46] W. Wu and S. Shaik, Chem. Phys. Lett. **301**, 37 (1999).

[47] R. Pollet, A. Savin, T. Leininger, and H. Stoll, J. Chem. Phys. **116**, 1250 (2002).

[48] T. Leininger, H. Stoll, H.-J. Werner, and A. Savin, Chem. Phys. Lett. **275**, 151 (1997).

[49] N. O. Malcolm and J. J. McDouall, J. Phys. Chem. **100**, 10131 (1996).

[50] E. Kraka, Chem. Phys. **161**, 149 (1992).

[51] L. Gagliardi, D. G. Truhlar, G. L. Manni, R. K. Carlson, C. E. Hoyer, and J. L. Bao, Acc. Chem. Res. **50**, 66 (2017).

[52] G. Li Manni, R. K. Carlson, S. Luo, D. Ma, J. Olsen, D. G. Truhlar, and L. Gagliardi, J. Chem. Theory Com-

put. **10**, 3669 (2014).
[53] P. Sharma, V. Bernales, S. Knecht, D. G. Truhlar, and L. Gagliardi, p. arXivID: 1808.06273 (2018).
[54] S. Ghosh, C. J. Cramer, D. G. Truhlar, and L. Gagliardi, Chem. Sci. **8**, 2741 (2017).
[55] G. Gidofalvi and D. A. Mazziotti, J. Chem. Phys. **129**, 134108 (2008).
[56] J. Fosso-Tande, T.-S. Nguyen, G. Gidofalvi, and A. E. DePrince III, J. Chem. Theory Comput. **12**, 2260 (2016).
[57] T. Helgaker, P. Jørgensen, and J. Olsen, *Molecular Electronic-Structure Theory* (John Wiley & Sons, Inc., New York, 2000).
[58] K. Husimi, Proceedings of the Physico-Mathematical Society of Japan. 3rd Series **22**, 264 (1940).
[59] J. E. Mayer, Phys. Rev. **100**, 1579 (1955).
[60] P.-O. Löwdin, Phys. Rev. **97**, 1474 (1955).
[61] E. Pérez-Romero, L. M. Tel, and C. Valdemoro, Int. J. Quantum Chem. **61**, 55 (1997).
[62] C. Garrod and J. K. Percus, J. Math. Phys. **5**, 1756 (1964).
[63] Z. Zhao, B. J. Braams, M. Fukuda, M. L. Overton, and J. K. Percus, J. Chem. Phys. **120**, 2095 (2004).
[64] R. M. Erdahl, Int. J. Quantum Chem. **13**, 697 (1978).
[65] J. Povh, F. Rendl, and A. Wiegele, Computing **78**, 277 (2006).
[66] J. Malick, J. Povh, F. Rendl, and A. Wiegele, SIAM J. Optim. **20**, 336 (2009).
[67] D. A. Mazziotti, Phys. Rev. Lett. **106**, 83001 (2011).
[68] J. P. Perdew, A. Savin, and K. Burke, Phys. Rev. A **51**, 4531 (1995).
[69] A. D. Becke, A. Savin, and H. Stoll, Theor. Chim. Acta **91**, 147 (1995).
[70] A. M. Sand, C. E. Hoyer, K. Sharkas, K. M. Kidder, R. Lindh, D. G. Truhlar, and L. Gagliardi, J. Chem. Theory Comput. **14**, 126 (2018).
[71] R. K. Carlson, D. G. Truhlar, and L. Gagliardi, J. Chem. Theory Comput. **11**, 4077 (2015).
[72] See https://github.com/edeprince3/v2rdm_casscf for v2RDM-CASSCF v0.8, a variational two-electron reduced-density-matrix-driven approach to complete active space self-consistent field theory (2018).
[73] J. M. Turney, A. C. Simmonett, R. M. Parrish, E. G. Hohenstein, F. A. Evangelista, J. T. Fermann, B. J. Mintz, L. A. Burns, J. J. Wilke, M. L. Abrams, et al., WIRES Comput. Mol. Sci. **2**, 556 (2012).
[74] R. Gáspár, Acta Physica Academiae Scientiarum Hungaricae **35**, 213 (1974).
[75] J. C. Slater, Phys. Rev. **81**, 385 (1951).
[76] S. H. Vosko, L. Wilk, and M. Nusair, Can. J. Phys. **58**, 1200 (1980).
[77] J. P. Perdew, K. Burke, and M. Ernzerhof, Phys. Rev. Lett. **77**, 3865 (1996).
[78] A. D. Becke, Phys. Rev. A **38**, 3098 (1988).
[79] C. Lee, W. Yang, and R. G. Parr, Phys. Rev. B **37**, 785 (1988).
[80] F. Aquilante, J. Autschbach, R. K. Carlson, L. F. Chibotaru, M. G. Delcey, L. De Vico, I. Fdez. Galván, N. Ferré, L. M. Frutos, L. Gagliardi, et al., J. Comput. Chem. **37**, 506 (2016).
[81] N. Forsberg and P.-Å. Malmqvist, Chem. Phys. Lett. **274**, 196 (1997).
[82] G. Ghigo, B. O. Roos, and P. Å. Malmqvist, Chem. Phys. Lett. **396**, 142 (2004).
[83] J. L. Whitten, J. Chem. Phys. **58**, 4496 (1973), arXiv:1011.1669v3.
[84] B. I. Dunlap, J. W. D. Connolly, and J. R. Sabin, J. Chem. Phys. **71**, 3396 (1979).
[85] Y. Shao, Z. Gan, E. Epifanovsky, A. T. Gilbert, M. Wormit, J. Kussmann, A. W. Lange, A. Behn, J. Deng, X. Feng, et al., **113**, 184 (2015), URL `https://doi.org/10.1080/00268976.2014.952696`.
[86] J. W. Mullinax, E. Epifanovsky, G. Gidofalvi, and A. E. DePrince III, submitted (2018), URL `https://arxiv.org/abs/1809.09058`.
[87] H. Van Aggelen, P. Bultinck, B. Verstichel, D. Van Neck, and P. W. Ayers, Phys. Chem. Chem. Phys. **11**, 5558 (2009).
[88] J. P. Perdew, R. G. Parr, M. Levy, and J. L. Balduz, Phys. Rev. Lett. **49**, 1691 (1982).
[89] M. J. Tayebjee, D. R. McCamey, and T. W. Schmidt, J. Phys. Chem. Lett. **6**, 2367 (2015).
[90] M. C. Hanna and A. J. Nozik, Journal of Applied Physics **100**, 074510 (2006).
[91] P. M. Zimmerman, F. Bell, D. Casanova, and M. Head-Gordon, J. Am. Chem. Soc. **133**, 19944 (2011).
[92] M. W. B. Wilson, A. Rao, B. Ehrler, and R. H. Friend, Acc. Chem. Res. **46**, 1330 (2013).
[93] S. Izadnia, D. W. Schönleber, A. Eisfeld, A. Ruf, A. C. LaForge, and F. Stienkemeier, J. Phys. Chem. Lett. **8**, 2068 (2017).
[94] S. Yoo, B. Domercq, and B. Kippelen, Appl. Phys. Lett. **85**, 5427 (2004).
[95] A. C. Mayer, M. T. Lloyd, D. J. Herman, T. G. Kasen, and G. G. Malliaras, Appl. Phys. Lett. **85**, 6272 (2004).
[96] C.-W. Chu, Y. Shao, V. Shrotriya, and Y. Yang, Appl. Phys. Lett. **86**, 243506 (2005).
[97] I. Paci, J. C. Johnson, X. Chen, G. Rana, D. Popović, D. E. David, A. J. Nozik, M. A. Ratner, and J. Michl, J. Am. Chem. Soc. **128**, 16546 (2006).
[98] B. P. Rand, J. Genoe, P. Heremans, and J. Poortmans, Prog. Photovolt. Res. Appl. **15**, 659 (2007).
[99] Y. Shao, S. Sista, C.-W. Chu, D. Sievers, and Y. Yang, Appl. Phys. Lett. **90**, 103501 (2007).
[100] J. B. Birks, *Photophysics of aromatic molecules* (Wily-Interscience, London, 1970).
[101] J. Schiedt and R. Weinkauf, Chem. Phys. Lett. **266**, 201 (1997).
[102] H. Angliker, E. Rommel, and J. Wirz, Chem. Phys. Lett. **87**, 208 (1982).
[103] N. Sabbatini, M. T. Indelli, M. T. Gandolfi, and V. Balzani, J. Phys. Chem. **86**, 3585 (1982).
[104] J. Burgos, M. Pope, C. E. Swenberg, and R. R. Alfano, Phys. Status Solidi B **83**, 249 (1977).
[105] R. Mondal, C. Tönshoff, D. Khon, D. C. Neckers, and H. F. Bettinger, J. Am. Chem. Soc. **131**, 14281 (2009).
[106] C. Tönshoff and H. Bettinger, Angew. Chem. Int. Ed. **49**, 4125 (2010).
[107] S. Zade and M. Bendikov, Angew. Chem. Int. Ed. **49**, 4012 (2010).
[108] K. N. Houk, P. S. Lee, and M. Nendel, J. Org. Chem. **66**, 5517 (2001).
[109] M. Bendikov, H. M. Duong, K. Starkey, K. N. Houk, E. A. Carter, and F. Wudl, J. Am. Chem. Soc. **126**, 7416 (2004).
[110] D.-e. Jiang and S. Dai, J. Phys. Chem. A **112**, 332 (2008).
[111] B. Hajgató, D. Szieberth, P. Geerlings, F. De Proft,

and M. S. Deleuze, J. Chem. Phys. **131**, 224321 (2009), ISSN 00219606.
[112] C.-S. Wu and J.-D. Chai, J. Chem. Theory Comput. **11**, 2003–2011 (2015).
[113] C. U. Ibeji and D. Ghosh, Phys. Chem. Chem. Phys. **17**, 9849 (2015).
[114] J. Hachmann, J. J. Dorando, M. Avilés, and G. K.-L. Chan, J. Chem. Phys. **127**, 134309 (2007).
[115] G. Gidofalvi and D. A. Mazziotti, J. Chem. Phys. **129**, 134108 (2008).
[116] W. Mizukami, Y. Kurashige, and T. Yanai, J. Chem. Theory Comput. **9**, 401 (2013).
[117] J. Fosso-Tande, D. R. Nascimento, and A. E. DePrince III, Mol. Phys. **114**, 423 (2016).
[118] J. B. Schriber and F. A. Evangelista, J. Chem. Phys. **144**, 161106 (2016).
[119] J. Lee, D. W. Small, E. Epifanovsky, and M. Head-Gordon, J. Chem. Theory Comput. **13**, 602 (2017).
[120] S. Battaglia, N. Faginas-Lago, D. Andrae, S. Evangelisti, and T. Leininger, J. Phys. Chem. A **121**, 3746 (2017).
[121] S. Lehtola, J. Parkhill, and M. Head-Gordon, Mol. Phys. **116**, 547 (2018).
[122] N. Dupuy and M. Casula, J. Chem. Phys. **148**, 134112 (2018).
[123] K. Pelzer, L. Greenman, G. Gidofalvi, and D. A. Mazziotti, J. Phys. Chem. A **115**, 5632 (2011).
[124] J. B. Schriber, K. P. Hannon, and F. A. Evangelista, p. arXivID: 1808.09403 (2018).
[125] F. Plasser, H. Pašalić, M. H. Gerzabek, F. Libisch, R. Reiter, J. Burgdörfer, T. Müller, R. Shepard, and H. Lischka, Angew. Chem. Int. Ed. **52**, 2581 (2013).
[126] S. Horn, F. Plasser, T. Müller, F. Libisch, J. Burgdörfer, and H. Lischka, Theor. Chem. Acc. **133**, 1511 (2014).
[127] Y. Yang, E. R. Davidson, and W. Yang, Proc. Nat. Acad. Sci. **113**, E5098 (2016).